

Análise do Espectro de Potências de Galáxias: Uma abordagem via métodos de Monte-Carlo

Arthur Eduardo da Mota Loureiro

Orientador: Prof. Dr. Luís Raul Weber Abramo

Dissertação apresentada ao Instituto de Física da Universidade de São Paulo para a obtenção do título de Mestre em Ciências.

Banca Examinadora:

Prof. Dr. Luís Raul Weber Abramo (IF-USP)

Prof. Dr. Marcos Vinicius Borges Teixeira Lima (IF-USP)

Prof. Dr. Eduardo Serra Cypriano (IAG-USP)

São Paulo
2015

FICHA CATALOGRÁFICA
Preparada pelo Serviço de Biblioteca e Informação
do Instituto de Física da Universidade de São Paulo

Loureiro, Arthur Eduardo da Mota

Análise do espectro de potências de galáxias: um abordagem via métodos de Monte-Carlo. São Paulo, 2015.

Dissertação (Mestrado) – Universidade de São Paulo.
Instituto de Física. Depto. Física Matemática

Orientador: Prof. Dr. Luís Raul Weber Abramo

Área de Concentração: Física

Unitermos: 1. Cosmologia; 2. Estrutura do universo;
3. Método de Monte Carlo.

USP/IF/SBI-056/2015

UNIVERSIDADE DE SÃO PAULO
INSTITUTO DE FÍSICA

Galaxy Power Spectrum Analysis: A Monte-Carlo Approach

Arthur Eduardo da Mota Loureiro

Advisor: Prof. Dr. Luís Raul Weber Abramo

Dissertation presented to the Institute of Physics, University of Sao Paulo, in partial fulfilment of the requirements for the degree of Master of Sciences

Examination Committee:

Prof. Dr. Luís Raul Weber Abramo (IF-USP)

Prof. Dr. Marcos Vinicius Borges Teixeira Lima (IF-USP)

Prof. Dr. Eduardo Serra Cypriano (IAG-USP)

São Paulo
2015

“It might be possible that the world
itself is without meaning.”

Virginia Woolf, *Mrs. Dalloway*

Acknowledgments

Firstly, I would like to thank my advisor, Prof. Raul Abramo, for all the guidance, help, time, and – more importantly – patience to advise me throughout the realization of this work. Secondly, my colleague Lucas Secco, for all the collaboration, companionship, and specially for writing the first version of the FKP code adapted to be used on the Monte-Carlo analysis. Likewise, I would like to thank Prof. Marcos Lima, whose classes were fundamentally important to my academic formation as a cosmologist, and to specially thank Prof. Silvio R. Dahmen from *Universidade Federal do Rio Grande do Sul* for the academic and personal guidance, moral support, encouragement, and friendship through all these years of my academic life.

I would also like to thank all the people at *Departamento de Física Matemática* and *Departamento de Astronomia* for all the amazing discussions on the seminars, “CosmoClubs”, and classes, specially Meera Machado for all the excellent discussions about science, all the support, and for a friendship that transcends the work environment. Also, André Vitorelli, Michel Agüena, Hugo Camacho, André Alencar, Carolina Queiroz, Rodrigo Voivodic, Pramod Padmanabhan, Pablo Ibieta, Irene Balmes, and Loic Le Tiran, without whom this epoch would be much less enjoyable.

I would like thank my mother, Maria Alice Mota, my father, Eduardo Loureiro, and my grandparents, Irene and Porfírio Mota, for the constant comprehension, moral support, and for always believing in me; my friends in São Paulo, Cláudio Pérsio, Pedro Axelrud, Virginia Stefanello, Moreno Hassem, Dr. Alexandre Hassem Neto, and Cláudia Carpes, for living here was made more enjoyable because of them; and all my friends in Porto Alegre for their constant encouragement, specially Vivian Pizzato, Nicole de March, Sophie Collignon, André Gomes, Marcelo Pereira, Rodrigo Sieben, Marcelo Fontoura, Gabriel Carpes, Camilla Carpes, Eleonor Carpes, Guilherme Kolinger, Débora Peretti, Ingrid Pelisoli, Isadora Alves, Felipe Antunes, Augusto Medeiros, and many more. Finally, a special thanks to Karina Pacheco for constantly pushing me towards being a better and wiser person.

This work was performed using the computing facilities of the Laboratory of Astroinformatics (IAG/USP, NAT/Unicsul), funded by the Brazilian agency FAPESP (grant 2009/54006-4) and the INCT-A. During this work, I have been supported by the Brazilian agency CNPq.

Abstract

Many galaxy surveys are planned to release their data over the next few years. Each different survey has its own geometrical limitations, which reflects upon the data as a selection function – the spatial distribution of certain types of galaxies. Given a galaxy map (real or mock), the main goal of this work is to obtain information about how the selection function affects some of the cosmological parameters which can be probed from large-scale structure. A Monte-Carlo Markov Chain method is proposed in order to probe the effects of considering the selection function's parameters as nuisance parameters. The method consists in combining realizations of simulated galaxy catalogs using theoretical matter power spectra, combined with an optimal power spectrum estimator method. Theory and data are then compared in a multivariate Gaussian representing the likelihood function. This Monte-Carlo method has proven robust and capable of probing selection function effects on the cosmological parameters, showing that the simple marginalization over the nuisance parameters might lead to wrong estimates on the cosmology. The method is applied to obtain forecasts for these effects on the upcoming J-PAS Luminous Red Galaxies data and is employed to obtain constraints on the Hubble parameter (H_0), the dark matter density (Ω_c) and two parameters of the equation of state of dark energy (w_0 and w_a).

Resumo

Nos próximos anos, diversos levantamentos de galáxias planejam lançar uma quantidade considerável de novos dados, marcando, assim, o início da chamada “era da cosmologia de precisão”. Cada levantamento possui suas próprias limitações geométricas, que manifestam-se perante os dados na forma de uma função de seleção, ou seja, uma distribuição espacial de cada tipo de galáxia. A partir de um mapa de galáxias (real ou simulado), o principal objetivo desse trabalho foi descobrir como a função de seleção afeta alguns dos parâmetros cosmológicos que podem ser obtidos através de dados futuros de estrutura em larga escala. Portanto, propôs-se um método de Monte-Carlo com cadeias de Markov para estudar os efeitos decorrentes da inclusão dos parâmetros da função de seleção como *nuisance parameters*. Esse método consiste em combinar simulações de catálogos de galáxias, usando um espectro de potências teórico da matéria junto com um estimador ótimo, a fim de obter ambos espectros (teórico e observacional) e compará-los em uma verossimilhança Gaussiana-multivariada. O método de Monte-Carlo provou-se robusto e capaz de demonstrar os efeitos da função de seleção sobre as estimativas dos parâmetros cosmológicos, comprovando que o simples ato de marginalizar sobre os parâmetros não desejados pode levar a estimativas equivocadas na cosmologia em questão. Finalmente, esse método foi aplicado nas estimações do parâmetro de Hubble (H_0), na densidade de matéria escura (Ω_c) e em dois dos parâmetros da equação de estado da energia escura (w_0 e w_a) com o objetivo de prever tais efeitos para dados futuros do levantamento J-PAS com Galáxias Vermelhas Luminosas.

Contents

1	Introduction	1
1.1	Review of General Relativity	2
1.1.1	The Friedmann-Roberson-Walker Metric	5
1.1.2	Λ CDM: The Standard Cosmological Model	7
1.2	Scaling Dark Energy: CPL Parametrization	9
1.3	Cosmology with Current Galaxy Surveys	10
1.3.1	The Sloan Digital Sky Survey (SDSS)	11
1.3.2	The Dark Energy Survey (DES)	14
1.3.3	The Javalambre Physics of the Accelerating Universe Survey (J-PAS)	16
2	Large-Scale Structure of the Universe	19
2.1	Linear Perturbation Theory	20
2.1.1	Newtonian Perturbation Theory	23
2.1.2	Observational Probes of Inhomogeneity	25
2.2	Statistical Analysis of the Large-Scale Structure	29
2.2.1	Correlation Function and Power Spectrum	30
2.3	Gaussian and Log-Normal Density Fields	31
2.3.1	Statistical Properties of a Gaussian Density Field	32
2.3.2	From Gaussian to Log-Normal Density Fields	34
2.3.3	From Poissonian Realizations to Galaxy Mock Catalogs	36
2.4	Power Spectrum Analysis: The FKP Estimator	38
3	Bayesian Statistics in Cosmology	41
3.1	Basic Bayesian Statistics	42
3.1.1	Bayes's Theorem and Marginalization	42
3.1.2	Parameter Estimation	44
3.2	Bayesian Inference for Galaxy Surveys	46
3.3	Monte-Carlo Methods for Bayesian Inference	47

4	Method and Analysis	53
4.1	Method: The MCMaps Algorithm	53
4.2	Analytical Considerations	56
4.2.1	Top-Hat Selection Function	57
4.2.2	Inverse Square Selection Function	60
4.2.3	Gaussian Selection Function	62
4.3	J-PAS LRGs Forecast	68
4.3.1	Individual Redshift Bin Analysis	70
4.3.2	Joint Data Set Analysis	80
5	Conclusions	87
	Appendices	93
A	Moments of a Log-Normal Distribution	93
	Bibliography	97

Chapter 1

Introduction

Ever since the results of two independent Type Ia Supernovae surveys appeared at the end of the 90's [1, 2], the Universe's counter-intuitive behaviour was clear. Evidences for an accelerated expansion cast many doubts about the nature of the Universe. In recent years, this unexpected expansion was assigned to the existence of some kind of dark energy – a concept similar to Einstein's cosmological constant, Λ . In case this energy comes from the vacuum, the current of particle theory physics predicts that its value should be ~ 120 orders of magnitude larger than the one measured. Together with the evidence that most of the Universe's mass is non-luminous and non-interacting – cold dark matter (CDM) –, astronomical observations suggest that approximately 95% of the Universe's constituents are unknown. This Λ CDM paradigm suggests intriguing questions about the nature of these two components, and international efforts have highlighted the importance of searching answers to such questions.

Two decades after the SNe results came out, cosmology started to benefit from an expressive amount of data, lowering measurement uncertainties to just a few percent in many cases. The combined measurements from Cosmic Microwave Background (CMB) and Large Scale Structure (LSS) confirms that our Universe has around 75% of dark energy, 21% dark matter and only 4% of ordinary baryonic matter [3].

Commonly, dark energy is parametrized as the ratio between its pressure and density, though an equation of state, $w_{de} = p_{de}/\rho_{de}$. This parameter defines the main properties of this unknown component. Therefore, most of the current cosmological surveys focus on this parameter. In the case where $w_{de} = -1$, one have just the cosmological constant. However, this parameter may vary according to the observed cosmic epoch, for example, with a simple redshift dependence $w_{de}(z) = w_0 + w_a z/(1+z)$, where w_0 and w_a are free parameters to be constrained by observations [4, 5, 6]. In such cases, one may observe a variation on the growth of structures in the Universe. Considering this parameter's evolution, one can better comprehend the true nature of dark energy, which means distinguishing between a cosmological constant, a scalar field, or even some large scale modification of General Relativity.

To understand the way in which structure forms in the Universe is one of the main challenges of modern cosmology. In the last few decades, a variety of astronomical surveys – such as SDSS, DES, BOSS, and, in the future, J-PAS [7, 8, 9, 10] – focused on measurements of the local distribution of galaxies and other objects. A key tool has been the **baryon acoustic oscillations** (BAOs) [11, 12]: during the epoch when the Universe became neutral and photons decoupled from baryonic matter – called **recombination phase** –, baryons kept information about the acoustic scale from the last phase. Such scale remains imprinted on the matter distribution of the Universe and can be measured as a slightly bigger probability of finding galaxies separated by a characteristic scale. This BAO scale is, today, approximately $105h^{-1}$ Mpc – where h is related to the Hubble constant today, as $H_0 = 100h$ km/s/Mpc – and works as a statistical standard-ruler.

Since dark matter only interacts gravitationally and, as the name suggests, do not emit light, one faces a complicated issue when probing the real matter distribution. One can only detect tracers of the underlying matter density field, such as galaxies, quasars, and clusters. According to Bardeen *et al.*(1986)[13], the density peaks of a Gaussian field are related to the density fields of the **matter halos**. Those gravitational collapsed structures – with a total mass close to $\sim 10^{11}M_\odot$ – are biased in relation to matter distribution.

The present work was divided into four main parts. The present chapter introduces the basic concepts relevant to the development of modern cosmology, from a review of General Relativity, the standard cosmological model, the CPL parametrization for dark energy, and a overview of some of the main present and upcoming galaxy surveys – BOSS, DES and J-PAS. Second part is dedicated to the development of linear perturbation theory and probes of the large scale structure, introducing key concepts such as the matter power spectrum. The third chapter explains the importance of Bayesian statistics for modern cosmology, three of the most used algorithms for Monte-Carlo Markov Chain simulations and how these methods can be applied to the study of galaxy power spectra from galaxy surveys. Finally, chapter 4 is a study of the importance of the selection function on the estimated galaxy power spectrum, with some analytical considerations comparing one of the cases with an MCMC simulation. A forecast is also made, under different circumstances, for J-PAS Luminous Red Galaxies, to probe how its selection function might affect some cosmological parameters estimations.

1.1 Review of General Relativity

The most important tool for the development of modern cosmology was General Relativity. In 1915, Albert Einstein first published his new theory of gravitation unifying spacetime geometry with the behaviour of matter and energy [14]. Einstein’s Field Equations were built based on two simple principles: covariance and equivalence.

The first principle claims that all physical laws should be expressed in a frame-

independent way. This fundamental assumption implies that there is no preferential spacetime structure nor absolute motions. Foremost, one can define a covariant expression for the line element in spacetime as:

$$ds^2 = g_{\mu\nu} dx^\mu dx^\nu, \quad (1.1)$$

where $g_{\mu\nu}$ is the **metric**. It is assumed Einstein's summation convention, with Greek indices ranging from 0 to 3. The first index denotes timelike coordinates, which means $dx^0 = dt$, and the last three are for spacelike coordinates – also expressed with Latin indices [15]. Another useful mathematical tool for curved spacetimes are the Christoffel symbols:

$$\Gamma_{\alpha\beta}^\mu = \frac{g^{\mu\nu}}{2} [g_{\alpha\nu,\beta} + g_{\beta\nu,\alpha} - g_{\alpha\beta,\nu}], \quad (1.2)$$

where the comma stands for the common derivative ($g_{\alpha\beta,\mu} = \partial g_{\alpha\beta} / \partial x^\mu$). The use of this object leads to the concept of covariant derivative – such a tensor's derivative is also a tensor, *e. g.*:

$$A^\mu_{\nu;\alpha} = A^\mu_{\nu,\alpha} - \Gamma_{\nu\alpha}^\beta A^\mu_\beta + \Gamma_{\beta\alpha}^\mu A^\beta_\nu. \quad (1.3)$$

The second concept behind General Relativity, the equivalence principle, guarantees full motion relativity. Within this idea, Einstein states the correspondence between motion in the presence of gravitational fields for a stationary observer and motion for a non-inertial observer in the absence of gravitational fields. If the laws governing a free falling particle – in the presence of a gravitational field – are the same for all, then there is a correspondent motion among free particles in a non-inertial reference frame. In other words, gravitational effects are identical to those resulting through acceleration. Such concept gives rise to two forms of the equivalence principle.

The **weak equivalence principle** refers to spacetime. It states that, in the presence of any gravitational field, a free falling observer will not feel gravity. In this case, spacetime will be that of Special Relativity (Minkowski spacetime). Of course, non-uniform fields are exceptions as they give rise to tidal forces. As for the **strong equivalence principle**, it goes beyond spacetime statements, requiring that all laws of physics assume the same form in the free falling frame as they would in the absence of gravity.

In Special Relativity – and classical mechanics –, free particles move along straight lines; General Relativity has a corresponding proposition. Particles, in curved spacetimes, follow geodesics – paths which are “minimal” in spacetime length. In terms of the **action principle** [16, 17]:

$$\delta S = \delta \int L d\tau = 0, \quad (1.4)$$

where τ is a general parametrization that describes the particle's path. The functional L stands for the *Lagrangian* and, in Newtonian mechanics, represents the difference between kinetic and potential energies. Regarding a free falling observer, who, according to the

equivalence principle, observes a Minkowski spacetime in its neighbourhood, its equation of motion is

$$\frac{d^2 x^\mu}{d\tau^2} = 0; \quad x^\mu = (t, x, y, z), \quad (1.5)$$

which means that the particle's acceleration is null, leading to a Minkowski spacetime

$$d\tau^2 = \eta_{\alpha\beta} dx^\alpha dx^\beta, \quad (1.6)$$

and here $\eta_{\alpha\beta}$ is the Minkowski metric, $\eta_{\alpha\beta} = \text{diag}(-1, 1, 1, 1)$. For a more general set of coordinates, one can write

$$dx^\mu = \frac{\partial x^\mu}{\partial x'^\nu} dx'^\nu. \quad (1.7)$$

Replacing (1.7) into (1.6), results in the geodesic equation:

$$\frac{d^2 x^\mu}{d\tau^2} = -\Gamma_{\alpha\beta}^\mu \frac{dx^\alpha}{d\tau} \frac{dx^\beta}{d\tau}, \quad (1.8)$$

describing particles trajectories in the absence of external forces.

Influenced by **Mach's principle**, Einstein developed his field equations based on the idea that the rest frame of matter is an inertial frame. From conservation laws, one can assume the zero divergence of an **energy-momentum tensor** – the source of gravitation:

$$T^{\mu\nu}{}_{;\nu} = 0, \quad (1.9)$$

where T^{00} is the energy density; T^{12} is the x-component of current for the y-momentum; and so on[16]. When relating this object to the spacetime geometry, second derivatives of the metric appear, representing the spacetime curvature. The only choice leading to a tensor is the **Riemann tensor**

$$R^\lambda{}_{\mu\nu\kappa} = \Gamma_{\mu\nu,\kappa}^\lambda - \Gamma_{\mu\kappa,\nu}^\lambda + \Gamma_{\mu\nu}^\eta \Gamma_{\kappa\eta}^\lambda - \Gamma_{\mu\kappa}^\eta \Gamma_{\nu\eta}^\lambda. \quad (1.10)$$

This object leads to the **Ricci tensor** when contracting two indices:

$$R_{\mu\nu} = \Gamma_{\mu\nu,\alpha}^\alpha - \Gamma_{\mu\alpha,\nu}^\alpha + \Gamma_{\mu\nu}^\eta \Gamma_{\alpha\eta}^\alpha - \Gamma_{\mu\alpha}^\eta \Gamma_{\nu\eta}^\alpha, \quad (1.11)$$

and to the **Ricci scalar** R contracting the last two indices:

$$R = g^{\mu\nu} R_{\mu\nu}. \quad (1.12)$$

Using the definitions from the last two expressions, the Einstein tensor emerges as:

$$G_{\mu\nu} \equiv R_{\mu\nu} - \frac{1}{2} g_{\mu\nu} R, \quad (1.13)$$

and it obeys the property that:

$$G^\mu{}_{\nu;\mu} = \left(R^\mu{}_\nu - \frac{1}{2}g^\mu{}_\nu R \right)_{;\mu} = 0 . \quad (1.14)$$

Now, since both the energy-momentum tensor and (1.13) have zero covariant divergence, it seems fair to assume that they are proportional to each other:

$$G_{\mu\nu} = 8\pi GT_{\mu\nu} - g_{\mu\nu}\Lambda. \quad (1.15)$$

These covariant equations, linking spacetime geometry with energy and matter, are Einstein's gravitational equations. The second term on the right-hand side of (1.15) is the *cosmological constant*, introduced by Einstein in a 1917 paper [18] to counter-balance gravity and leading to a static, but unstable Universe. Ironically, the cosmological constant is, today, the prime candidate for causing the observed accelerated expansion.

It is also important to highlight that, on the weak-field and quasi-static limit, these equations reflect Newtonian gravity:

$$\begin{cases} g_{00} = -(1 + 2\phi) \\ \nabla^2\phi = 4\pi G\rho \end{cases} \quad (1.16)$$

where ϕ is the Newtonian gravitational potential.

1.1.1 The Friedmann-Roberson-Walker Metric

The main assumption of modern cosmology is that our place in the Universe is no different from any other. This is called the **cosmological principle**, and follows directly from it that our Universe is both **isotropic** (it is identical in all direction) and **homogeneous** (it has constant density in large scales). Generally speaking, isotropy affirms that there are no geometrically preferred spatial directions, while homogeneity requires that at any moment in time every spatial point “looks the same”. These symmetries allow the topology to be foliated by globally extended instants – spacelike hypersurfaces–, resulting in a notion of **cosmic time**. Also, a class of naturally privileged observers appear: the **fundamental observers**, who are at rest with respect to the matter content of the Universe. These fundamental observers's worldlines are orthogonal to the time foliation and their watches measure the cosmic time [19].

Combining this concept of time with isotropy and the known fact that the Universe is in expansion – as discovered by Edwin Hubble in 1929 [15, 16, 17] –, it is straightforward to conclude that the metric must assume the following form:

$$ds^2 = -dt^2 + a^2(t) [f^2(r)dr^2 + g^2(r)(d\theta^2 + \sin^2\theta d\phi^2)] . \quad (1.17)$$

As a consequence of translational symmetry, the radial and transverse components of the metric can be decomposed. Distances are measured as a product of a time-dependent **scale factor** $a(t)$ and a time-independent **comoving coordinate** r [16]. As both functions $f(r)$ and $g(r)$ are arbitrary, they can be chosen in a way that resembles Euclidean space: $f(r) = 1$ and $g(r) = r^2$. However, a more general form of (1.17) can be written in a way that both open, flat, and closed geometries are included:

$$ds^2 = -dt^2 + a^2(t) [dr^2 + S_k^2(r)(d\theta^2 + \sin^2 \theta d\phi^2)], \quad (1.18)$$

where the function $S_k(r)$ stands for the three geometrical topologies:

$$S_k(r) = \frac{\sin(\sqrt{K}r)}{\sqrt{K}r} = \begin{cases} \sin r, & K = 1 \text{ (open)} \\ r, & K = 0 \text{ (flat)} \\ \sinh r, & K = -1 \text{ (closed)} \end{cases} \quad (1.19)$$

Redshift

A useful concept to establish at this point is **redshift**. Hubble's law states that nearby galaxies in the local Universe move away from each other at a rate $v = Hx$. As the physical separation of two fundamental observers is $a(t)dr$, Hubble's law can be rewritten as

$$H(t) = \frac{\dot{a}(t)}{a(t)}. \quad (1.20)$$

So, at small scales, one can define redshift as

$$\frac{\lambda_{obs}}{\lambda_{source}} \equiv 1 + z \simeq 1 + \frac{v}{c}. \quad (1.21)$$

A more general expression for redshift comes when considering the photon's null geodesic. For a radial geodesic, the metric yields [16]:

$$r = \int \frac{dt}{a(t)}. \quad (1.22)$$

Since the comoving distance is constant for this case, the integral above leads to

$$\frac{dt_{source}}{dt_{obs}} = \frac{a(t_{source})}{a(t_{obs})}, \quad (1.23)$$

which means that there's a time-dilation for photons emitted from distant galaxies, which is proportional to the expansion of the Universe. This effect also appears on the observed

wavelength, resulting in a more general expression for redshift:

$$1 + z \equiv \frac{\lambda_{obs}}{\lambda_{source}} = \frac{1}{a(t)}. \quad (1.24)$$

where $a(t = t_0) = 1$.

The concept of redshift is fundamental for many cosmological analysis, including the measurement of distances in galaxy surveys and the construction of a 3D map of the Universe.

1.1.2 Λ CDM: The Standard Cosmological Model

To build a standard model for cosmology, one must define the right-hand side of (1.15), the energy-momentum tensor. Such object must also obey isotropy and homogeneity, which makes the *perfect fluid* a suitable candidate.

$$T^{\mu\nu} = (\rho + p) \frac{dx^\mu}{ds} \frac{dx^\nu}{ds} - g^{\mu\nu} p. \quad (1.25)$$

Given comoving coordinates and the FRW metric, (1.25) becomes

$$T^\mu_\nu = \begin{bmatrix} -\rho & 0 & 0 & 0 \\ 0 & p & 0 & 0 \\ 0 & 0 & p & 0 \\ 0 & 0 & 0 & p \end{bmatrix} \quad (1.26)$$

Now, using the FRW metric (1.18) together with the energy-momentum tensor (1.26), it is possible to find dynamical equations for the scale factor applying Einstein's field equations. Firstly, the nontrivial components of the Einstein tensor (1.13) are

$$\begin{aligned} G_{00} &= \frac{3}{a^2}(\dot{a}^2 + K), \\ G_{ij} &= \frac{1}{a^2}(2a\ddot{a} + \dot{a}^2 + K)\delta_{ij}, \end{aligned} \quad (1.27)$$

where δ_{ij} is the *Kronecker delta*. Including the Einstein Metric Tensor leads to two independent equations for the matter-energy in the Universe

$$\left(\frac{\dot{a}}{a}\right)^2 = \frac{8\pi G}{3}\rho - \frac{K}{a^2} + \frac{\Lambda}{3} \quad (1.28)$$

$$\frac{\ddot{a}}{a} = -\left(4\pi Gp + \frac{1}{2}\left[\left(\frac{\dot{a}}{a}\right)^2 + \frac{K}{a^2}\right]\right) + \frac{\Lambda}{3}. \quad (1.29)$$

Combining these two expressions with the equations of state for all the components of the

Universe allows to determine $a(t)$, $\rho(t)$ and $p(t)$ [20]. The first of them, equation (1.28), could be used to determine the value of K , *i.e.*, the spatial curvature of the Universe. At the present epoch, $t = t_0$, $a(t_0) = 1$,

$$K = \frac{8\pi G}{3}\rho(t_0) - \underbrace{\dot{a}^2(t_0)}_{H_0^2} + \frac{\Lambda}{3} \equiv H_0^2(\Omega_0 - 1). \quad (1.30)$$

Here, H_0 is the Hubble constant today and $\Omega \equiv \rho/\rho_{cr}$. The critical density, $\rho_{cr} \equiv 3H_0^2/8\pi G = 8.098 h^2 \times 10^{-11} eV^4$, is an important parameter in cosmology. The ratio of energy-matter density to critical density, Ω , defines not only the curvature of the Universe but its fate. If $\Omega > 1$, the Universe will be temporally finite to the future, meaning it will have an end, collapsing on itself, unless $\Lambda > 0$, in which case it may still expand forever; if $\Omega < 1$, the Universe will also expand forever; the last case, where $\Omega = 1$, *i.e.*, $\rho_0 = \rho_{cr}$, the Universe will be temporally infinite in future.

Combining equations (1.28) and (1.29) gives

$$\frac{\ddot{a}}{\dot{a}} = -\frac{4\pi G}{3}(\rho + 3p), \quad (1.31)$$

Which shows that the acceleration is independent of K . It is common to express (1.28) in terms of the Universe's components: pressureless matter [$\rho_m = (\rho_C + \rho_b) \propto a^{-3}(t)$], radiation [$\rho_r \propto a^{-4}(t)$] and vacuum energy ($\rho_\Lambda = \text{constant}$). In terms of the Hubble constant scaled by its current value, (1.28) can be expressed as

$$E^2(t) \equiv \frac{H^2(t)}{H_0^2} = [\Omega_\Lambda + \Omega_K a^{-2} + \Omega_m a^{-3} + \Omega_r a^{-4}] \quad (1.32)$$

or

$$E^2(t) = \sum_i \Omega_i a^{-3(1+w_i)} \quad (1.33)$$

where w_i stands for the equation of state for each component:

$$w_i = \begin{cases} 0 & , \text{Matter (dark and baryonic)} \\ 1/3 & , \text{Radiation} \\ -1 & , \text{Vacuum or cosmological constant} \\ -1/3 & , \text{Curvature} \end{cases} . \quad (1.34)$$

Recalling the fact that $(1+z) = a^{-1}(t)$, equation (1.33) can also be written as

$$E^2(z) = \sum_i \Omega_i (1+z)^{3(1+w_i)} \quad (1.35)$$

So, now, the comoving distance at a given redshift can be expressed as

$$r(z) = \frac{1}{H_0} \int_0^z \frac{dz'}{E(z')}. \quad (1.36)$$

meaning that such measurements depend on the content of the Universe.

In summary, the background smooth Universe can be described by a FRW metric and a perfect fluid with a cosmological constant. Distance measurements are related to the scale factor, which evolves in time according to the Friedmann equations. The standard cosmological model presents an accelerated expanding solution with a flat geometry in a cosmological constant dominated universe. Also, the measured baryonic density is known to be insufficient, leading to the need for dark matter. However, a singularity occurs when the cosmic time t reaches zero, $a(t \rightarrow 0) \rightarrow 0 \therefore \rho(t \rightarrow 0) \rightarrow \infty$, what it is called the **Big Bang**.

1.2 Scaling Dark Energy: CPL Parametrization

As was stated before, a cosmological constant – or vacuum energy – is about 120 orders of magnitude lower than the theoretical predicted value. Chevallier and Polarski (2001) proposed that the present energy density might be a slowly varying cosmological constant [4]. According to those authors, a minimally coupled scalar field ϕ , called **quintessence**, slowly rolls down its potential in a way that it can present a negative pressure like that which is required for dark energy [21]. The standard cosmological models suggests that Λ has a constant equation of state $p_{DE} = w_{DE}\rho_{DE}$, with $w_{DE} = -1$. The Chevallier-Polarski-Linder (CPL) parametrization suggests that the equation of state might evolve with redshift, $w_{DE} = w_{DE}(z)$, in a particular way [4, 5].

In 2002, Linder proposed a parametrization of the equation of state for dark energy based on the mapping of the expansion history of the Universe [5]. Starting from the observed distance-redshift relation $d(z) = (1+z)\eta(z)$, where $\eta(z)$ is the conformal time – time light travels a comoving distance $dx = d\eta = dt/a$ [15] –, and assuming a flat Universe,

$$\eta(z) = \int_0^z \frac{dz'}{E(z')}. \quad (1.37)$$

Here, one can rewrite (1.28), defining $\rho_K = -\rho_{cr}K/H^2$ and $\rho_\Lambda = \rho_{cr}\Lambda/3H^2$, as

$$H^2(t) = \frac{8\pi G}{3} \sum_i \rho_i(t). \quad (1.38)$$

Employing the first law of thermodynamics for this case, $d(\rho a^3)/dt = -pd(a^3)/dt$, leads to

$$\dot{\rho}/\rho = -3H(z)[1 + p/\rho] \equiv -3H(z)[1 + w(z)] \quad (1.39)$$

where the possibility of redshift-dependent evolution for w is explicit expressed.

The accelerated expansion strongly suggests a dark component with negative equation of state in addition to matter. Putting together (1.37) and (1.35), one can express (1.39) as

$$\eta(z) = \frac{1}{H_0} \int_0^z dz' \left[\Omega_m (1+z)^3 + (1 - \Omega_m) e^{-3 \int_0^{1+z'} d \ln(1+z'') [1+w(z'')] } \right]^{1/2} \quad (1.40)$$

where the radiation component was neglected because it is too small compared to the others in the present epoch.

As shown by Chevalier and Polarski (2001), $w(z)$ can result from a scalar field equation but it does not allow a model independent parametrization. Alternatively, some parametrizations have been proposed in the literature. In his 2002 paper, Eric Linder showed that a simple linear parametrization, such as $w(z) = w_0 + w_1 z$, brings problems for redshifts $z > 1$, since the exponential in (1.37) results in $(1+z)^{3(1+w_0-w_1)} e^{3w_1 z}$. Instead, he proposes a new parametrization that also works for redshifts $z > 1$ [5]:

$$w(z) = w_0 + w_a \frac{z}{1+z}. \quad (1.41)$$

This is the CPL parametrization for the equation of state of dark energy. In this case, the exponential in (1.37) results in $(1+z)^{3(1+w_0+w_a)} e^{-3w_a z/(1+z)}$.

Such parametrization presents various advantages:

1. A two-dimensional parameter space;
2. Reduces itself to the linear case for low redshifts;
3. Behaves well for higher redshifts;
4. Can reconstruct scalar field equations of state and their distance-redshift relations;
5. Shows a satisfactory sensitivity to observational data.

A simple physical explanation for the CPL parametrization comes from the slow roll approximation [15, 16]. One can interpret $dw/d \ln(1+z)|_{z=1} = w_a/2$ as a natural measure, directly related to the slow roll factor V'/V . In this case, $z = 1$ is a region where this scalar field could be evolving from a matter-dominated epoch to a dark energy-dominated one.

1.3 Cosmology with Current Galaxy Surveys

Galaxy surveys are one of the main tools in cosmology. From these experiments one can study some of the most important cosmological tools like LSS, weak and strong gravita-

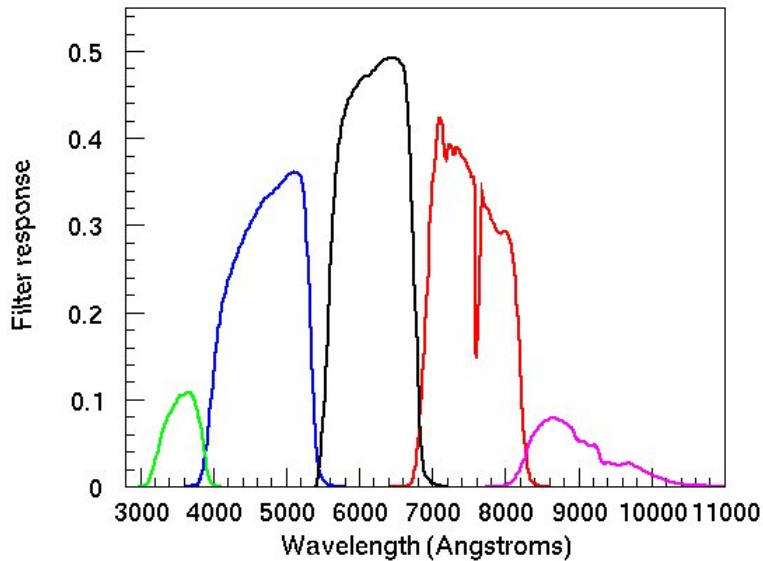


Figure 1.1: The SDSS-III camera filter throughput curves.

Figure from <http://www.sdss3.org>

tional lensing, BAOs, galaxy evolution, and many others. This Section presents some of the main cosmological galaxy surveys, their differentials, main goals and achievements.

1.3.1 The Sloan Digital Sky Survey (SDSS)

The Sloan Digital Sky Survey, named after the Alfred P. Sloan Foundation, is one of the most – if not *the most* – important cosmological survey of all times. Originally designed to do both photometry and spectroscopy, five years after the first light, SDSS had a deep multi-filter imaging of the sky in over 8000 square degrees with spectra for more than 700,000 astronomical objects. After its second phase, from 2005 to 2008, it had surveyed half of the northern hemisphere sky mapping the three-dimensional clustering of more than one million galaxies, 150,000 Quasars and 500 Type Ia Supernovae, leading to a much deeper understanding of the Universe.

Sloan’s photometric system uses 5 colors (u' , g' , r' , i' and z')[7] with accurate astrometry (≤ 10 arcsec) and a multi-object spectrometer designed to cover from near-UV to near-IR ($\sim 3000 - 10,000\text{\AA}$) to a limiting magnitude of $r' \sim 23$. The telescope has a 2.5m aperture with a focal ratio of f/5 producing a flat field of 3° with a plate scale of 16.51 arcsec/mm, and is situated at the Apache Point Observatory, New Mexico, at a height of 2,800m.

Sloan’s main camera consists of 54 CCDs covering 2.3° of the sky and operates in a TDI (Time Delay and Integrate). This system allows to survey the sky in a way that the

CDDs perform 5-color photometry simultaneously. The time spent for each CDD for each part of the sky (effective integration time) is 55 seconds [7].

The northern survey's footprint was chosen to minimize Galaxy foreground pollution – it has a nearly elliptical shape, 130° E-W by 110° N-S, close to the North Galactic Pole. It also has 45 big stripes in the northern region separated by 2.5° – each one scanned twice – completed with an offset perpendicular scan in order to interlace photometric columns, allowing some overlap regions.

Main cosmological goals for this international effort were focused on measuring the local LSS in the Universe ($z \lesssim 0.5$), and obtaining the galaxy power spectrum up to \sim Gpc scales. Such measurements allowed to constrain the shape of the galaxy power spectrum predicted by the linear perturbation theory, leading to the first reliable measurement of BAOs [11]. The photometric redshift (*photo-z*) data from Sloan is also powerful a tool for today's cosmology since it allows for a deep and complete image of thousands of square degrees.

Sloan's timeline

SDSS has been running for several years and had many different projects divided into four phases.

- **SDSS-I (2000-2005):** Along the first five years, Sloan imaged around 8,000 square degrees of the northern sky using its 5-color photometric system and obtained spectra from galaxies and quasars for more than 5,700 square degrees of the original photometric field;
- **SDSS-II (2005-2008):** The observations were extended to explore stellar evolution in the Milky Way together with the **Sloan Supernova Survey**, finding 197 Type Ia SNe events to use as standard candles. The **Sloan Legacy Survey** observed more than 2 million astronomical objects with spectra for over 800,000 galaxies and 110,000 quasars, allowing for the first accurate LSS investigation and the first detection of BAOs;
- **SDSS-III (2008-2014):** The third phase began in 2008 and was divided into 4 different surveys: APOGEE, for Galactic Evolution; MARVELS, for exoplanetary research; SEGUE-2, for stellar research; and **BOSS**, the spectroscopic galaxy survey to measure the expansion rate of the Universe through baryon acoustic oscillations (more details on the next subsection);
- **SDSS-IV (2014-2020):** The current generation of SDSS experiments focus on precision cosmology and measurements of the high- z Lyman- α forest. SDSS will also extend the APOGEE experiment and initiate detailed spatially resolved spectroscopy on nearby galaxies to investigate their internal structure.

The Baryon Oscillation Spectroscopic Survey (BOSS)

The Baryon Oscillation Spectroscopic Survey is one of the four experiments in Sloan's phase III (SDSS-III) and its main purpose is to map the spatial distribution of quasars and Luminous Red Galaxies (LRGs) using its multiple-object spectrograph with 1000 optic fibres to obtain redshift for 1.5 million galaxies up to $z = 0.7$ and Lyman- α spectra of 160,000 quasars at $2.2 < z < 3$, covering 10,000 square degrees of the northern sky. The survey uses a rebuilt spectrograph based on the original SDSS, however, using smaller fibres and improved detectors allowing for a wider wavelength range (360-1000 nm). When completed, the survey will have used more than 2000 unique spectroscopic aluminium plates, each one covering a circular field of 3° diameter. This configuration allows the BOSS experiment to exceed a density of astronomical objects for LRGs and observe a comoving density of $\bar{n} = 2 - 3 \times 10^{-4} h^3 \text{Mpc}^3$ with clustered galaxies reaching a bias of $b \sim 2$.

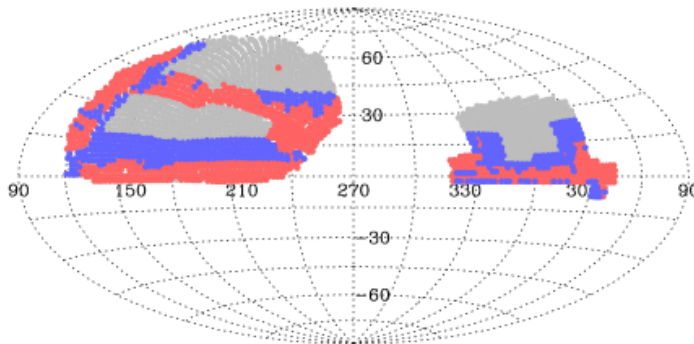


Figure 1.2: The area covered by BOSS 2208 spectroscopic plates in equatorial coordinates. Colours are due the sequence of plates used. Figure from [9]

Mapping these two types of tracers – quasars and LRGs –, provides solid data to probe the baryon acoustic scale (BAO) imprinted since the early Universe (see Section 2.1.2). Using the BAO scale as a standard-ruler, the SDSS collaboration hopes to measure the angular diameter distance with 1% precision for redshifts between $0.3 < z < 0.55$ for LRGs. The distribution of quasars at $z \sim 2.5$ provides the same measurement, but with a 1.5% precision, allowing to probe the cosmic expansion rate, the Hubble flow, $H(z)$, with 1 – 2% precision. This precise measurement can also be used to test for alternative theories of gravity [22].

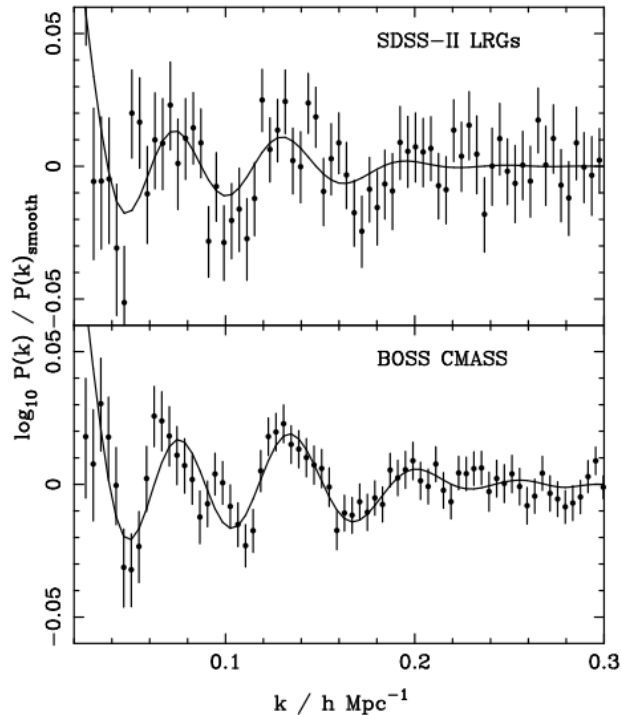


Figure 1.3: Comparison of the power spectrum of SDSS-II LRGs and BOSS galaxies. Solid lines are the best-fit models [23]

The quasar survey performed by BOSS uses a pioneering strategy, measuring BAOs at high redshifts – from 2.5 up to 3.5 – through Lyman- α forest absorption lines using quasars as background light. The experiment can detect the Ly- α trough when it reaches $z = 2$ and detects them until it becomes opaque around $z \sim 4$.

Together with the cosmological constraints, BOSS will obtain a numerous sample of galaxies and quasars, ideal to understand galaxy formation and evolution. BOSS’s data also contains valuable information about metallicity of stars, through its spectra, and can be used to probe how and when galaxies were formed.

1.3.2 The Dark Energy Survey (DES)

As the name suggests, the Dark Energy Survey was designed to investigate four of the major probes of dark energy: Type Ia Supernovae, BAOs, galaxy clusters and weak gravitational lensing. The first two (SNe and BAO) are ”purely geometrical”, and constrain the whole expansion of the Universe, while the other two (clusters and WL) probe both the growth of structures and the expansion. DES is designed to probe the origin of the observed accelerated expansion in the Universe. This international collaboration has members from the U.S., U.K., Spain, Brazil, Switzerland, and Germany. It will map 300 million galaxies over 5000 square degrees with sub-arcsec resolution for images using a 570-Megapixels wide-field digital camera, the DECam, built for the Blanco 4m telescope

in Chile [8].

In addition to a wide area (more than 10% of the sky), the Dark Energy Survey will dedicate 10% of its time to discover and measure light curves for more than 1900 Type Ia Supernovae using $r'i'z'$ filters. DES's Supernovae ranges from redshift 0.3 to 0.75, and will be observed through repeated imaging of a 40 square degree region. SNe estimates on distances are excellent probes constrain dark energy.

Using galaxy clusters as cosmological probes, the DES collaboration hopes to understand the origin of the gravitational potentials, Ψ and Φ , and the evolution of the scale factor, $a(t)$. The survey was primarily designed to use detailed optical measurements of clusters, photometric redshifts, and to take advantage of the synergy with cluster measurements from the South Pole Telescope (SPT). This strategy allows to use the integrated Sunyaev-Zel'dovich effect as a robust indicator of cluster mass for all SPT clusters up to $z = 1.3$.

One of the most important features in DES is its ability to measure weak lensing shear of galaxies as a function of redshift. The structure's growth rate and the cosmic expansion history are very sensitive to the evolution of the statistical pattern of WL distortions and the cross-correlation of foreground galaxies and background shear [24]. The Dark Energy survey is designed to measure shapes and photometric redshifts for over 300 million galaxies, in a 5000 square degree area, with great control of images quality, enabling it to measure accurately the lensing of LSS.

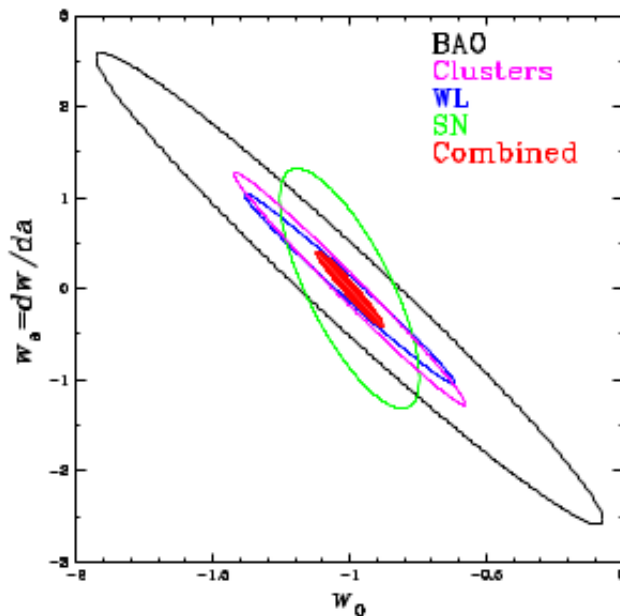


Figure 1.4: The 68% confidence level regions for the Dark Energy Survey forecast on constraints for the CPL parametrization, w_0 and w_a . Each of the probes are combined with Planck CMB priors and the red region shows the combination of all four dark energy probes. Figure from [25].

When forecasting dark energy parameters constraints for DES, the collaboration followed the approach suggested by the Dark Energy Task Force in [6], which uses the CPL parametrization (Section 1.2). The DETF defined a figure of merit, proportional to the area in the $w_0 - w_a$ plane that encloses the 95% confidence level region. The DES collaboration's forecasts for dark energy, using each of the cosmological probes, are shown in Figure 1.4 .

The comparison for both techniques might shine a light on modifications to General Relativity proposed to explain the effects of dark energy [8]. The first year of data has already be taken and, over four more years, DES will reach redshifts of $0.2 < z < 1.2 - 2$ using photometry on broad band filters – g', r', i' and z' – in the southern hemisphere.

1.3.3 The Javalambre Physics of the Accelerating Universe Survey (J-PAS)

Situated at Sierra de Javalambre, in Spain, the J-PAS telescope has a 2.5m aperture and will perform a photometric galaxy survey using a combination of 54 narrow-band and 5 broad-band filters (*ugriz* SDSS's filter system)[10]. Using a 1.2 Gigapixels camera –JPCam, the second largest camera in the world –, J-PAS will be able to produce high-quality images, mapping over 8500 square degrees of the sky, covering all visible electromagnetic spectrum (from 3500 to 10000Å). The J-PAS collaboration includes several researchers from Brazilian and Spanish institutions and it also counts on two 80cm telescopes: one at Javalambre Sierra (JPlus); and another in Chile (SPlus).

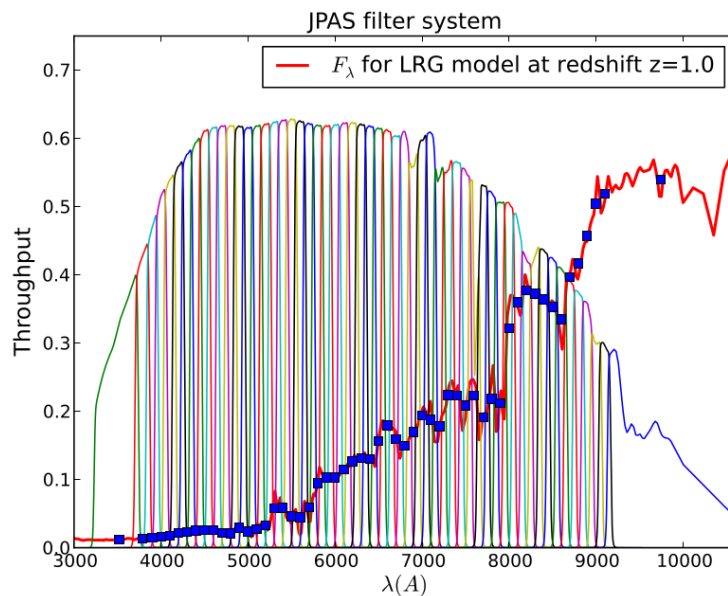


Figure 1.5: Filter system used for J-PAS photometry, together with a early type galaxy redshifted spectrum, showing the flux produced by the observed filters.

Benitez *et al.* (2009) showed that medium-band filters combined with a narrow-band filter system is much more efficient for photometric redshifts than a regular broad band filter system [26]. Even though narrow-band imaging is not very efficient for the observation of individual object, it is extremely useful for cosmological purposes. Benitez *et al.* (2009) also argued that using a system of adjacent $\sim 100\text{\AA}$ -width filters, one can reach $\sim 0.3\%$ photometric redshift precision for LRGs. Such measurements allow J-PAS to probe the BAO scale up to $z < 1.1$ for this type of galaxy. The survey's strategy consists in combining LRGs measurements together with blue galaxies through OII emission lines, up to $z < 1.35$, and quasars, up to $z < 4$, maximizing the effective volume over which the BAO scale can be measured.

The new strategy allows to probe information about the cosmological fluctuations, leading to better constraints for cosmological parameters. The forecasts for J-PAS on the CPL parameters for dark energy (Figure 1.6) were obtained from BAOs and cluster counts using Planck and DETF Stage-II priors. Both probes are comparable with one another in constraining these parameters.

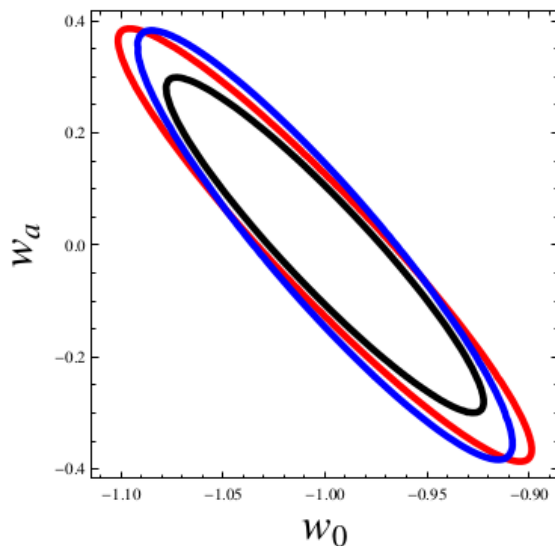


Figure 1.6: 95% Contour level regions for the dark energy equation of state parameters, w_0 and w_a . In (red) is the cluster counts only, in (blue) BAOs only and (black) shows the BAOs combined with cluster counts. Figure from [10]

Even though the main goal for J-PAS was originally the study of BAOs, its unique design allows to analyse many other cosmological probes like weak lensing, galaxy evolution, quasars with excellent photo- z precision [27], and Type Ia Supernovae [28]. The J-PAS filter system allows a precise multi-tracer analysis achieving high completeness, while having accurate photo- z , by a combination of LRGs up to $z \sim 1$, emission-line galaxies (ELGs) up to $z \sim 1.4$, Ly- α emitters (LAEs) and Quasars up to $z \sim 5$, producing a deep and wide three-dimensional map of the Universe over 1/5 of the sky.

Chapter 2

Large-Scale Structure of the Universe

Even though the cosmological principle states that the Universe is homogeneous, on small scales one can observe complex and inhomogeneous structures such as clusters, voids, filaments, walls, galaxies, stars, etc. The attractive nature of gravity forms these structures during the evolution of the Universe. Groups and clusters of galaxies are not distributed in a random way, instead, their positions in the sky are correlated. The three-dimensional galaxy distribution revealed by redshift surveys shows fascinating structures like the Great Wall, a galaxy structure with a size of $\sim 100 Mpc h^{-1}$ [18], or nearly spherical regions with no bright galaxies inside, called **voids**, with diameters of $\sim 50 Mpc h^{-1}$. These observations suggest that there might exist even larger structures and that at larger scales the Universe is homogeneous.

These small-scales observations, together with the CMB anisotropies with relative fluctuations of $\delta T/T \sim 10^{-5}$, suggest that the present Universe started from small inhomogeneities at redshift $z \sim 1100$. When studying how matter reacts under gravity in an expanding Universe, it is useful to consider the **relative density contrast**,

$$\delta(\mathbf{r}, t) \equiv \frac{\rho(\mathbf{r}, t) - \bar{\rho}(t)}{\bar{\rho}(t)}, \quad (2.1)$$

where $\bar{\rho}(t)$ is the mean density at a time t . Density fluctuations grow due to gravitational interaction, as over-dense regions increase their density contrast while under-dense regions decrease – which means that $|\delta|$ increases.

Section 2.1 will develop the linear theory of perturbation, considering perturbations in an FRW background Universe, in both relativistic formulation and in the Newtonian approximations. The main formulas are then used to evolve Einstein-Boltzmann equations in the **CAMB code** [29]. Moving forward, Section 2.3 develops the statistical properties of the Universe from Gaussian density fields. Then, galaxy mocks and some fundamental concepts like the selection function, bias, shot-noise, and cosmic variance are discussed.

Finally, Section 2.4 presents the statistical tools for the observed LSS, in particular the **FKP estimator** for power spectrum analysis using an optimal weighting scheme [30, 31]. These are fundamental tools for the method presented in Chapter 4.

2.1 Linear Perturbation Theory

A common method to solve complicated coupled differential equation in physics is perturbation theory. Matter and energy affect gravity and *vice-versa*. Photons are affected by Compton scattering with free electrons, while electrons are coupled to protons, and both are affected by gravity. Even if dark matter do not interact with those, it also affects the metric, together with neutrinos [15]. The most usual solution in this case is to solve the Boltzmann equations for each of the species in a perturbed solution around an FRW background.

The starting point for this formalism is the collisional Boltzmann equation,

$$\frac{df}{dt} = \mathcal{C}[f], \quad (2.2)$$

where $\mathcal{C}[f]$ accounts for all the collisions a species might suffer during the evolution of the Universe and f is the occupation function, or a probability distribution function. One can open the total derivative in Eq. (2.2) and rewrite it as:

$$\frac{df}{dt} = \frac{\partial f}{\partial t} + \frac{dx^i}{dt} \frac{\partial f}{\partial x^i} + \frac{dp}{dt} \frac{\partial f}{\partial p} = \mathcal{C}[f], \quad (2.3)$$

which allows to investigate the behaviour for each component.

To obtain the left hand side of (2.3), it is necessary to account for perturbations in the background metric described by (1.17). These are described by two potentials, with dependence in both space and time, $\Psi(\mathbf{r}, t)$, the Newtonian potential, and $\Phi(\mathbf{r}, t)$, the curvature potential, related to the perturbations in spacial curvature. In **conformal-Newtonian gauge**, the non-vanishing terms of the perturbed metric are

$$\begin{cases} g_{00}(\mathbf{r}, t) = -(1 + 2\Psi(\mathbf{r}, t)); \\ g_{ij}(\mathbf{r}, t) = \delta_{ij}a^2(t)(1 + 2\Phi(\mathbf{r}, t)); \end{cases} \quad (2.4)$$

or

$$ds^2 = -(1 + 2\Psi(\mathbf{r}, t))dt^2 + a^2(t)(1 + \Phi(\mathbf{r}, t)) [dr^2 + S_k^2(r)(d\theta^2 + \sin^2 d\phi^2)] \quad (2.5)$$

With the perturbed metric one can write the relativistic version of (2.3) as:

$$\frac{df}{dt} = \frac{\partial f}{\partial t} + \frac{dx^i}{dt} \frac{\partial f}{\partial x^i} + \frac{dp}{dt} \frac{\partial f}{\partial p} + \frac{d\hat{p}_i}{dt} \frac{\partial f}{\partial \hat{p}_i}, \quad (2.6)$$

leading to

$$\frac{\partial f}{\partial t} + \frac{\hat{p}_i}{a} \frac{p}{E} \frac{\partial f}{\partial x^i} - \frac{\partial f}{\partial E} \left[\frac{p^2}{E} \dot{\Phi} + \frac{\partial \Psi}{\partial x^i} \frac{p \hat{p}_i}{a} + \frac{p^2}{E} H \right] = \left(\frac{\partial f}{\partial t} \right)_c. \quad (2.7)$$

This is one of the main equation for the study of perturbation's evolution together with the perturbed Einstein Field Equations. As the evolution of the Fourier modes \mathbf{k} depends primarily on the magnitude of \mathbf{k} , it is simpler to develop the perturbation formalism in Fourier space instead of real space.

The Universe's constituents can be divided in two types: relativistic, like photons and neutrinos; and non-relativistic, like dark matter and baryons. In Fourier space, the perturbations depend not only on k and η (conformal time) but also on $\hat{k} \cdot \hat{p} \equiv \mu$. The fractional temperature difference for photons can be expressed as

$$\Theta(k, \mu, \eta) \equiv \int d^3r \frac{\delta T(\mathbf{r}, \eta)}{T(\mathbf{r}, \eta)} e^{-ikr\mu}. \quad (2.8)$$

Or, in a general way, defining the l th multipole moment for the photon's temperature field,

$$\Theta_l = \frac{1}{(-i)^l} \int_{-1}^1 \frac{d\mu}{2} \Theta(\mu) \mathcal{L}_l(\mu) \quad (2.9)$$

where \mathcal{L}_l is the Legendre polynomial of l -th order. While higher Legendre polynomials are important on small scales, the first ones govern the large-scale structure behaviour. A similar formulation can describe neutrino perturbations, expressed by $\mathcal{N}(k, \mu, \eta)$. As for the non-relativistic components, dark and baryonic matter, their descriptions are given by the first two perturbation momenta in Fourier space, the density contrast $[\tilde{\delta}(k, \eta)$ and $\tilde{\delta}_b(k, \eta)]$ and the velocity $[\tilde{v}(k, \eta)$ and $\tilde{v}_b(k, \eta)]$.

Combining the Boltzmann equation, (2.7), for photons, neutrinos, baryons, and dark matter leads to a set of coupled equations for the evolution of each component [15]. Using primes to denote the conformal time derivative, $' = d/d\eta$, one has:

$$\Theta' + ik\mu\Theta + \Phi' + ik\mu\Psi = -\tau' \left[\Theta_0 - \Theta + v_b\mu - \frac{1}{2}\mathcal{L}_2(\mu)(\Theta_2 + \Theta_{P2} + \Theta_{P0}) \right], \quad (2.10)$$

$$\Theta'_P + ik\mu\Theta_P = -\tau' \left[-\Theta_P + \frac{1}{2}[1 - \mathcal{L}_2(\mu)(\Theta_2 + \Theta_{P2} + \Theta_{P0})] \right], \quad (2.11)$$

$$\delta'_b + ikv_b = -3\Phi' \quad (2.12)$$

$$v'_b + \frac{a'}{a}v_b + ik\Psi = \tau' \frac{4\rho_\gamma}{3\rho_b} [3i\Theta_1 + v_b], \quad (2.13)$$

$$\delta' + ikv = -3\Phi', \quad (2.14)$$

$$v' + \frac{a'}{a}v = -ik\Psi, \quad (2.15)$$

and

$$\mathcal{N} + ik\mu\mathcal{N} = -\Phi' - ik\mu\Psi. \quad (2.16)$$

Equations (2.10) and (2.11) refer to photons, where Θ_P is called **strength of polarization** and τ is the optical depth – the number of photon-electron interactions from η to η_0 . The following four equations – (2.12), (2.13), (2.14), and (2.15) – are related to the baryonic and dark matter evolution, respectively. The last one, (2.16), governs the perturbations in the distribution of massless neutrinos. So far, there are only seven equations for nine variables – $\Theta, \mathcal{N}, \delta, v, \delta_b, v_b, a, \Phi$, and Ψ . The last “missing” ones, involving the two perturbation potentials, come from perturbing Einstein’s field equations.

Perturbations on Einstein Field Equations

The time-time component, G^0_0 , can be expressed as

$$G^0_0 = g^{00}G_{00} = (-1 + 2\Psi)R_{00} - \frac{R}{2}. \quad (2.17)$$

So, the first order of the time-time component of Einstein’s field equations is

$$\delta G^0_0 = \frac{2}{a^2}\nabla^2\Phi - 6H(\dot{\Phi} - H\Psi) = 8\pi G \underbrace{\delta T^0_0}_{\delta\rho}. \quad (2.18)$$

This generalized expression for the Poisson equation can be written, in Fourier space and using the conformal time, as

$$k^2\Phi + 3\frac{a'}{a}\left(\Phi' - \frac{a'}{a}\Psi\right) = -4\pi G\delta\rho \quad (2.19)$$

or, in terms of the species,

$$k^2\Phi + 3\frac{a'}{a}\left(\Phi' - \frac{a'}{a}\Psi\right) = -4\pi G[\rho_{dm}\delta + \rho_b\delta_b + 4\rho_\gamma\Theta_0 + 4\rho_\nu\mathcal{N}_0]. \quad (2.20)$$

This is one of the equations that determine the evolution of Ψ and Φ , the other expression comes from the spatial part of Einstein’s field equations. First, the geometrical part,

$$G^i_j = g^{ik}\left[R_{kj} - \frac{g_{kj}}{2}R\right] = \frac{\delta^{ik}(1 - \Phi)}{a^2}R_{kj} - \frac{\delta_{ij}}{2}R. \quad (2.21)$$

to the first order in the perturbations, the anisotropic stress appears if $\Psi \neq -\Phi$:

$$\delta G^i_j = \frac{1}{a^2} k^i k_j (\Psi + \Phi). \quad (2.22)$$

Applying the projection operator, $\Pi_i^j = \hat{k}_i \hat{k}^j - \frac{1}{3} \delta_i^j$, in the spatial part of the Einstein tensor,

$$\Pi_i^j G^i_j = \frac{2}{3a^2} k^2 (\Psi + \Phi). \quad (2.23)$$

When projecting the energy-momentum tensor, one can see that it is proportional to the quadrupole, $\mathcal{L}_2(\mu)$, which means that only the photons and neutrinos's quadrupoles have influence. So, the last equation for the evolution of linear perturbations in the Universe is

$$k^2 (\Psi + \Phi) = -32\pi G a^2 [\rho_\gamma \Theta_2 + \rho_\nu \mathcal{N}_2], \quad (2.24)$$

meaning that, if photons and neutrinos's quadrupoles are negligible, both potentials are equal and opposite.

Because of the coupled momenta given by the infinite hierarchy of equations, these equations can be very hard to solve. Some approximations can be done in order to get useful results, but there are codes available, like **CAMB**¹ [29], that can quickly give exact solutions for these equations, in linear theory.

2.1.1 Newtonian Perturbation Theory

A simpler case can be derived to examine the growth of density perturbations for length scales smaller than the Hubble radius. For such cases, a Newtonian framework can be used considering that matter is dust-like (pressureless) with density $\rho(\mathbf{r}, t)$. Matter, then, can be described in a fluid approximation, with a velocity field $\mathbf{v}(\mathbf{x}, t)$. In this case, the equations of motion for fluids are

$$\left\{ \begin{array}{ll} \frac{D\rho}{Dt} = -\rho \nabla \cdot \mathbf{v} & \text{(Continuity Equation);} \\ \frac{D\mathbf{v}}{Dt} = -\frac{\nabla p}{\rho} - \nabla \Phi & \text{(Euler Equation);} \\ \nabla^2 \Phi = 4\pi G \rho & \text{(Poisson Equation);} \end{array} \right. \quad (2.25)$$

with $D/Dt \equiv \partial/\partial t + \mathbf{v} \cdot \nabla$ as the **convective derivative**. Considering a first order perturbation on the homogeneous background, $\rho(\mathbf{x}, t) \rightarrow \rho_0(t) + \delta\rho$ and $\mathbf{v}(\mathbf{x}, t) \rightarrow \mathbf{v}_0(t) + \delta\mathbf{v}$, where $\mathbf{v}_0 = H\mathbf{x}$ (\mathbf{x} is the physical coordinate) denotes the Hubble flow.

¹Available online at <http://camb.info/>

The continuity equation becomes

$$\left(\frac{\partial}{\partial t} + (\mathbf{v}_0 + \delta\mathbf{v}) \cdot \nabla \right) (\rho_0 + \delta\rho) = -(\rho_0 + \delta\rho) \nabla \cdot (\mathbf{v}_0 + \delta\mathbf{v}), \quad (2.26)$$

and the background solution is just $\dot{\rho} = -3H\rho_0$, allowing to rewrite (2.26) as

$$\left(\frac{\partial}{\partial t} + \mathbf{v}_0 \cdot \nabla \right) \delta\rho = -\rho_0 \nabla \cdot \delta\mathbf{v} - \delta\rho \nabla \cdot \mathbf{v}_0. \quad (2.27)$$

The expression inside the left hand side parenthesis in (2.27) can be identified as the time derivative for a observer comoving with the unperturbed expansion of the Universe, $d/dt \equiv \left(\frac{\partial}{\partial t} + \mathbf{v}_0 \cdot \nabla \right)$. Therefore, one can express (2.25) for the perturbations in terms of the density contrast, $\delta \equiv \delta\rho/\rho_0$, as

$$\left\{ \begin{array}{ll} \frac{d}{dt} \delta = -\nabla \cdot \delta\mathbf{v} & \text{(Continuity Equation);} \\ \frac{d}{dt} \delta\mathbf{v} = -\frac{\nabla \delta p}{\rho_0} - \nabla \delta\Phi - (\delta\mathbf{v} \cdot \nabla) \mathbf{v}_0 & \text{(Euler Equation);} \\ \nabla^2 \delta\Phi = 4\pi G \rho_0 \delta & \text{(Poisson Equation);} \end{array} \right. \quad (2.28)$$

It is more useful to consider this problem in comoving coordinates, instead of Eulerian, in order to account for the expansion of the Universe. Hence, $\mathbf{x} = a(t)\mathbf{r}(t)$, $\delta\mathbf{v} = a(t)\mathbf{u}(t)$, and $\nabla_x = a^{-1}\nabla_r$ (the subscript will be dropped for notation purposes). So, for a fundamental observer, both continuity and Euler equations can be written as

$$\dot{\delta} = -\nabla \cdot \mathbf{u}, \quad (2.29)$$

$$\dot{\mathbf{u}} + 2\frac{\dot{a}}{a}\mathbf{u} = \frac{1}{a^2} \nabla \delta\Phi - \frac{\nabla \delta p}{\rho_0}. \quad (2.30)$$

Now, there are three equations for four variables (δ , \mathbf{u} , $\delta\Phi$ and δp). The equation of state is the one missing to complete the set, from which:

$$c_s^2 \equiv \frac{\partial p}{\partial \rho}. \quad (2.31)$$

One can express the evolution for the amplitude of δ as

$$\ddot{\delta} + 2\frac{\dot{a}}{a}\dot{\delta} - \left(4\pi G \rho_0 - \frac{c_s^2}{a^2} \nabla^2 \right) \delta = 0. \quad (2.32)$$

This equation describes the evolution of the matter density contrast in the Newtonian

approximation.

2.1.2 Observational Probes of Inhomogeneity

The present Section briefly discuss some of the observational probes when investigating the consequences of linear perturbation theory on LSS. The combination of these observables leads to a deeper understanding of the cosmological parameters of the standard model.

Cosmic Microwave Background

Discovered by accident by two engineers from Bell Laboratories in 1964, the CMB is a snapshot from when the Universe was around 380,000 years old. When photons decoupled from baryonic matter, at redshift ~ 1100 , their last scattering surface stays imprinted throughout the Universe in all directions. The intensity for a gas of photon with a blackbody distribution is

$$I_\nu = \frac{4\pi\nu^3}{e^{2\pi\nu/T} - 1}. \quad (2.33)$$

In 1996, the FIRAS instrument, aboard the COBE space telescope, proved that a gas of photons with $T = 2.73K$ was in near-perfect agreement with the radiation measured from CMB – Figure 2.1 .

As suggested by linear perturbation theory (equations (2.10) to (2.16), (2.20), and (2.24)), anisotropies on the photon distribution are coupled to all the other components of the Universe, indicating that these primordial perturbations evolve into inhomogeneities.

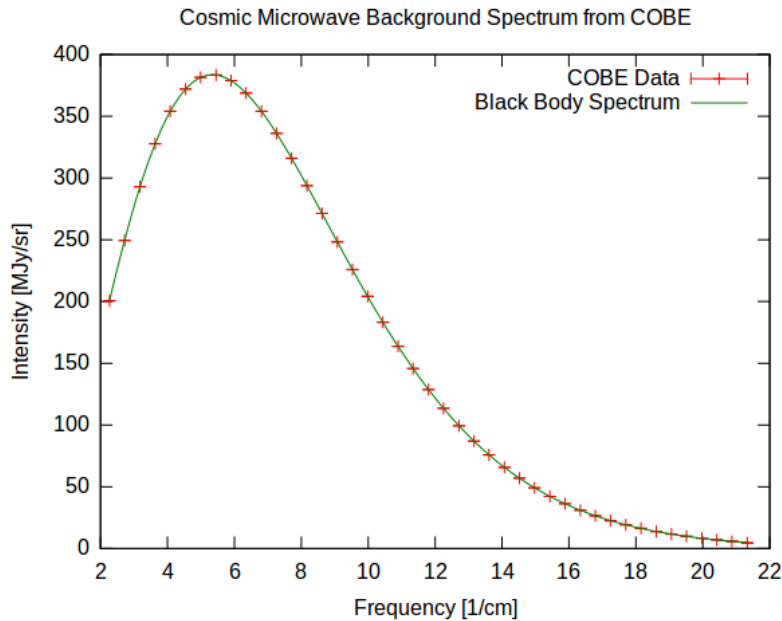


Figure 2.1: The blackbody spectrum for a 2.73K photon's gas in agreement with FIRAS's data points. [32]

Galaxy Surveys

The matter power spectrum (formally presented on Section 2.2) is one of the main results of galaxy catalogs – some of the main future surveys are specified in Section 1.3. Although the connection between galaxy positions and the three-dimensional power spectrum for dark matter is not direct – for only luminous matter can be observed –, galaxies work as biased tracers of the underlying density field. This means that the dark matter density contrast should be related to the tracer’s density field through a bias: [33].

$$\delta_g = b\delta_{DM} \quad (2.34)$$

Some problems might arise from this definition, since bias may vary with scale, and galaxy distances are measured in redshift space, combining the information on radial position with velocity. At small scales, for example, Redshift space distortions make a spherical structure, collapsing gravitationally, appear as a flattened ellipse, elongated in the radial direction.

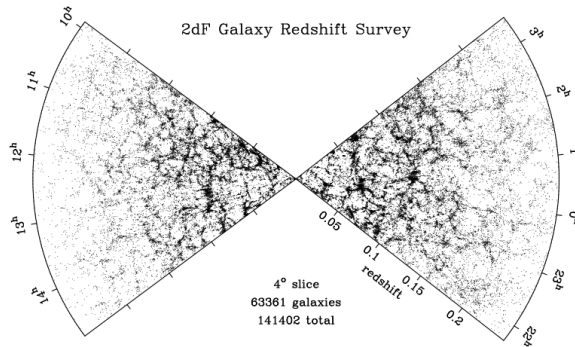


Figure 2.2: Distribution of 141,402 galaxies from the 2dF Redshift Galaxy Survey in a 4° wide range [34]. Galaxy catalogs like this one are the base for the power spectrum measurement.

Baryon Acoustic Oscillations

During the radiation epoch, photons and baryons were tightly coupled, which results in the photon-baryon plasma experiencing acoustic oscillations. Some acoustic peaks were first observed in the CMB angular power spectrum, suggesting that some large-scale consequences should also be observed in the distribution of matter. In fact, Eisenstein et al (2005) demonstrated the acoustic oscillations imprint in the correlation function using data from SDSS luminous red galaxies [11] (see Figure 2.4).

At redshift $z \sim 1100$, recombination suddenly decreases the sound speed ending the wave propagations due to cosmological perturbations in the relativistic plasma. During the epoch between the formation of primordial perturbations and recombination, the char-

acteristic time scale translated into a characteristic length scale producing oscillations, a harmonic series of maxima and minima in the anisotropy spectrum of the CMB [11]. Linear perturbation theory predicts that these acoustic oscillations in the primordial plasma would be imprinted at later times in the large-scale structures of non-relativistic matter [35].

In other words, the Universe was composed of a hot plasma of photons and baryons before recombination and decoupling. These two components were tightly coupled via Thompson scattering and the forces of gravitation and radiation pressure set up oscillations in the photon gas. Considering a spherical perturbation in the density of the baryon-photon plasma, it propagates outwards in form of a acoustic wave with sound speed $c_s = c/\sqrt{3(1+R)}$, where $R \equiv 3\rho_b/4\rho_\gamma \propto \Omega_b/(1+z)$ [36]. After recombination, the Universe becomes neutral and the baryon acoustic wave “freeze” while the photons propagate freely – forming what is observed by CMB [12]. The baryons distribution has an imprinted density excess, which is related to this characteristic spherical shell from when the baryon wave “stalled”. As baryons and dark matter interact through gravity, dark matter distribution also contains this acoustic peak. Figure 2.3 shows different stages of the BAO peak evolution.

Suppose a galaxy is formed at the centre of the initial density perturbation. The correlation function in Figure 2.3 shows a bump at a radius r' , which means a higher probability of finding another galaxy separated by a distance r' . This scale is close to the sound horizon – the comoving distance a sound wave can travel inside the baryon-photon plasma during decoupling – and it is related to the baryon and matter densities as:

$$r' = \int_{z_{rec}}^{\infty} \frac{c_s dz}{H(z)} = \frac{1}{\sqrt{\Omega_m H}} \frac{2c}{3z_{eq} R_{eq}} \ln \left(\frac{\sqrt{1+R_{rec}} + \sqrt{R_{rec} + R_{eq}}}{1 + \sqrt{R_{eq}}} \right), \quad (2.35)$$

where $z_{eq} = \Omega_m/\Omega_\gamma$ is the redshift of matter-radiation equality and R_{rec} refers to the recombination. As long as one can measure Ω_b with high precision, the scale r' works as a standard ruler [12].

According to Eisenstein (2005), the measurement of the BAO peak leads to several conclusions. Firstly, it provides a smoking-gun evidence that linear perturbation theory governs the formation of LSS from an initial state at redshift $z \sim 1100$. Also, it provides further evidence that dark matter was present at recombination epoch, since a pure baryonic model would be in disagreement with the observed correlation function peak. Finally, the BAO scale provides a natural length scale which can be measured over a wide range of redshifts, helping to probe the angular diameter distance and the evolution of the Hubble flow. However, the acoustic signal in matter correlations is weak, a 10% contrast in the matter power spectrum on large scales, meaning that for a survey to observe it well, it must have an effective volume of at least $\sim 1Gpc^3 h^{-3}$. Such volumes were not

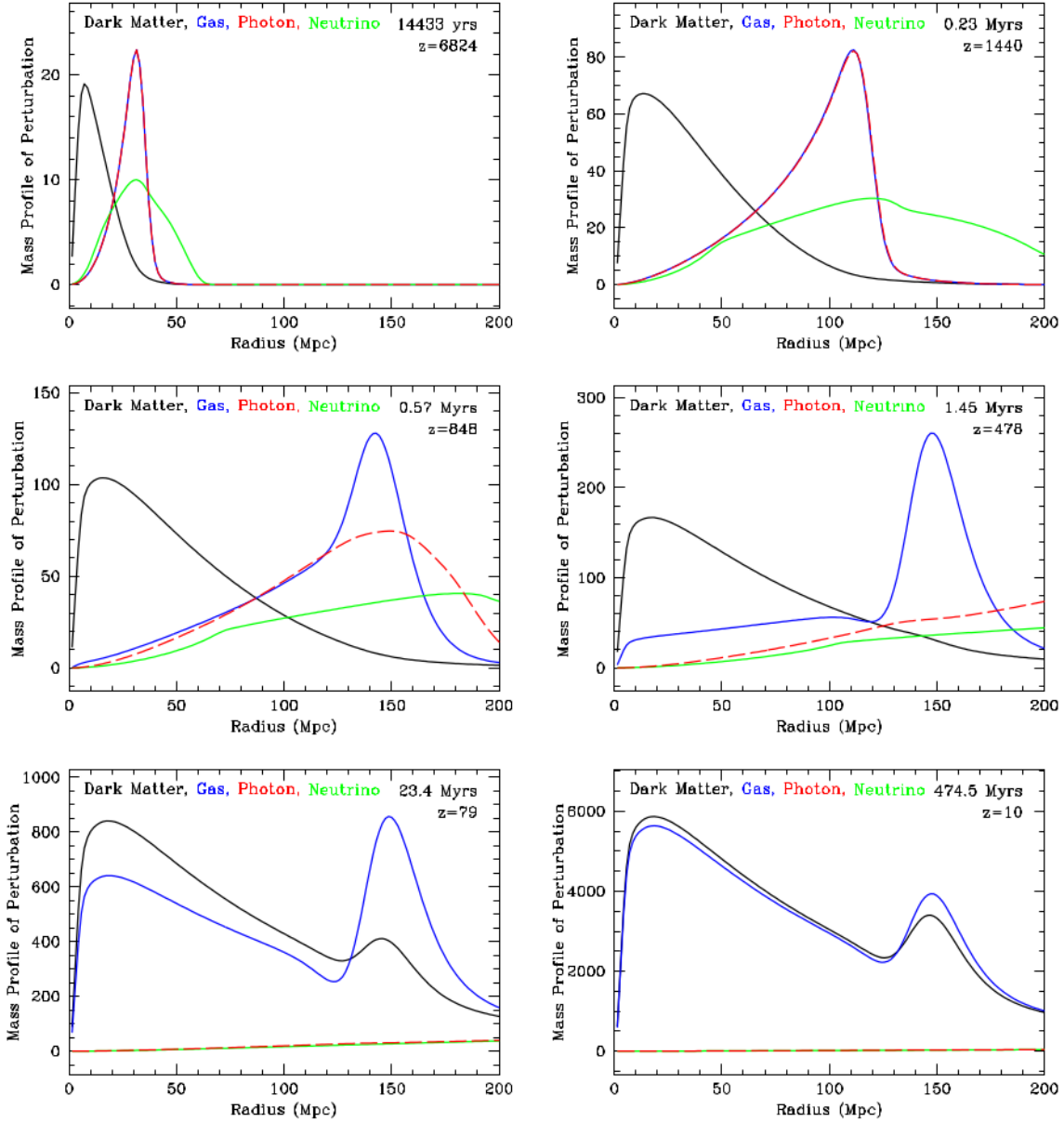


Figure 2.3: Different stages of the evolving spherical density perturbation according to Eisenstein *et al.* (2007). The density perturbation initially propagates through the baryon-photon plasma as a pulse (*top-left*). As dark matter only interacts gravitationally with this plasma, its perturbation takes more time to reach that of the tightly coupled plasma. However, during recombination epoch, photons continue to stream away from baryons (*middle-left*). After recombination (*middle-right*), photons freely stream away leaving a density perturbation in baryons around $105 Mpc h^{-1}$, together with a dark matter perturbation near the origin. The last panels show how the acoustic peak is affected due gravitational effects due dark matter and baryon interaction. Figure from [36].

easily achieved by the first generation of redshift galaxy surveys, although, the current generation is capable of using the BAO standard ruler for precise measurements of the Hubble flow.

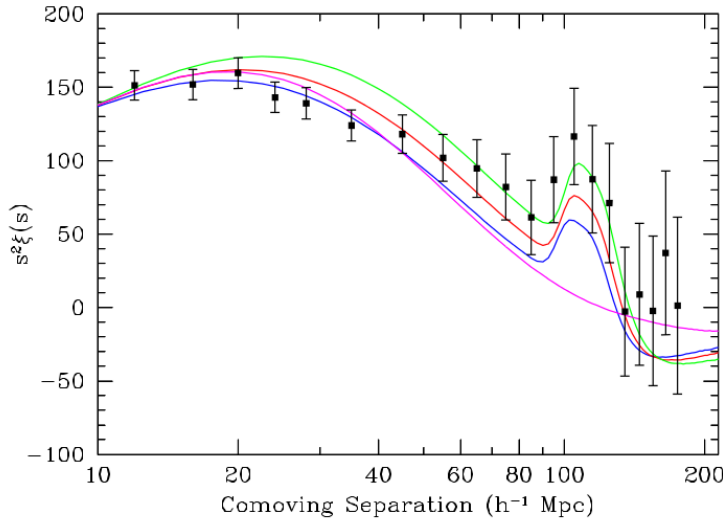


Figure 2.4: Correlation function times r^2 from SDSS's Luminous Red Galaxies and fits for different models. Models are $\Omega_m h^2 = 0.12$ (*green*), 0.13 (*red*), and 0.14 (*blue*); all with $\Omega_b h^2 = 0.024$. The magenta line corresponds to a pure CDM model with $\Omega_m h^2 = 0.105$ and lacks the acoustic peak. Figure from [11].

2.2 Statistical Analysis of the Large-Scale Structure

In the case for a flat comoving geometry, it is useful to develop a plane wave decomposition formalism in which the density field is represented as a superposition of many modes. Although this does not work for curved geometries, the plane waves provide a complete set of eigenfunctions for a flat FRW geometry. Considering that the density field has periodic boundary conditions within some box of size L_{box} , the Fourier expansion will be expressed as

$$\delta(\mathbf{r}) = \sum \delta_{\mathbf{k}} e^{-i\mathbf{k}\cdot\mathbf{r}}, \quad (2.36)$$

with $\mathbf{k} = \frac{2\pi}{L_{box}} \mathbf{n}$ and $n_x, n_y, n_z = 1, 2, 3, \dots$

Let the size of the box, L_{box} , become large enough so the sum at (2.36) turns into an integral of the density of modes in Fourier space – as it is usually done, *e.g.*, in statistical mechanics [16]:

$$\delta(r) = \left(\frac{L_{box}}{2\pi} \right)^3 \int d^3k \delta_{\mathbf{k}}(k) e^{-i\mathbf{k}\cdot\mathbf{r}} \quad (2.37)$$

$$\delta_{\mathbf{k}}(k) = \left(\frac{1}{L_{box}} \right)^3 \int d^3r \delta(r) e^{i\mathbf{k}\cdot\mathbf{r}}. \quad (2.38)$$

Notwithstanding, it is easier to work with the sum convention when using Fast Fourier Transforms algorithms, as it will be presented on Section 2.3.

2.2.1 Correlation Function and Power Spectrum

Firstly, the **correlation function** can be defined in terms of the density contrast as

$$\xi(\mathbf{r}) \equiv \langle \delta(\mathbf{r}')\delta(\mathbf{r}' + \mathbf{r}) \rangle. \quad (2.39)$$

Here, the $\langle \rangle$ expresses a normalized average over a certain volume $V = L_{box}^3$.

Together with (2.36) – and as $\delta(\mathbf{r})$ is real – one can express ξ as

$$\xi(\mathbf{r}) = \left\langle \sum_{\mathbf{k}} \sum_{\mathbf{k}'} \delta_{\mathbf{k}} \delta_{\mathbf{k}'}^* e^{-i(\mathbf{k}' - \mathbf{k}) \cdot \mathbf{r}'} e^{-i\mathbf{k} \cdot \mathbf{r}} \right\rangle. \quad (2.40)$$

with

$$\langle \delta_{\mathbf{k}} \delta_{\mathbf{k}'}^* \rangle = \begin{cases} \delta_{\mathbf{k}\mathbf{k}'} |\delta_{\mathbf{k}}|^2 & \text{(discrete);} \\ (2\pi)^3 |\delta_{\mathbf{k}}|^2 \delta_D^3(\mathbf{k} - \mathbf{k}') & \text{(continuum);} \end{cases} \quad (2.41)$$

The remaining sum can be taken to the continuum limit:

$$\xi(\mathbf{r}) = \frac{V}{(2\pi)^3} \int d^3k |\delta_{\mathbf{k}}|^2 e^{-i\mathbf{k} \cdot \mathbf{r}} \quad (2.42)$$

The **power spectrum** is defined as the Fourier pair of the correlation function, yet one can simply express it as

$$P(k) \equiv \langle |\delta_{\mathbf{k}}|^2 \rangle. \quad (2.43)$$

More generally, in terms of the mean galaxy density, \bar{n} , the galaxy density contrast is $\delta_g(\mathbf{r}) = (n(\mathbf{r}) - \bar{n})/\bar{n}$ and the power spectrum can be defined in terms of the Fourier transform of the galaxy density contrast, $\delta_{\mathbf{k}}(\mathbf{k})$

$$\langle \delta_{\mathbf{k}}(\mathbf{k}) \delta_{\mathbf{k}'}(\mathbf{k}') \rangle = (2\pi)^3 P(k) \delta_D^3(\mathbf{k} - \mathbf{k}'). \quad (2.44)$$

This means that the power spectrum is the second moment of the distribution in Fourier space, the variance. If the Universe is very smooth, the power spectrum will have a small amplitude, whereas if it has considerable inhomogeneities, the power spectrum will be larger. From (2.44), one can see that the power spectrum has dimensions of $(length)^3$.

As the Universe is isotropic, the density contrast does not have a preferred direction. This means that there is no angular dependence in the power spectrum, $\langle |\delta_{\mathbf{k}}(\mathbf{k})|^2 \rangle = |\delta_{\mathbf{k}}(k)|^2$. The angular dependence in (2.42) can be integrated in spherical coordinates if the polar axis is along the \mathbf{k} direction – $\exp\{-i\mathbf{k} \cdot \mathbf{r}\} \rightarrow \cos(kr\mu)$ –, so (2.42) can be written as

$$\xi(r) = \frac{4\pi V}{(2\pi)^3} \int dk k^2 P(k) \frac{\sin(kr)}{kr} \quad (2.45)$$

The **Code for Anisotropies in the Microwave Background** [29], or just **CAMB**, can evolve the inhomogeneities equations from 2.1 and provide a theoretical matter power spectrum given a certain cosmology (see Figure 2.5).

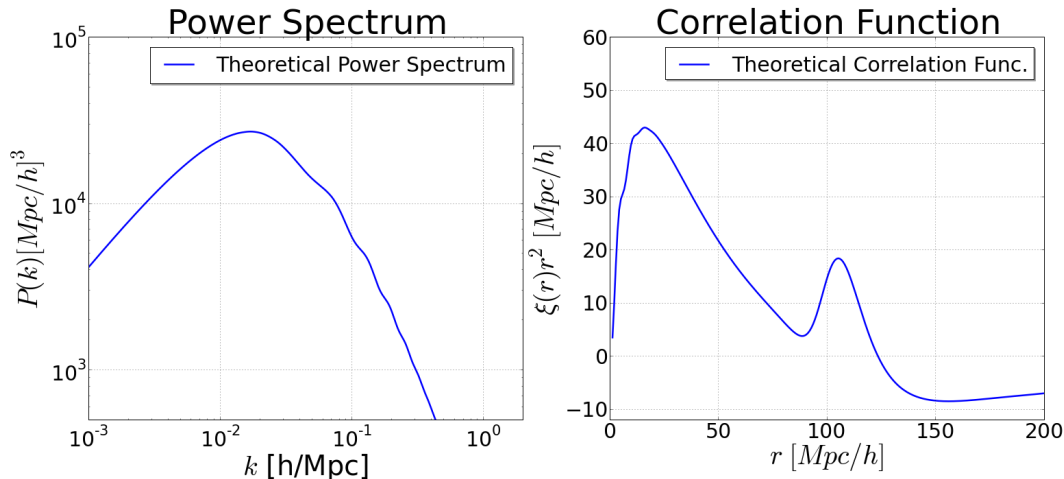


Figure 2.5: (left) A theoretical matter power spectrum for the Λ CDM model generated with **CAMB**. (right) The correlation function obtain from **CAMB**'s theoretical matter power spectrum using (2.45). The second peak, at $\sim 105 Mpc h^{-1}$, is the BAO scale.

2.3 Gaussian and Log-Normal Density Fields

Linear perturbation theory – developed on Section 2.1 – is an important tool to make predictions about LSS. In the present Section, the main goal is to develop a formalism capable of generating galaxy mock catalogs in order to compare real data with predictions made from linear perturbation. To do so, one must first understand the statistical properties of the underlying matter distribution, δ . As the density (contrast) field is approximately homogeneous in very large scales [16]. One can consider the concept of **ensembles of Universes**, which means that the density has different values in space, but with a given variance which is the same everywhere. To obtain large scale homogeneities, the **variance**, $\langle \delta^2 \rangle$, must be position-independent, measured looking at different and separate regions of the Universe. This is a version of the ergodic hypothesis[20].

It is nonsense to seek for a particular solution to the linear perturbation equations – or even non-linear – that produces the **real** distribution of galaxies, *i. e.*, reproduces the actual position of every observed galaxy in the Universe. Strictly speaking, it is not expected from the theory to predict the density contrast at any specific location \mathbf{r} . To do so would require knowledge of the actual initial conditions, $\delta(\mathbf{r}, t_i)$, an information that is

not available. Instead, one should look for a more general description, trying to reproduce the average statistical properties of the underlying matter distribution.

2.3.1 Statistical Properties of a Gaussian Density Field

First, consider the Universe as a limited box – one can think about it as a limited 3D sky survey map – which can be divided into equal sized cells with the same statistical properties and $\delta_1, \delta_2, \delta_3, \dots, \delta_N$ as the dimensionless density contrast on each cell (a cube with side L_{cell} and volume dV). This can be interpreted as a realization of a single random variable δ . Once determined the probability of any δ realization, all the statistical properties can be inferred. So, a probability density function (p.d.f.) might describe the density contrast which will be a functional of δ , $\mathbb{P}[\delta]$. It follows from the definition of δ , (2.1), that it should have zero mean.

The probability is given as a function of a set of variables $(\delta_1, \delta_2, \delta_3, \dots, \delta_N)$ by a p.d.f. $\mathbb{P} = \mathbb{P}[\delta_1, \delta_2, \dots, \delta_N]$ that would be efficiently expressed as

$$\mathbb{P}[\delta_1, \delta_2, \dots, \delta_N] = \prod_{i=1}^N f_i(\delta_i) \quad (2.46)$$

However, this decomposition implies that each of the δ_i evolves independently of the others, which is not true as gravity and other interactions imply that the $\delta_i(\mathbf{r})$ are correlated. Instead, from Eq. (2.41), one can work in Fourier space as each of the $\mathbf{k} = (2\pi/L)\mathbf{n}$ – assuming **harmonic boundary conditions** – evolves independently:

$$\mathbb{P}[\delta(\mathbf{k})] = \prod_{\mathbf{k}} g_{\mathbf{k}}(\delta_{\mathbf{k}}), \quad (2.47)$$

and

$$\delta_{\mathbf{k}} = \int_V d^3r \delta(\mathbf{r}) e^{-\mathbf{k}\cdot\mathbf{r}}. \quad (2.48)$$

A simple choice for $g_{\mathbf{k}}$ is a Gaussian, as suggested by the theory of inflation [15, 20, 16] From (2.48) one can see that $\delta_{\mathbf{k}}$ comes from combining $\delta(\mathbf{r})$ from various different positions. It is reasonable to assume that $\delta(\mathbf{r})$ was almost uncorrelated – or almost uncorrelated – in the very early Universe. As $\delta_{\mathbf{k}}$ is an integral over a large number of nearly uncorrelated random variables, from the central limit theorem, one can assume that the p.d.f. for $\delta_{\mathbf{k}}$ is nearly Gaussian. It is important to recall that, since $\delta(\mathbf{r})$ is real, $\delta_{\mathbf{k}}$ is constrained by $\delta_{-\mathbf{k}} = \delta_{\mathbf{k}}^*$.

Now, expressing $\delta_{\mathbf{k}} = A_{\mathbf{k}} e^{i\phi_{\mathbf{k}}}$, the Gaussian p.d.f. for $\delta_{\mathbf{k}}$ can be expressed as

$$g_{\mathbf{k}}(A_{\mathbf{k}}, \phi_{\mathbf{k}}) dA_{\mathbf{k}} d\phi_{\mathbf{k}} = \frac{1}{(2\pi)^{3/2} \sigma_{\mathbf{k}}} \exp \left[-\frac{A_{\mathbf{k}}^2}{2\sigma_{\mathbf{k}}^2} \right] dA_{\mathbf{k}} d\phi_{\mathbf{k}} \quad (2.49)$$

where $\langle A_{\mathbf{k}}^2 \rangle = \sigma_{\mathbf{k}}^2$ and $\phi_{\mathbf{k}}$ is a regular distribution in the range $(0, 2\pi)$. Which means $\delta_{\mathbf{k}}$ have random phases and Gaussian amplitudes. The first moment of (2.49) is $\langle \delta_{\mathbf{k}} \rangle = 0$ – as expected for the density field. However, recalling the result from (2.43), the variance of the Gaussian amplitude p.d.f. is the matter power spectrum of fluctuations,

$$\sigma_{\mathbf{k}}^2 = P(k). \quad (2.50)$$

This is the first step towards a “recipe” used to generate a galaxy mock catalog from a theoretical matter power spectrum. First, one uses a given set of cosmological parameters to evolve the linear equations for background perturbations and obtain a theoretical matter power spectrum. Using this $P(k)$ as the variance of Gaussian realizations, (2.49), one can produce a density fluctuation field in Fourier space – since in this case, each mode evolves independently.

The next step is to transform from Fourier space to real space. To do it so, consider that the probability of having a specific configuration of $\{\delta_{\mathbf{k}}\}$ is given by multiplying the independent probabilities for each $\delta_{\mathbf{k}}$,

$$\mathbb{P}[\{\delta_{\mathbf{k}}\}] = \prod_{\mathbf{k}} g_{\mathbf{k}}(\delta_{\mathbf{k}}) = N \exp \left\{ -\frac{1}{2} \sum_{\mathbf{k}} \frac{|\delta_{\mathbf{k}}|^2}{P(k)} \right\}. \quad (2.51)$$

Now, using the Fourier Transform to go from \mathbf{k} -space to \mathbf{r} -space,

$$|\delta_{\mathbf{k}}|^2 = \int d^3 r \int d^3 r' \delta(\mathbf{r}) \delta(\mathbf{r}') e^{-i\mathbf{k} \cdot (\mathbf{r} - \mathbf{r}')} \quad (2.52)$$

and, together with (2.51), one can write

$$\begin{aligned} \mathbb{P}[\delta(\mathbf{r})] &= N \exp \left\{ -\frac{1}{2} \sum_{\mathbf{k}} \int d^3 r \int d^3 r' \delta(\mathbf{r}) \delta(\mathbf{r}') e^{-i\mathbf{k} \cdot (\mathbf{r} - \mathbf{r}')} \frac{1}{P(k)} \right\} \\ &= N \exp \left\{ -\frac{1}{2} \int d^3 r \int d^3 r' \delta(\mathbf{r}) \delta(\mathbf{r}') \mathfrak{F}(\mathbf{r} - \mathbf{r}') \right\}. \end{aligned} \quad (2.53)$$

Here, taking the continuum limit of the Fourier series, $\sum_{\mathbf{k}} \rightarrow (V/(2\pi)^3) \int d^3 k$,

$$\mathfrak{F}(\mathbf{r} - \mathbf{r}') = \sum_{\mathbf{k}} \frac{e^{i\mathbf{k} \cdot (\mathbf{r} - \mathbf{r}')}}{P(k)} \rightarrow \frac{V}{(2\pi)^3} \int d^3 k \frac{e^{-i\mathbf{k} \cdot (\mathbf{r} - \mathbf{r}')}}{P(k)} \quad (2.54)$$

This p.d.f. shows that, at different regions in the Universe, $\delta(\mathbf{r})$ is **not independent** and can not be expressed as a product of probability distribution functions. Nevertheless, the density contrast – in real space – can be obtained by

$$\delta(\mathbf{r}) = \frac{1}{V} \sum_{\mathbf{k}} \delta_{\mathbf{k}} e^{i\mathbf{k} \cdot \mathbf{r}}. \quad (2.55)$$

When applying this formalism in simulations, it is useful to express the Fourier transform (2.55) in terms of a Fast Fourier Transform (FFT). In one dimension, the discrete Fourier transform becomes

$$\delta(r) \rightarrow \delta_l = \delta(r_l) = \frac{\Delta k}{2\pi} \sum_j \exp\{i[\Delta k(j-1)\Delta r(l-1)]/n\} \underbrace{\delta(k_j)}_{\tilde{\delta}_j} \quad (2.56)$$

or

$$\delta_l = \frac{\Delta k}{2\pi} \sum_j \exp\{i[2\pi(j-1)(l-1)]/n\} \tilde{\delta}_j, \quad (2.57)$$

and the inverse FFT is:

$$\tilde{\delta}_j = \Delta r \sum_l \exp\{-i[2\pi(l-1)(j-1)]/n\} \delta_l, \quad (2.58)$$

where $\Delta r = V/n_{tot}$ and $\Delta k = 1/V$ with n the number of cells in one direction and n_{tot} the total number of cells. Using these tools, it is possible to generate Gaussian realizations of the density field. Unfortunately, this recipe leads to non-physical values for the density contrast. From the definition of $\delta(\mathbf{r})$, (2.1), one can see that any $\delta(\mathbf{r}) < -1$ results in $\rho(\mathbf{r}) < 0$ – which is not physical. As the Gaussian p.d.f. goes from $-\infty$ to $+\infty$, it is not impossible to generate values of $\delta_{\mathbf{k}}$ that lead to non-physical density contrasts.

2.3.2 From Gaussian to Log-Normal Density Fields

To solve the problem presented at the end of the last Section, Coles and Jones (1991) proposed a log-normal (LN) model for the mass distribution [37]. They argued that, different from regular linear theory, a LN model always has $\rho(\mathbf{r}) > 0$ and is close enough to the Gaussian model at early times, not contradicting the inflation predictions. As stated before, a Gaussian field with standard deviation σ has a non-null probability to produce non-physical $\delta(\mathbf{r})$. Even if the linear power spectrum corresponds to $\delta(\mathbf{r}) \ll 1$, or most cosmological scales of interest, the problem remains. When $\sigma(\delta(\mathbf{r})) \approx 1$, it is clear that the Gaussian approximation is not valid.

Since a LN density field should preserve $\langle \delta_{LN} \rangle = 0$, it can be defined as [37]

$$1 + \delta_{LN}(\mathbf{r}) = e^{\delta_G(\mathbf{r}) - \sigma_G^2(\mathbf{r})/2}, \quad (2.59)$$

where the subscript G refers to the Gaussian density field. This is a reasonable approximation for the real underlying matter density field since it is straightforward that it does not lead to $\rho(\mathbf{r}) < 0$. Also, where $\sigma_G(\mathbf{r}) \ll 1$, the LN density field behaves as the Gaussian. For the first moment,

$$\begin{aligned}\langle \delta_{LN}(\mathbf{r}) \rangle &= \left\langle e^{\delta_G(\mathbf{r}) - \sigma_G^2(\mathbf{r})/2} \right\rangle - 1 \\ &= e^{-\sigma_G(\mathbf{r})/2} \langle e^{\delta_G(\mathbf{r})} \rangle - 1\end{aligned}\quad (2.60)$$

As shown in appendix A, using equation (A.5), one can see that $\langle e^{\delta_G(\mathbf{r})} \rangle = e^{\sigma_G(\mathbf{r})/2}$, as $\delta_G(\mathbf{r})$ comes from a Gaussian distribution with mean value $\mu = 0$. So,

$$\langle \delta_{LN}(\mathbf{r}) \rangle = e^{-\sigma_G^2(\mathbf{r})} (e^{\sigma_G^2(\mathbf{r})}) - 1 = 0 \quad (2.61)$$

As for the second moment of the log-normal density field,

$$\begin{aligned}\langle \delta_{LN}^2(\mathbf{r}) \rangle &= \langle (e^{\delta_G(\mathbf{r}) - \sigma_G^2(\mathbf{r})/2})^2 \rangle \\ &= e^{\sigma_G^2(\mathbf{r})} \langle e^{2\delta_G(\mathbf{r})} \rangle + 1 - 2e^{\sigma_G^2(\mathbf{r})/2} \langle e^{\delta_G(\mathbf{r})} \rangle\end{aligned}\quad (2.62)$$

for the first expression in $\langle \rangle$, one uses the second moment of the LN distribution, (A.8), leading to $\langle e^{2\delta_G(\mathbf{r})} \rangle = e^{2\sigma_G^2(\mathbf{r})}$; as for the last one, it goes like the one for the first moment, as stated before. Therefore,

$$\langle \delta_{LN}^2(\mathbf{r}) \rangle = e^{\sigma_G^2(\mathbf{r})} - 1 \simeq \sigma_G^2(\mathbf{r}) + \mathcal{O}(\sigma_G^4(\mathbf{r})). \quad (2.63)$$

This shows that the log-normal density field is a reasonable assumption for a physical density field with almost Gaussian statistics.

Another important feature arises when simulating the density field: one can easily introduce bias in (2.59).

$$1 + \delta_{LN}(\mathbf{r}) = e^{b\delta_G(\mathbf{r}) - b^2\sigma_G^2(\mathbf{r})/2} \quad (2.64)$$

which will reflect directly when going from the matter density field to a galaxy field, as presented in next subsection. It is also important to consider the correlation function, which for the log-normal field can be written as:

$$\xi_{LN}(r) = \langle \delta_{LN}(r) \delta_{LN}(r+r') \rangle = e^{\xi_G(r)} - 1. \quad (2.65)$$

Hence, in order to generate the LN density field with the right statistical properties, it is necessary to “prepare” the Gaussian density field. Instead of simply using a theoretical matter power spectrum as the variance of the Gaussian amplitude in 2.49, it is necessary to “gaussianize” it first. To do it, one must use (2.45) to go from power spectrum to correlation function and then, using (2.65) to write

$$\xi_G(r) = \ln[1 + \xi(r)]. \quad (2.66)$$

The ‘‘Gaussian’’ power spectrum is then defined as

$$P_G(k) = 4\pi \int dr r^2 \xi_G(r) \frac{\sin(kr)}{kr}. \quad (2.67)$$

This Gaussian power spectrum is the one used as the variance in (2.49) to generate the set of $\delta_G(\mathbf{k})$. The Fourier transform of this quantity, $\delta_G(\mathbf{r})$, and its variance, $\sigma_G(\mathbf{r})$, are the ones used in (2.64) to obtain the LN density contrast field. Figure 2.6 shows the difference between the Gaussian and the physical power spectrum.

This technique allows to reproduce a density contrast field that respects the physical conditions imposed by (2.1) and, in addition, it can incorporate **bias**. Next, one must transform from a $\delta_{LN}(\mathbf{r})$ to a $\delta_g(\mathbf{r})$, a galaxy density contrast – or, a galaxy mock catalog.

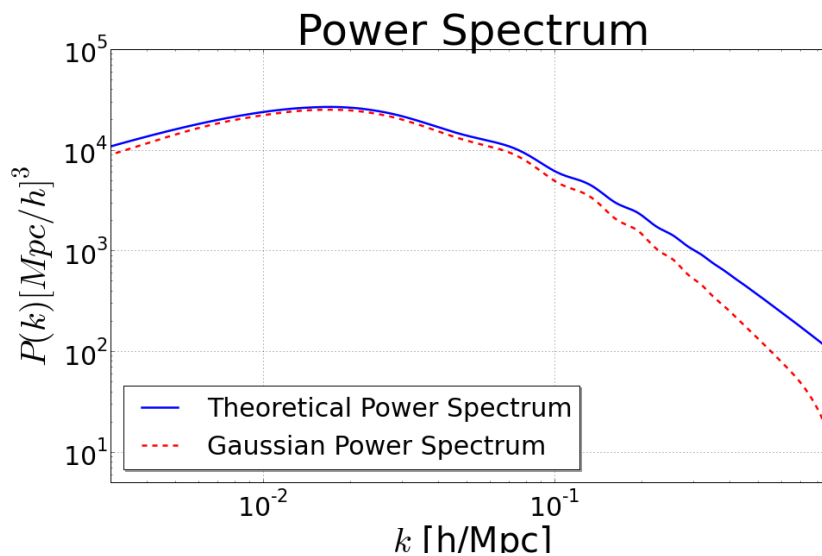


Figure 2.6: Comparison between the physical (theoretical) matter power spectrum and the Gaussian matter power spectrum used to generate log-normal density field realizations. Notice that the Gaussian spectrum loses power on small-scales.

2.3.3 From Poissonian Realizations to Galaxy Mock Catalogs

Since the log-normal field is realistic – in the sense that it respects $\delta(\mathbf{r}) > -1$ –, using Poissonian realizations, one can generate a catalog of objects, or galaxies. The Poisson p.d.f. contains two main features that are very fitting for this purpose: i) it always returns an integer value; ii) its mean value is equal to its variance.

$$\mathbb{P}(X = k) = \frac{\lambda^k e^{-\lambda}}{k!} \quad (2.68)$$

where λ is a distribution parameter, the mean value.

Now, a biased galaxy mock catalog can be produced using Poissonian realizations with $\lambda = \bar{n}(\mathbf{r})[1 + \delta_{LN}(\mathbf{r})]V$, where $\bar{n}(\mathbf{r})$ is the mean number of galaxies in a given region \mathbf{r} –

also known as the **selection function**.

$$N_g(\mathbf{r}) = \mathbb{P}_{\text{pois}}[\bar{n}(\mathbf{r})[1 + \delta_{LN}(\mathbf{r})]] \quad (2.69)$$

It follows from (2.69) that $\langle N_g(\mathbf{r}) \rangle = \bar{N}_g(\mathbf{r})$ and $\langle N_g^2(\mathbf{r}) \rangle = \bar{N}_g(\mathbf{r})[\bar{N}_g + 1]$. Therefore, the galaxy density contrast is defined as

$$\delta_g(r) = \frac{N_g(\mathbf{r}) - \bar{N}_g}{\bar{N}_g} \quad (2.70)$$

and the galaxy correlation function,

$$\begin{aligned} \xi_{gg}(\mathbf{r}) &= \langle \delta_g(\mathbf{r})\delta_g(\mathbf{r} + \mathbf{r}') \rangle \\ &= b^2\xi(\mathbf{r}) + \frac{1}{\bar{n}(\mathbf{r})}\delta_D^3(\mathbf{r} - \mathbf{r}'). \end{aligned} \quad (2.71)$$

The last term in the equation above is the **Poissonian shot-noise**, while the b^2 is the galaxy **bias**. A $b \neq 1$ means that luminous matter do not follow the same distribution as the total mass. In terms of the galaxy power spectrum,

$$P_{gg}(k) = b^2 P_0(k) \quad (2.72)$$

with $P_0(k)$ representing the underlying dark matter power spectrum, which one does not have direct access through observations.

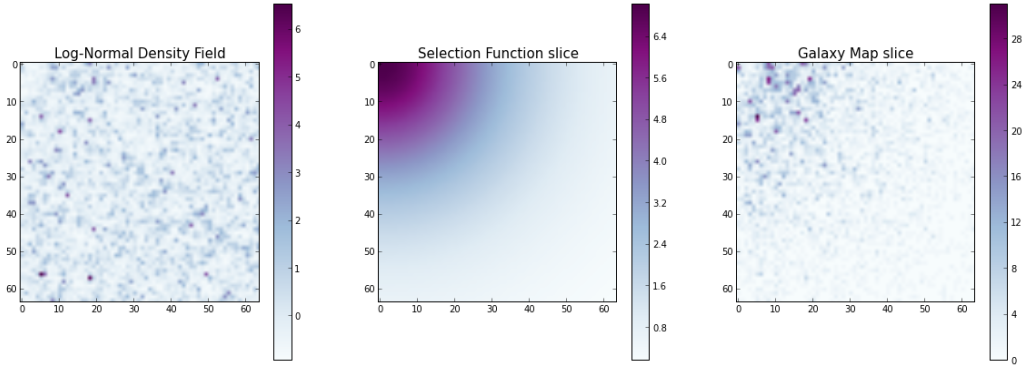


Figure 2.7: (*left*) An example of a log-normal density field. (*center*) A radial decaying selection function. (*right*) The resulting galaxy mock catalog after convolving the selection function with the log-normal density field through a Poissonian realization, Eq. (2.69)

It is important to highlight that some sources of uncertainties arise due to the realizations. Large scale fluctuations are associated with the Gaussian realizations from Eq.

(2.49), and are related to **cosmic variance** – the fact that any survey is volume limited, introducing statistical errors since one can not analyse all modes. The small-scale fluctuations, related to the Poissonian realizations, are due to the introduction of shot-noise from this type of statistics.

2.4 Power Spectrum Analysis: The FKP Estimator

Feldman, Kaiser and Peacock (1994) presented an optimal power spectrum estimator (FKP estimator) for three-dimensional surveys using a weighting scheme, under the assumption that long-wavelength Fourier modes come from a Gaussian distribution [30] – as it is also discussed in Section 2.3. Given the Poissonian realization formalism developed on last Section, it can be interpreted as

$$\mathbb{P}_{\text{pois}}[\text{Volume element } \delta V \text{ contains a galaxy}] = \bar{n}(\mathbf{r})[1 + \delta_{LN}(\mathbf{r})]\delta V \quad (2.73)$$

The FKP approach consists to take the Fourier transform of the real galaxy map minus a synthetic catalog with the same selection function. This procedure should take away fluctuations that are not due to the actual structure of the original map. The weighting function is adjusted to optimize the estimator's performance,

$$F(\mathbf{r}) \equiv \frac{1}{N}w(\mathbf{r})[N_g(\mathbf{r}) - \alpha N_{syn}(\mathbf{r})] \quad (2.74)$$

where $N_g(\mathbf{r}) = \sum_j \delta_D^3(\mathbf{r} - \mathbf{r}_j)$ and \mathbf{r}_j is the location of the j th galaxy – the same holds for the synthetic catalog, $N_{syn}(\mathbf{r})$. Also, α is a constant that matches the two catalogs, $\bar{n}_g = \alpha \bar{n}_{syn}$, and N is a normalization constant defined by

$$N = \left\{ \int d^3r \bar{n}^2(\mathbf{r})w^2(\mathbf{r}) \right\}^{1/2}. \quad (2.75)$$

The expectation value of the square module of the Fourier transformed (2.74) gives

$$\langle |F(\mathbf{k})|^2 \rangle = \frac{\int d^3r \int d^3r' w(\mathbf{r})w(\mathbf{r}') \langle [N_g(\mathbf{r}) - \alpha N_{syn}(\mathbf{r})][N_g(\mathbf{r}') - \alpha N_{syn}(\mathbf{r}')] \rangle e^{i\mathbf{k}(\mathbf{r}-\mathbf{r}')}}{\int d^3r \bar{n}^2(\mathbf{r})w^2(\mathbf{r})}. \quad (2.76)$$

As both catalogs are generated from Poissonian realizations, one can obtain the following relations

$$\begin{aligned} \langle N_g(\mathbf{r})N_g(\mathbf{r}') \rangle &= \bar{n}(\mathbf{r})\bar{n}(\mathbf{r}')[1 + \xi(\mathbf{r} - \mathbf{r}')] + \bar{n}\delta_D^3(\mathbf{r} - \mathbf{r}'); \\ \langle N_{syn}(\mathbf{r})N_{syn}(\mathbf{r}') \rangle &= \alpha^{-2}\bar{n}(\mathbf{r})\bar{n}(\mathbf{r}') + \alpha^{-1}\bar{n}(\mathbf{r})\delta_D^3(\mathbf{r} - \mathbf{r}'); \\ \langle N_g(\mathbf{r})N_{syn}(\mathbf{r}') \rangle &= \alpha^{-1}\bar{n}(\mathbf{r})\bar{n}(\mathbf{r}'); \end{aligned} \quad (2.77)$$

leading to

$$\langle |F(\mathbf{k})|^2 \rangle = \int \frac{d^3 k'}{(2\pi)^3} P(\mathbf{k}') W(\mathbf{k} - \mathbf{k}') + P_{shot}. \quad (2.78)$$

The last term on the expression above is the shot-noise term,

$$P_{shot} \equiv \frac{(1 + \alpha)}{N^2} \int d^3 r \bar{n}(\mathbf{r}) \frac{w^2(\mathbf{r})}{b^2(\mathbf{r})}. \quad (2.79)$$

As for the first term of (2.78), it is a three-dimensional convolution of the power spectrum with a window function, $W(\mathbf{k} - \mathbf{k}') = |G(\mathbf{k} - \mathbf{k}')|^2$, where $G(\mathbf{k})$ is the Fourier transform of the weighted selection function.

$$G(\mathbf{r}) \equiv \frac{w(\mathbf{r})\bar{n}(\mathbf{r})}{N} \quad (2.80)$$

In other words, from (2.78),

$$\hat{P}(\mathbf{k}) = |F(\mathbf{k})|^2 - P_{shot}. \quad (2.81)$$

So, averaging over \mathbf{k} -shells, the FKP estimator is just

$$\hat{P}(k) \equiv \frac{1}{V_k} \int_{V_k} d^3 k' \hat{P}(\mathbf{k}'), \quad (2.82)$$

where V_k is the \mathbf{k} -shell's volume.

Percival, Verde and Peacock (2004) also derived an expression for the optimal weighting in the FKP estimator [31]:

$$w(\mathbf{r}) = \frac{b^2 P(k)}{1 + \bar{n}(\mathbf{r}) b^2(\mathbf{r}) P(k)} \quad (2.83)$$

FKP Error Bars

To complete the power spectrum analysis, it is necessary to obtain error bars for the FKP estimator and understand the statistical fluctuations related to it. Firstly, one can assume that the window function is compact compared with the scales of interest, so the mean square fluctuations of the FKP estimator are:

$$\begin{aligned} \sigma_P^2(k) &\equiv \langle [\hat{P}(k) - P(k)]^2 \rangle \\ &= \frac{1}{V_k^2} \int_{V_k} d^3 k \int_{V_k} d^3 k' \langle \delta \hat{P}(\mathbf{k}) \delta \hat{P}(\mathbf{k}') \rangle \\ &\cong \frac{1}{V_k} \int d^3 k' \left| \frac{P(k)}{N^2} \int d^3 r [\bar{n}(\mathbf{r}) w(\mathbf{r})]^2 e^{i\mathbf{k}\cdot\mathbf{r}} + \frac{(1 + \alpha)}{N^2} \int d^3 r \bar{n}(\mathbf{r}) \frac{w^2(\mathbf{r})}{b^2(\mathbf{r})} e^{i\mathbf{k}\cdot\mathbf{r}} \right|^2. \end{aligned} \quad (2.84)$$

Finally, the fractional variance – leading to the error bars in Figure 2.8 – is given by

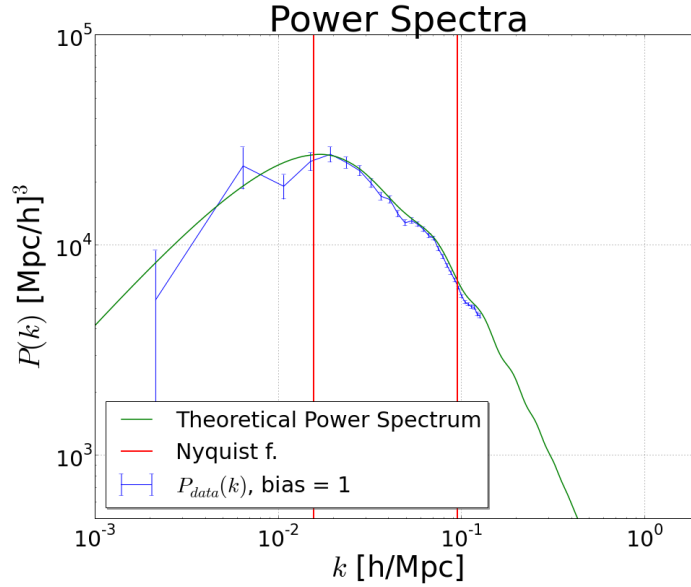


Figure 2.8: Power spectrum estimation for a cubic mock galaxy catalog with error bars given by (2.85) (blue) in comparison with the theoretical power spectrum from CAMB (green). The red lines are the limits of the survey’s volume, *i.e.*, all the modes which fit inside the characteristic scales of the survey: the cell size (which defines the highest Fourier mode – the Nyquist frequency) and the survey’s largest scale (which defines the smaller Fourier mode related to the survey).

$$\frac{\sigma_P^2(k)}{P^2(k)} = \frac{(2\pi)^3}{V_k N^4} \int d^3r \left\{ [\bar{n}(\mathbf{r})w(\mathbf{r})]^2 + \frac{1}{P(k)} \left[\bar{n}(\mathbf{r}) \frac{w^2(\mathbf{r})}{b^2(\mathbf{r})} \right] \right\}^2 \quad (2.85)$$

Figure 2.9 shows the comparison between the error bars due to the fluctuations of Gaussian and Poissonian realizations for mock catalog generation, and the ones from Eq. (2.85).

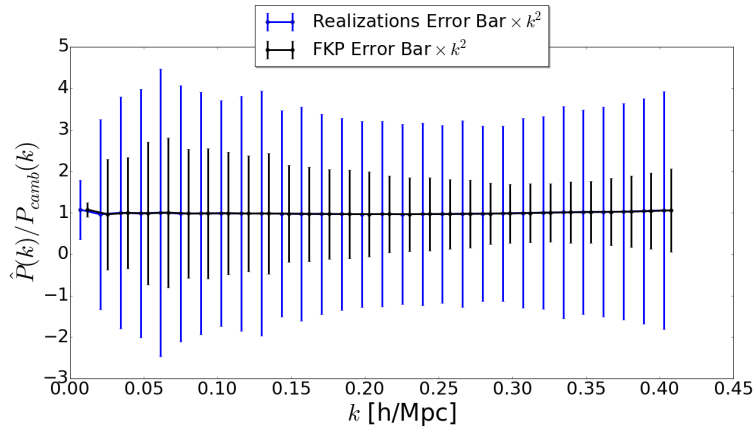


Figure 2.9: Comparison between FKP error bars and the fluctuations on the spectra due to the Gaussian and Poissonian realizations of the galaxy mocks using 300 realizations. Error bars were multiplied by k^2 for visualization purposes.

Chapter 3

Bayesian Statistics in Cosmology

Since the beginning of the precision cosmology era, data analysis is at the center of the discussions. Every year, cosmological experiments produce several hundred Terabytes of new data, and it has been proved that using simple “brute force” methods would take decades to analyse it, even with tomorrow’s technologies and fast parallelizable processing capacity. Considering Cosmology’s study object, it seems risky to use a frequentist approach – there is only one Universe to do statistics with. In other words, one can only observe characteristics in a region of the Universe and infer consequences. There is no possibility to do repetitive experiments in order to probe, for example, the density of dark matter.

The main goal of data analysis in cosmology is to probe the cosmological parameters from all different observables and to combine data to obtain the maximum amount of information. This way, one can associate data from different experiments in estimates for the set of the cosmological parameters. With the amount of high quality data coming up in the next few years, it is fundamental to investigate powerful statistical tools in order to constrain a large number of parameters. One needs an approach that allows to put estimates and error bars on quantitative parameters. This is where Bayesian statistics comes in. It allows to infer parameter estimations from single data sets, to determine degrees of plausibility to hypothesis (confidence levels), and to cross-correlate data, using different datasets to probe a model’s parameters – just to give some general example.

This chapter’s primary goal is to develop Bayesian inference as applied to Cosmology, in order to obtain measurements of cosmological parameters from observational data sets. The first Section reviews the basics of Bayesian statistics, from Bayes’s Theorem to parameter estimation. The second Section briefly discusses the applications of Bayesian inference in modern cosmology. Finally, this chapter’s final Section is dedicated to **Monte-Carlo Markov Chain** methods (MCMC), explaining the **affine invariant method** and the methodology employed for the analysis presented on Chapter 4.

3.1 Basic Bayesian Statistics

When asserting whether a hypothesis is right or wrong, one must assign a certain “degree of plausibility” to the proposition. It is reasonable to look for some criteria when defining degrees of plausibility [38], such as:

- i) They can be represented by real numbers

$$\text{prob}(\text{true}) = 1 \quad \text{and} \quad \text{prob}(\text{false}) = 0; \quad (3.1)$$

- ii) They obey “common sense”, *i.e.*, if the plausibility of A increases, then the plausibility of *not-A* (\bar{A}) should decrease

$$\text{prob}(A|I) = 1 - \text{prob}(\bar{A}|I); \quad (3.2)$$

- iii) The joint hypothesis of A **given** B is related in a sensible way to the plausibilities of A **and** B

$$\text{prob}(A, B|I) = \text{prob}(A|B, I) \times \text{prob}(B|I) \quad (3.3)$$

- iv) They obey consistency requirements, for example, the plausibility depends only on the evidence and not on the order in which it is considered;
- v) The degree of plausibility is transitive, which means that if A is more plausible than B , and B more than C , then A must necessarily be more plausible than C .

In terms of the regular parlance used in Bayesian statistics, the “degree of plausibility” is the **posterior probability**. Bayes’s theorem relates the posteriors to likelihoods and prior probabilities. Note that all expression above, (3.1), (3.2), and (3.3), conditionally depend on I . This denotes the relevant background information and means that there are no absolute probabilities – although the conditional on I can be omitted.

3.1.1 Bayes’s Theorem and Marginalization

The basis for any statistical theory comes from the **sum rule**, (3.2), and the **product rule**, (3.3). Any other result can be obtained from them, and Bayes’s theorem is not an exception. It follows directly from the product rule that

$$\text{prob}(B, A|I) = \text{prob}(B|A, I) \times \text{prob}(A|I). \quad (3.4)$$

However, $\text{prob}(B, A|I) = \text{prob}(A, B|I)$, so the right hand side of (3.4) can be expressed as $\text{prob}(A|B, I) \times \text{prob}(B|I)$, leading to Bayes's theorem:

$$\text{prob}(A|B, I) = \frac{\text{prob}(B|A, I) \times \text{prob}(A|I)}{\text{prob}(B|I)} \quad (3.5)$$

This relates $\text{prob}(A|B, I)$ to $\text{prob}(B|A, I)$. The importance of Bayes's theorem becomes more clear when one changes to data analysis terminology. Consider A as hypothesis and B as data [39], so (3.5) can be expressed as

$$\text{prob}(\text{hypothesis}|\text{data}, I) \propto \text{prob}(\text{data}|\text{hypothesis}, I) \times \text{prob}(\text{hypothesis}|I) \quad (3.6)$$

Bayesian statistics allows to relate the probability that a certain hypothesis is true, given the data, to the probability that the data would have been measured as it was if the hypothesis were actually true [the first term in (3.6), also known as **likelihood function**]. Another powerful feature of Bayesian statistics is the second term on (3.6) (the **prior probability**), which represents how much one knows (or do not) about the truth of the hypothesis before data is analysed. The combined probability of likelihood and prior leads to the posterior probability, the right hand side of (3.6). Note that the $\text{prob}(B|I) = \text{prob}(\text{data}|I)$ was omitted from (3.6). This term is called **evidence**, and turns out to be just a constant in most cases. However, in some cases, the evidence might be used for model selection [39].

Nuisance Parameters and Marginalization

When dealing with real data, sometimes it is necessary to take into account quantities which inevitably enter into the analysis, but are of no fundamental interest, called **nuisance parameters**. As an example, some unwanted background signal present in observations or any instrumental parameters that are hard to calibrate. For any of these cases, **marginalization** is an important tool to help dealing with nuisance parameters.

From the product rule (3.3), one can add the probability of *not-B* (\bar{B}) in both sides,

$$\text{prob}(A, B|I) + \text{prob}(A, \bar{B}|I) = [\text{prob}(B|A, I) + \text{prob}(\bar{B}|A, I)] \times \text{prob}(A|I). \quad (3.7)$$

However, the sum rule (3.2) guarantees that the expression inside brackets on the equation above should be equal to unity, so

$$\text{prob}(A|I) = \text{prob}(A, B|I) + \text{prob}(A, \bar{B}|I) \quad (3.8)$$

This equation has an important statement. It says that the probability of A being true, whether or not B is true, is equal to the sum of probabilities of A and B being true, together with A being true and B false. Now, suppose there's a set of statements related

to the proposition B , in a way that equation (3.8) can be rewritten as

$$prob(A|I) = \sum_k prob(A, B_k|I) \quad (3.9)$$

with $\sum_k prob(B_k|A, I) = 1$. The actual marginalization expression arises when taking the continuum limit of (3.9). In this context, B can be interpreted as the numerical value of a parameter of interest [39]. Then, the integrand of the posterior probability translates into a **probability density function** (p.d.f.).

$$pdf(A, B = b|I) = \lim_{\delta b \rightarrow 0} = \frac{prob(A, b \leq B \leq b + \delta b|I)}{\delta b} \quad (3.10)$$

so the probability that the value of B is inside some finite range $[b_1, b_2]$, given that A is true, can be expressed as

$$prob(A, b_1 \leq B \leq b_2|I) = \int_{b_1}^{b_2} pdf(A, B|I)dB. \quad (3.11)$$

Now, the definition of marginalization comes when one integrates (3.11) for all possible values of B , as the true value of B must be somewhere in between. This translates as

$$prob(A|I) = \int_{-\infty}^{+\infty} prob(A, B|I)dB \quad (3.12)$$

3.1.2 Parameter Estimation

It was shown that the posterior distribution contains information about the degree of plausibility of the value of a given parameter given a certain data set. Still, one may want to summarize this information using two values: the best estimate and a measure of its errors. As the probability density related to a single parameter's value is a mensuration of how much one can rely that the true value is near that point, it is straightforward that the best estimate is given by the maximum of the posterior p.d.f.

Let A be the parameter one wishes to estimate and $\mathbb{P} = prob(A|\{\text{data}\}, I)$ the posterior p.d.f. Then the best estimated value for A , a_0 , is given by the condition

$$\left. \frac{d\mathbb{P}}{dA} \right|_{a_0} = 0, \quad (3.13)$$

with the secondary condition that a_0 is a maximum value

$$\left. \frac{d^2\mathbb{P}}{dA^2} \right|_{a_0} < 0. \quad (3.14)$$

This method can be generalized to estimates of N parameters, $\{A_i\}$. The criteria for

best estimates given by (3.13) and (3.14) can be expressed, in terms of the logarithm of the likelihood, $\ln \mathbb{L} = \mathbb{K}$, for a set of optimal values, $\mathbf{a}_0 = \{a_{0i}\}$, as

$$\left. \frac{\partial \mathbb{K}}{\partial A_i} \right|_{\mathbf{a}_0} = 0, \quad (3.15)$$

where $i = 1, 2, 3, \dots, N$. Now, making a Taylor expansion of (3.15),

$$\mathbb{K} = \mathbb{K}(\mathbf{a}_0) + \frac{1}{2} \sum_{i=1}^N \sum_{j=1}^N \left. \frac{\partial^2 \mathbb{K}}{\partial A_i \partial A_j} \right|_{\mathbf{a}_0} (A_i - a_{0i})(A_j - a_{0j}) + \dots \quad (3.16)$$

One can think this situation in terms of vectors and matrices, $\mathbf{A} = \{A_i\}$, and – ignoring higher terms of the Taylor expansion in (3.16) – write the posterior p.d.f. as

$$\text{prob}(\mathbf{A}|\{\text{data}\}, I) \propto \exp \left[\frac{1}{2} (\mathbf{A} - \mathbf{a}_0)^T \nabla \nabla \mathbb{K}(\mathbf{a}_0) (\mathbf{A} - \mathbf{a}_0) \right]. \quad (3.17)$$

Here, $\nabla \nabla \mathbb{K}$ is an $N \times N$ matrix of second derivatives, and $(\mathbf{A} - \mathbf{a}_0)^T$ is the transpose of the $(\mathbf{A} - \mathbf{a}_0)$ vector. This p.d.f. is called a **multivariate Gaussian** and is a direct conclusion that $\nabla \mathbb{K}(\mathbf{a}_0) = 0$ gives the maximum for the posterior, leading to the best estimated value.

Nevertheless, from (3.17), comparing with a one-dimensional case, the variance is related to $\nabla \nabla \mathbb{K}|_{\mathbf{a}_0} \rightarrow -1/\sigma^2$. This result suggests that the covariance matrix σ^2 , from which the error can be estimated for each parameter, can be expressed as minus the inverse of $\nabla \nabla \mathbb{K}$ at the best value \mathbf{a}_0 :

$$\text{Cov}_{ij} = \sigma_{ij}^2 = \langle (A_i - a_{0i})(A_j - a_{0j}) \rangle = -(\nabla \nabla \mathbb{K})_{ij}^{-1}. \quad (3.18)$$

The parameters's error bars can be obtained from the square root of σ_{ij}^2 , the standard deviation, while the off-diagonal elements of (3.18) give information about the covariances between the estimated parameters A_i and A_j . It is important to highlight that the inverse of the diagonal elements of a matrix are not, generally speaking, equal to the diagonal elements of its inverse. Such mistakes can lead to wrong estimates for the error bars if one tries to avoid marginalization procedures [39].

In terms of the Fisher information matrix, it is related to Eq. (3.18):

$$F_{ij} = -(\nabla \nabla \mathbb{K})_{ij} = \text{Cov}_{ij}^{-1} \quad (3.19)$$

The Cramér-Rao inequality theorem states that $\text{Cov}_{ij} \geq F_{ij}^{-1}$ where the equality only holds when the estimated value truly lies at the maximum likelihood for a Gaussian likelihood.

3.2 Bayesian Inference for Galaxy Surveys

Bayesian statistics has many applications in cosmology and it was mainly developed, in this context, to obtain cosmological parameters from CMB measurements [40, 41, 42]. In many cases, the observable is not directly related to the parameters one wants to probe, for example, obtaining the age of the Universe from the CMB angular power spectrum [41]. This is no different when thinking about galaxy surveys. The main observable in this case is the three-dimensional distribution of galaxies, which is itself just a biased tracer of the underlying dark matter distribution.

Following the approach from last Section, when probing cosmological parameters from galaxy surveys, it is important to develop a likelihood function that takes into account our main observable, the galaxy power spectrum. This observable is sensitive to some cosmological parameters whose variations leads to different matter distributions. When constructing a likelihood function, one must compare predictions from perturbation theory with measurements from observations.

Section 2.4 was dedicated to the development of an optimal power spectrum estimator for galaxy distribution. This is obtained from redshift galaxy surveys to probe cosmological parameters. Based on what was developed in the last Section, a multivariate Gaussian on the estimated galaxy power spectrum seems a reasonable approach for a (log-)likelihood function. In this case,

$$\mathbb{K} = -\frac{1}{N_b} \sum_{i=1}^{N_b} \frac{[\hat{P}_d(k_i) - \hat{P}_{th}^{\mathbf{q}}(k_i)]^2}{2\sigma_d^2(k_i)} \quad (3.20)$$

where $\hat{P}_d(k_i)$ is the data galaxy power spectrum estimated using the FKP method and measured in N_b bins; $\sigma_d^2(k_i)$ is the data variance; and $\hat{P}_{th}^{\mathbf{q}}(k_i)$ is the theoretical galaxy power spectrum, generated with perturbation theory from a set of cosmological parameters \mathbf{q} that one wishes to estimate.

To obtain $\hat{P}_{th}^{\mathbf{q}}(k_i)$, one starts with a set of cosmological parameters $\mathbf{q} = \{H_0, \Omega_\Lambda, \Omega_m, \dots\}$, evolve the linear perturbation theory equations (Section 2.1) using **CAMB** [29], and obtain a theoretical matter power spectrum, $P_{th}^{\mathbf{q}}(k)$. With this theoretical matter power spectrum, one uses the procedures described in Section 2.3 to generate galaxy mock catalogs. This mock catalog contains the same cosmology, \mathbf{q} , “behind” its galaxy distribution and the **same selection function** used to estimate $\hat{P}_d(k_i)$ which means that, when estimating this mock’s power spectrum with an FKP estimator, the likelihood function will reflect only the dependence on the cosmological parameters \mathbf{q} .

It is fundamentally important to highlight the use of the same selection function (or selection function parameters when probing $\bar{n}(\mathbf{r})$ as well) on both power spectra in (3.20). As the FKP method uses a synthetic catalog to “remove” spurious structures, if one uses different $\bar{n}(\mathbf{r})$, some effects due to the convolution between spectrum and window function

[see Eq. (2.78)] can mimic different cosmologies and affect the parameters's estimations. The next chapter will present a detailed analysis of these assertions.

In terms of the posterior distribution, (3.20) can be expressed as

$$prob(\mathbf{q}|\{data\}, I) \propto \sum_{i=1}^{N_b} \exp \left\{ -\frac{[\hat{P}_d(k_i) - \hat{P}_{th}^{\mathbf{q}}(k_i)]^2}{2\sigma_d^2(k_i)} \right\} \times prob(\mathbf{q}|I). \quad (3.21)$$

The simplest choice is to take the priors, $prob(\mathbf{q}|I)$, as **flat**:

$$prob(\mathbf{q}|I) = \begin{cases} 1, & \text{if } (\mathbf{q}_{min} < \mathbf{q} < \mathbf{q}_{max}); \\ 0, & \text{otherwise;} \end{cases} \quad (3.22)$$

Extremes for each \mathbf{q} parameter vary depending on prior known information about each different cosmological parameter. For example, it is widely known that $50 < H_0 < 100$ km/s/Mpc, so these are suitable limits for a flat prior on the Hubble constant.

However, as was mentioned before, a “brute force” method to probe the posterior would take a huge amount of time and computational effort. The posterior presented in Eq. (3.21) has as many dimensions as the number of cosmological parameters, \mathbf{q} , or more, as shown in the next Chapter, when probing the effects of the selection function on the cosmological parameters. This turns the problem into an N-dimensional grid interpolation, making it very hard to find the likelihood's maximum value.

3.3 Monte-Carlo Methods for Bayesian Inference

Interpolating an N-dimensional likelihood function through a grid in parameter space is not a wise option when it comes to obtaining its maximum value and confidence levels. Monte-Carlo methods allow to quickly explore and sample unknown functions such as posterior distributions. Although there is no formal definition for what constitutes a Monte-Carlo method, the main algorithm applied in Cosmology is the Monte-Carlo Markov Chain (MCMC), which consists in performing random walks in parameter space, while sampling the posterior distribution. The present Section will introduce different computational algorithms for MCMC sampling, and discuss the advantages of each one.

MCMC methods generate M random samples of parameters sets $\{\Theta_i\}$ from the posterior p.d.f.

$$p(\Theta, \alpha|\{data\}, I) = \frac{1}{N} p(\{data\}|\Theta, \alpha, I) \times p(\Theta, \alpha|I) \quad (3.23)$$

where both the likelihood ($p(\{data\}|\Theta, \alpha, I)$) and the prior distribution ($p(\Theta, \alpha|I)$) can be easily computed for any value of (Θ, α) (α represents any nuisance parameters). In (3.23), N is a normalization constant equal to the evidence and, in most of the cases, there is no need to evaluate it.

One of the greatest advantages of MCMC is that, once the posterior is sampled, marginalized constraints on Θ are easily obtained by one- or two-dimensional histograms of projected samples into parameter subspaces spanned by Θ [43]. In other words, MCMC methods allow marginalizations to be treated as projections in subspaces, which implies that the expectation value of any function of the sampled parameters can be expressed as

$$\langle f(\Theta) \rangle = \int p(\Theta|\{\text{data}\}, I) f(\Theta) d\Theta \approx \frac{1}{M} \sum_{i=1}^M f(\Theta_i) \quad (3.24)$$

In most cases, generating samples for Θ is not a trivial task, but some analytical likelihood functions, such as a multivariate Gaussian, are an exception making this quite trivial. Over time, the random walks in parameter space produced by MCMC samplers draw a representative set of Θ from the posterior distribution. A feature of Markov Chain methods is that each point in parameter space depends solely on the position of the previous step.

The Metropolis-Hastings Algorithm

The Metropolis-Hastings algorithm (MH) is the most used MCMC method in literature, as it is very simple and fast to implement, although is not the fastest sampler there is [42, 43]. The chain goes from a position in parameter space Θ_1 to the next position Θ_2 with a transition probability $T(\Theta_1, \Theta_2)$, which is called the **transition kernel**, which is chosen so that the chain has a stationary asymptotic distribution equal to the posterior, $p(\Theta|\{\text{data}\}, I)$. By applying a **proposal density distribution**, $Q(\Theta_n, \Theta_{n+1})$, one can select a new point Θ_{n+1} given the current status of the chain in Θ_n . In MH, a new point in parameter space is accepted with probability

$$\gamma(\Theta_n, \Theta_{n+1}) = \min \left\{ 1, \frac{p(\Theta_{n+1}|\{\text{data}\}, I) Q(\Theta_{n+1}, \Theta_n)}{p(\Theta_n|\{\text{data}\}, I) Q(\Theta_n, \Theta_{n+1})} \right\} \quad (3.25)$$

with $T(\Theta_n, \Theta_{n+1}) = \gamma(\Theta_n, \Theta_{n+1}) Q(\Theta_n, \Theta_{n+1})$. This guarantees that $p(\Theta|\{\text{data}\}, I)$ is the equilibrium distribution for the Markov Chain [42, 43]:

$$p(\Theta_{n+1}|\{\text{data}\}, I) T(\Theta_{n+1}, \Theta_n) = p(\Theta_n|\{\text{data}\}, I) T(\Theta_n, \Theta_{n+1}) \quad (3.26)$$

As any MCMC method, the chain starts in some random position in parameter space and takes some time to reach the equilibrium point. This is called **burn in**. Although there is no formal definition of burn in, one can see it as the steps before the MCMC random walker's fluctuations reach an unbiased equilibrium value (Figure 3.1).

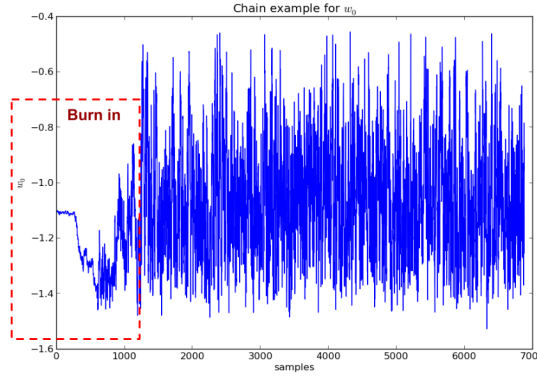


Figure 3.1: Illustration to show burn in for a w_0 chain generated by CosmoMC [42].

After burn in, every chain position is a correlated sample taken from the posterior distribution. When a point is not accepted $\Theta_{n+1} = \Theta_n$, the correlation is obvious. MH method converges for $n \rightarrow \infty$, but there are methods whose convergence times are shorter.

Algorithm 1 Procedure for a single step in Metropolis-Hastings algorithm.

- 1: Draw a proposed new point in parameter space from $Q(\theta, \Theta_n), \theta$.
 - 2: Define an acceptance probability $\gamma \leftarrow \{p(\theta)Q(\theta, \Theta_n)\} / \{p(\Theta_n)Q(\Theta_n, \theta)\}$
 - 3: Draw a random number in the range $(0, 1]$ from a regular distribution, $r \leftarrow [0, 1]$
 - 4: **if** $r \leq \gamma$ **then**
 - 5: Accept the new point $\Theta_{n+1} = \theta$
 - 6: **else**
 - 7: Repeats the old point $\Theta_{n+1} = \Theta_n$
 - 8: **end if**
-

The Affine Invariant Algorithm

Firstly proposed by Goodman and Weare (2010), the affine invariant sampling algorithm, also known as “stretch move”, produces independent samples of the posterior distribution much faster than any MH algorithm [43, 44]. Here, it is employed a notation similar to the one adopted in [43]. The affine invariant sampler consists of K “independent” **walkers** $W = \{\Theta^k\}$ and the proposal distribution for one walker k depends on the current position of the $K - 1$ walkers in the so-called **complementary ensemble**, $W^{[k]} = \{\Theta^j, \forall j \neq k\}$.

When updating the position in parameter space for a single walker, Θ^k , a second walker, Θ^j , is drawn arbitrarily from the complementary ensemble and the proposal is given by

$$\Theta_n^k \rightarrow \theta = \Theta_n^j + Z[\Theta_n^k - \Theta_n^j], \quad (3.27)$$

Z being a random variable from a distribution $g(Z = z)$ satisfying $g(z^{-1}) = zg(z)$, so the proposal density (3.27) is symmetric.

For a set of N parameters the chain's proposal is accepted with probability

$$\gamma = \min \left\{ 1, Z^{N-1} \frac{p(\boldsymbol{\theta})}{p(\boldsymbol{\Theta}_n^k)} \right\}. \quad (3.28)$$

Goodman and Weare (2010) argued in favour of a distribution for Z given by:

$$g(Z = z) \propto \begin{cases} \frac{1}{\sqrt{z}}, & \text{if } z \in \left[\frac{1}{a}, a \right] \\ 0, & \text{otherwise.} \end{cases} \quad (3.29)$$

where a is the only adjustable parameters, set to be equal to 2 in [44]. It indirectly controls the MCMC's acceptance rate, which should be between 17% and 45%, although there's no other reason for those values except "common sense" [42]. Higher or lower acceptance rates means the algorithm has a problematic acceptance proposal density, accepting too much or too little.

Algorithm 2 Procedure for a single step in Affine Invariant algorithm.

- 1: **for** $k = 1, 2, 3, \dots, K$ **do**
 - 2: Randomly chose a walker $\boldsymbol{\Theta}_n^j$ from the complementary ensemble $W_n^{[k]}$
 - 3: Sample z from the $g(z)$ p.d.f., $Z \leftarrow g(Z = z)$
 - 4: Draw a proposal position from $\boldsymbol{\theta} = \boldsymbol{\Theta}_n^j + Z[\boldsymbol{\Theta}_n^k - \boldsymbol{\Theta}_n^j]$
 - 5: Evaluate the acceptance probability $\gamma \leftarrow z^{N-1} \{p(\boldsymbol{\theta})\} / \{p(\boldsymbol{\Theta}_n^k)\}$
 - 6: Draw a random number in the range $(0, 1]$ from a regular distribution, $r \leftarrow [0, 1]$
 - 7: **if** $r \leq \gamma$ **then**
 - 8: Accept the new point $\boldsymbol{\Theta}_{n+1}^k = \boldsymbol{\theta}$
 - 9: **else**
 - 10: Repeats the old point $\boldsymbol{\Theta}_{n+1}^k = \boldsymbol{\Theta}_n^k$
 - 11: **end if**
 - 12: **end for**
-

The Parallel Stretch Move Algorithm

The affine invariant algorithm presented before shows an incredible potential for parallelized computation, which could considerably decrease the amount of time to sample a posterior distribution around its maximum value. The parallel version of the affine invariant method consists in separate walkers into two subsets, $W^{(0)} = \{\boldsymbol{\Theta}^k, \forall k = 1, 2, 3, \dots, K/2\}$ and $W^{(1)} = \{\boldsymbol{\Theta}^k, \forall k = K/2 + 1, K/2 + 2, \dots, K\}$. Firstly, all walkers at the first subset $W^{(0)}$ are updated using the walkers's positions on the other subset $W^{(1)}$ following the procedure described by Algorithm 3. Secondly, it updates all positions from the second set of walkers $W^{(1)}$ based on the new positions of $W^{(0)}$. After this process, all walkers would have taken a new step.

Algorithm 3 Procedure for the parallel stretch move algorithm.

```

1: for  $i \in \{0, 1\}$  do
2:   for  $k = 1, 2, 3, \dots, K/2$  do ▷ Parallelizable Loop
3:     Randomly chose a walker  $\Theta_n^j$  from the complementary ensemble  $W_n^{(i)}$ 
4:      $\Theta^k \leftarrow W^{(i),k}$ 
5:     Sample  $z$  from the  $g(z)$  p.d.f.,  $Z \leftarrow g(Z = z)$ 
6:     Draw a proposal position from  $\theta = \Theta_n^j + Z[\Theta_n^k - \Theta_n^j]$ 
7:     Evaluate the acceptance probability  $\gamma \leftarrow z^{N-1} \{p(\theta)\} / \{\Theta_n^k\}$ 
8:     Draw a random number in the range  $(0, 1]$  from a regular distribution,  $r \leftarrow [0, 1]$ 
9:     if  $r \leq \gamma$  then
10:      Accept the new point  $\Theta_{n+1/2}^k = \theta$ 
11:     else
12:      Repeats the old point  $\Theta_{n+1/2}^k = \Theta_n^k$ 
13:     end if
14:   end for
15:    $n \leftarrow n + 1/2$ 
16: end for

```

This algorithm was first developed by Daniel Foreman-Mackey *et al.* (2013) as a Python package called `emcee`¹ [43], and can be easily implemented. The results presented on the next chapter were obtained mainly using this Python package, parallelized in up to 24 cores and it is fully explained on Section 4.1.

¹Available online at <http://dan.iel.fm/emcee>

Chapter 4

Method and Analysis

The main purpose of this work is to obtain cosmological parameters from a galaxy survey, with a given selection function $\bar{n}(\mathbf{r})$, and to study the impact of selection function estimation on the cosmological parameters. A combination of all theoretical probes described in previous chapters leads to a method capable of probing how the selection function affects cosmological estimations. Although the FKP estimator 2.4 is capable of subtracting most of the structure induced by $\bar{n}(\mathbf{r})$, in some cases including the selection function parameters affects the cosmological results.

The method used for analysis is presented in detail, from the connections with the main concepts formerly presented, to the construction of the **MCMaps**¹ algorithm – the code developed for this work’s analysis. Next, some considerations on a few examples of analytical convolutions between power spectra and the window function are discussed, showing what is the expected effect on estimated spectra under certain survey geometries. Section 4.3 presents a forecast for J-PAS’s LRGs on four cosmological parameters (H_0, Ω_C, w_0 , and w_a) from $0.2 < z < 1.0$, based on simulations from [10].

4.1 Method: The MCMaps Algorithm

The present Section is dedicated to explaining the main method developed for this work. Every redshift or photometric galaxy survey is subjected to effects due to the geometry of the catalog. Also, every survey is limited by volume, through both the redshift range and the sky coverage. This affects the way in which the analysis is made; limited volume always introduces **cosmic variance** and limits on the range of modes that can be probed. Besides, it is known that different types of tracers present different clustering biases and selection functions [45, 46], so it is important to comprehend how to estimate cosmological parameters from a galaxy catalog that contains structure also due the survey’s geometry.

From a given galaxy map in comoving space ², with volume V_{tot} , and divided into

¹Available online at <https://github.com/arthurmloureiro/MCMaps>

²Redshift space is not yet implemented, although this would be a simple extension of this work.

N_{cell}^3 cells (using any method like nearest-grid-point or clouds-in-cells [47] to perform this division), one estimates the FKP error bars (2.85), which will be the basis for the MCMC likelihood, Eq. (3.21). As the method consists in probing both the selection function and the cosmology, one does not wish to estimate the data power spectrum, $\hat{P}_d(k)$, separately from the theoretical estimated power spectrum, $\hat{P}_{th}^{\mathbf{q}}(k)$. Instead, the estimation of data and theoretical power spectra is left for the MCMC. As the Monte-Carlo samples both the selection function's free parameters and the cosmology, the first set alters both theory and data power spectra – Section 3.2 explains the importance of using the same selection function in both spectra.

Once the FKP error bars are estimated for the data galaxy catalog, the posterior sampling process begins. Following the **parallel stretch move**, a set of parameters $\mathbf{Q} = \{\mathbf{n}, \mathbf{q}\} = \{n_1, n_2, \dots, H_0, \Omega_\Lambda, \dots\}$ (geometrical, \mathbf{n} , and cosmological, \mathbf{q}) is chosen. The process of sampling the posterior is the same described in Section 3.2: given the selection function parameters, the data galaxy power spectrum is estimated. Meanwhile, using the cosmological parameters \mathbf{q} , a **CAMB** matter power spectrum is generated and used to create galaxy mock catalogs (as described in 2.3). With the same selection function parameters \mathbf{n} used to estimate the data power spectrum, one estimates also the theoretical galaxy power spectrum from the mocks and calculate the multivariate likelihood (4.1), flat priors (4.2), and the resulting posterior distribution (4.3).

$$\mathbb{K} = -\frac{1}{N_b} \sum_{i=1}^{N_b} \frac{[\hat{P}_d^{\mathbf{n}}(k_i) - \hat{P}_{th}^{\mathbf{q}, \mathbf{n}}(k_i)]^2}{2\sigma_d^2(k_i)} \quad (\text{Gaussian Log-Likelihood}) \quad (4.1)$$

$$prob(\mathbf{Q}|I) = \begin{cases} 1, & \text{if } (\mathbf{Q}_{min} < \mathbf{Q} < \mathbf{Q}_{max}); \\ 0, & \text{otherwise;} \end{cases} \quad (\text{Flat Priors}) \quad (4.2)$$

$$prob(\mathbf{Q}|\{\text{data}\}, I) \propto \sum_{i=1}^{N_b} \exp \left\{ \frac{[\hat{P}_d^{\mathbf{n}}(k_i) - \hat{P}_{th}^{\mathbf{q}, \mathbf{n}}(k_i)]^2}{\sigma_d^2(k_i)} \right\} \times prob(\mathbf{Q}|I) \quad (\text{Posterior Distribution}). \quad (4.3)$$

The MCMaps code was developed in **Phyton** and uses the **emcee** parallel stretch move package [43] to sample the posterior. It can probe up to 9 cosmological parameters, H_0 , Ω_b , Ω_C , Ω_Λ , Ω_ν , n_s , and τ . All analysis on this chapter were made using the following fiducial cosmology:

- $H_0 = 72\text{km/s/Mpc}$;
- $\Omega_b = 0.0462$;
- $\Omega_C = 0.2538$;
- $\Omega_\Lambda = 0.70$;
- $\Omega_K = 0.0$;
- $\Omega_\nu = 0.0$;
- $w_0 = -1.0$;
- $w_a = 0.0$;

- $n_s = 0.96$ (spectral index);
- $\tau = 0.09$ (optical depth);

Given sufficient steps – which might depend on the number of parameters to be estimated – enough of the posterior is sampled, allowing to obtain the two- and one-dimensional distributions for each parameter. A more detailed explanation of the method can be found in algorithm 4.

Algorithm 4 The MCMaps algorithm.

- 1: Reads the data galaxy map, N_{ijl}^{data}
 - 2: Reads the user's input like cell size, number of cells, cosmological parameters to estimate and more
 - 3: Estimates the data FKP error bars, $\sigma_d^2(k)$, from (2.85)
 - 4: Begins with the parallel stretch move MCMC
 - 5: **for** $i \in \{0, 1\}$ **do** ▷ For N_s steps each walker will give
 - 6: **for** $k = 1, 2, 3, \dots, K/2$ **do** ▷ Parallelizable Loop
 - 7: Randomly chooses a walker $\mathbf{Q}_n^j = \{\mathbf{n}, \mathbf{q}\}$ from the complementary ensemble $W_n^{(i)}$
 - 8: $\mathbf{Q}^k \leftarrow W^{(i),k}$
 - 9: Samples z from the p.d.f. $g(z)$, (3.29)
 - 10: Draws a proposal position from $\mathbf{Q}' = \mathbf{Q}_n^j + Z[\mathbf{Q}_n^k - \mathbf{Q}_n^j]$
 - 11: Calculates the theoretical matter power spectrum from linear perturbation theory using the drawn set of cosmological parameters, $\mathbf{q}' = \{H_0, \Omega_C, \dots\}$, using **CAMB**
 - 12: Generates galaxy mock catalogs using the theoretical matter power spectra from the previous step – as described in Section 2.3
 - 13: Uses the set of selection function parameters, \mathbf{n}' , to estimate both data and theoretical power spectra
 - 14: Evaluates a value for the posterior distribution using (4.3)
 - 15: Evaluates the acceptance probability $\gamma \leftarrow z^{N-1} \{p(\mathbf{Q}')/\mathbf{Q}_n^k\}$
 - 16: Draws a random number $r \in (0, 1]$ from a regular distribution
 - 17: **if** $r \leq \gamma$ **then**
 - 18: Accepts the new point $\mathbf{Q}_{n+1/2}^k = \mathbf{Q}'$
 - 19: **else**
 - 20: Repeats the old point $\mathbf{Q}_{n+1/2}^k = \mathbf{Q}_n^k$
 - 21: **end if**
 - 22: **end for**
 - 23: $n \leftarrow n + 1/2$
 - 24: **end for**
-

4.2 Analytical Considerations

Another main goal of this work is to comprehend how the convolution with the window function affects the estimated power spectrum. Understanding it is an important step to study how a deconvolution, here performed by the MCMC, behaves. At the present Section, some reasonable selection functions are considered assuming radial dependence only. Going all the way to the window function and the resulting convolution with the power spectrum, the effects of the convolution are discussed and a final Monte-Carlo simulation shows these effects of selection function marginalization on the cosmological parameters.

One can start the development of the window function convolution formalism through Eq. (2.78), from which one obtains:

$$\hat{P}(\mathbf{k}) = \frac{1}{(2\pi)^3} \int d^3k' P(\mathbf{k}') |G(\mathbf{k} - \mathbf{k}')|^2. \quad (4.4)$$

The actual estimated power spectrum arises when averaging over Fourier space \mathbf{k} -shells of volume $V_{k_i} \sim 4\pi k_i^2 \Delta k$. Here, $k_i = (k_{max} + k_{min})/2$ and $\Delta k = k_{max} - k_{min}$, where k_{max} and k_{min} are respectively the upper and lower limits of the \mathbf{k} -shells. The volume average is then evaluated as:

$$\begin{aligned} \hat{P}(k_i) &= \frac{1}{V_k} \int_{V_k} d^3k \hat{P}(\mathbf{k}) \\ &= \underbrace{\frac{1}{V_k}}_{\simeq 1/4\pi k_i^2 \Delta k} \int_{V_k} d^3k \int \frac{d^3k'}{(2\pi)^3} \underbrace{P(\mathbf{k})}_{\sim P(k)} |G(\mathbf{k} - \mathbf{k}')|^2 \\ &= \frac{1}{4\pi k_i^2 \Delta k} \int_{k_{min}}^{k_{max}} dk k^2 \int d^2\hat{k} \int \frac{d^3k'}{(2\pi)^3} P(k') |G(\mathbf{k} - \mathbf{k}')|^2. \end{aligned} \quad (4.5)$$

The first integral can be expressed by taking the limit where the thickness of the \mathbf{k} -shells goes to zero, $\lim_{\Delta k \rightarrow 0}$, hence $k_i \rightarrow k$ and one has:

$$\hat{P}(k) = \int \frac{dk'}{2\pi^2} k'^2 P(k') \int \frac{d^2\hat{k}}{4\pi} \int \frac{d^2\hat{k}'}{4\pi} |G(\mathbf{k} - \mathbf{k}')|^2 \quad (4.6)$$

The last two integrals from the expression above perform angular averages on the window function over $\mathbf{k} - \mathbf{k}'$. However, given the conditions stated above about the radial dependence, choosing the line of sight to be aligned with one of the Fourier modes, one can express $|G(\mathbf{k} - \mathbf{k}')|^2 \approx |G(|\mathbf{k} - \mathbf{k}'|)|^2$, with $|\mathbf{k} - \mathbf{k}'| = \sqrt{k^2 + k'^2 - 2kk'\mu_k}$, where μ_k is the cosine between the two Fourier modes. Given this, the last two integrals (which are actually four integrals, one over each of the four angles considered) can be transformed into only one.

It is helpful to redefine the window function in terms of these angular averages,

$$\begin{aligned}
\tilde{W}(k, k') &\equiv \frac{1}{2\pi^2} \int \frac{d^2\hat{k}}{4\pi} \int \frac{d^2\hat{k}'}{4\pi} |G(|\mathbf{k} - \mathbf{k}'|)|^2 \\
&= \frac{1}{2\pi^2} \int_{-1}^1 \frac{d\mu_k}{2} \int_0^{2\pi} \frac{d\phi_k}{2\pi} \int_{-1}^1 \frac{d\mu_{k'}}{2} \int_0^{2\pi} \frac{d\phi_{k'}}{2\pi} |G(|\mathbf{k} - \mathbf{k}'|)|^2 \\
&= \frac{1}{2\pi^2} \int_{-1}^1 \frac{d\mu_k}{2} |G(|\mathbf{k} - \mathbf{k}'|)|^2.
\end{aligned} \tag{4.7}$$

So, the convolved power spectrum can be rewritten as

$$\hat{P}(k) = \int dk' k'^2 P(k') \tilde{W}(k, k'). \tag{4.8}$$

In the infinite volume limit, with $\bar{n} = \text{const}$, $\tilde{W}(k, k') \rightarrow 1/k^2 \delta_D(k - k')$, meaning that no modes are mixed by the convolution. Notice that the $\tilde{W}(k, k')$ has dimension of $(\text{length})^3$, or $(k)^{-3}$ – see Eq. (4.8).

From Eq. (2.80), one can go from a given selection function $\bar{n}(r)$ all the way to the convolved power spectrum (4.8), as the window function the square modulus of the Fourier transformed weighted selection function, $G(r)$. This simple approach allows to develop an intuition about how the selection function might affect the estimated power spectrum, and also its cosmological parameters.

4.2.1 Top-Hat Selection Function

The simplest case for a selection function is the Fourier pixel, also known as the **top-hat** selection function. This case simply filters the survey up to a characteristic scale R , allowing to obtain better estimates on the power spectra for this particular scale [15]. The top-hat selection function is defined as

$$\bar{n}(\mathbf{r}) = \frac{1}{V} \Theta_H(\mathbf{r} - \mathbf{R}) \tag{4.9}$$

where Θ_H is the Heaviside step function. Starting from Eq. (2.80), the limit where $w(\mathbf{r}) \sim \bar{n}(\mathbf{r})$, its Fourier transform can be expressed as

$$\begin{aligned}
G(\mathbf{k} - \mathbf{k}') &= \frac{1}{N} \int \frac{d^3r}{V} e^{-i(\mathbf{k} - \mathbf{k}') \cdot \mathbf{r}} \Theta_H(\mathbf{r} - \mathbf{R}) \\
&= \frac{1}{N} \frac{2\pi}{V} \int_0^R dr r^2 \int_{-1}^1 d\mu e^{i|\mathbf{k} - \mathbf{k}'|r\mu} \\
&= \frac{1}{N} \frac{4\pi}{V} \int_0^R dr r \frac{\sin(|\mathbf{k} - \mathbf{k}'|r)}{|\mathbf{k} - \mathbf{k}'|} \\
&= \frac{1}{N} \frac{4\pi}{V(|\mathbf{k} - \mathbf{k}'|)^3} \{\sin(|\mathbf{k} - \mathbf{k}'|R) - |\mathbf{k} - \mathbf{k}'|R \cos(|\mathbf{k} - \mathbf{k}'|R)\},
\end{aligned} \tag{4.10}$$

where N is a normalization constant given by Eq. (2.75). Now, defining $\alpha \equiv |\mathbf{k} - \mathbf{k}'|R$, leads to

$$\begin{aligned} G(\alpha) &= \frac{3}{\alpha^3}(\sin \alpha - \alpha \cos \alpha) \\ &= \frac{3}{\alpha} j_1(\alpha) \end{aligned} \quad (4.11)$$

where $j_1(\alpha)$ is the first order Bessel Spherical function. Then, one can evaluate the window function from expression (4.7), changing the integrand from $d\mu$ to $d\alpha$.

$$\begin{aligned} \tilde{W}(k, k') &= \frac{1}{2\pi^2 N^2} \frac{9}{2kk'R^2} \int_{|k-k'|R}^{(k+k')R} \frac{d\alpha}{\alpha^2} j_1^2(\alpha) \\ &= \frac{1}{2\pi^2 N^2} \frac{9}{2kk'R^2} \left\{ \frac{1}{30\alpha^5} \left[-3 - 5\alpha^2 + (3 - \alpha^2 + 2\alpha^4) \cos(2\alpha) + 6\alpha \sin(2\alpha) \right. \right. \\ &\quad \left. \left. + \alpha^3 \sin(2\alpha) + 4\alpha^5 \int_0^{2\alpha} \frac{\sin(x)}{x} dx \right] \right\}_{|k-k'|R}^{(k+k')R} \end{aligned} \quad (4.12)$$

This window function is plotted as a function of k and k' in a 2D matrix in Figure 4.1. From this figure, one can see that the top-hat selection function generates a window function that selects modes close by a certain scale. Although it becomes more clear when looking at Figure 4.2, showing the window function for two specific Fourier modes, $k' = 0.005$ and $k' = 0.05$.

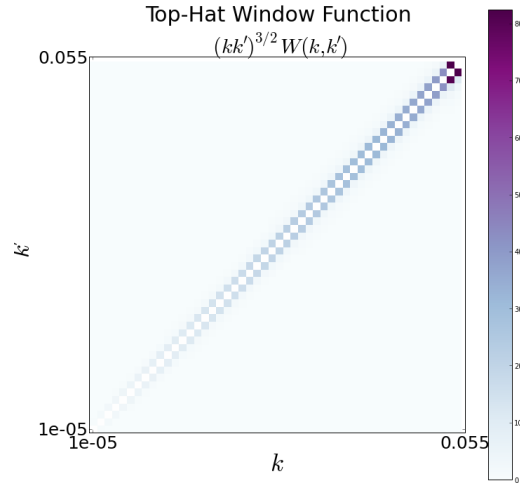


Figure 4.1: $(kk')^{3/2} \tilde{W}(k, k')$ for equally spaced bins from $k, k' = 1 \times 10^{-5}$ to 0.055 and $R = 150 \text{ Mpc } h^{-1}$.

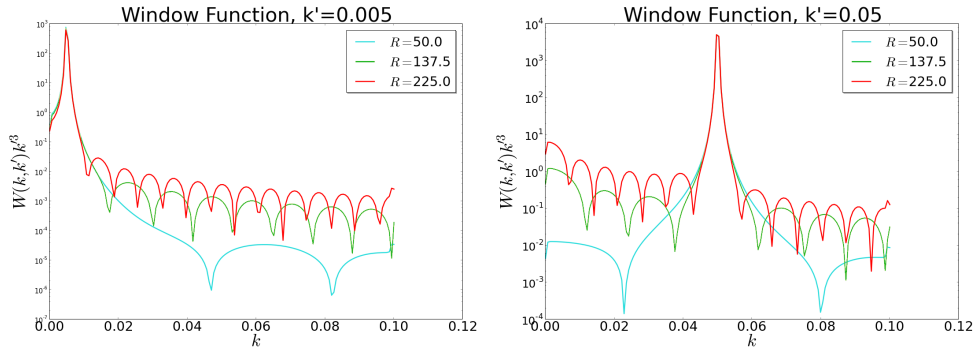


Figure 4.2: Window function $\tilde{W}(k, k')$ for three different values of R (in Mpc h^{-1}) fixing $k' = 0.005$ (left) and fixing $k' = 0.05$ (right). The amplitude of the main peak is independent of the survey's scale R , while the width of the other peaks get thicker with lower values of it.

To understand how the window function affects the power spectrum estimation, the convolution in (4.8) was numerically performed in a realistic **CAMB** matter power spectrum. The results for these convolutions are shown in Figure 4.3 for the same three values of the parameter R .

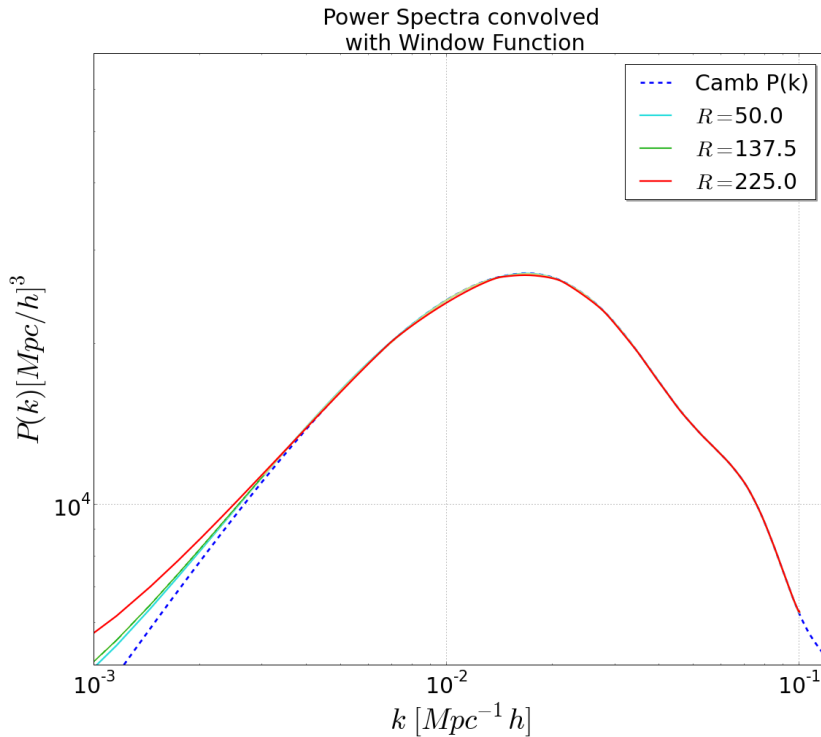


Figure 4.3: $P(k)$ convolved with a top-hat window. The spectra only differs for small values of k , *i.e.*, for large-scales. This is expected, since the top-hat selection function limits the volume of the survey to a spherical region of radius R .

One can see, from Figure (4.3), that for lower values R , the convolved spectra look a lot like the fiducial one, keeping the positions of the acoustic wiggles. As the convolution with a top-hat window leads to almost the same spectra as the real one, almost no changes were expected to happen on the cosmological parameters due the selection function effects. The following cases show a different situation.

4.2.2 Inverse Square Selection Function

Consider now a simple selection function that behaves as an inverse square law, also with one free parameter, A_r . This means that galaxy counts in the survey decay as the comoving radius of the survey gets higher. This is a simplified case of real-life surveys whose galaxy detection decays over redshift:

$$\bar{n}(\mathbf{r}) = \bar{n}(r) = \frac{A_r}{r^2} \quad (4.13)$$

Using the same weighting scheme as presented in PVP or FKP [31, 30], one can express the Fourier transform of Eq. (2.80) as:

$$\begin{aligned} G(\mathbf{k} - \mathbf{k}') &= \frac{1}{N} \int d^3r \frac{A_r}{A_r + r^2} e^{i(\mathbf{k} - \mathbf{k}') \cdot \mathbf{r}} \\ &= \frac{4\pi}{N} \int_0^\infty dr r^2 \frac{A_r}{A_r + r^2} \frac{\sin(|\mathbf{k} - \mathbf{k}'|r)}{|\mathbf{k} - \mathbf{k}'|r} \\ &= \frac{2\pi^2}{N} \frac{A_r e^{-\sqrt{A_r}|\mathbf{k} - \mathbf{k}'|}}{|\mathbf{k} - \mathbf{k}'|}. \end{aligned} \quad (4.14)$$

Then, to evaluate the window function (4.7), recall that $|\mathbf{k} - \mathbf{k}'| = \sqrt{k^2 + k'^2 - 2kk'\mu_k}$. So, the angular average of $|G(|\mathbf{k} - \mathbf{k}'|)|^2$ can be expressed as

$$\tilde{W}(k, k') = \frac{4\pi^4 A_r^2}{2\pi^2 N^2} \int_{-1}^1 \frac{d\mu_k}{2} \frac{\exp\{-2\sqrt{A_r} \sqrt{k^2 + k'^2 - 2kk'\mu_k}\}}{\sqrt{k^2 + k'^2 - 2kk'\mu_k}}. \quad (4.15)$$

Substituting $x = k^2 + k'^2 - 2kk'\mu_k \rightarrow dx = -2kk'd\mu_k$, the expression above becomes

$$\begin{aligned} \tilde{W}(k, k') &= \left(\frac{1}{2\pi^2 N^2} \right) \frac{4\pi^4 A_r^2}{2kk'} \int_{|k-k'|^2}^{(k+k')^2} \frac{dx}{2} \frac{e^{-2\sqrt{A_r}x}}{\sqrt{x}} \\ &= \left(\frac{1}{2N^2} \right) \frac{\pi^2 A_r^{3/2}}{kk'} \left[e^{-2\sqrt{A_r}|k-k'|} - e^{-2\sqrt{A_r}(k+k')} \right] \end{aligned} \quad (4.16)$$

Plotting the window function of Eq. (4.16) as a 2D matrix function of k and k' (Figure 4.4), one can see that it is symmetrical under $k \leftrightarrow k'$ and peaks at $k = k'$.

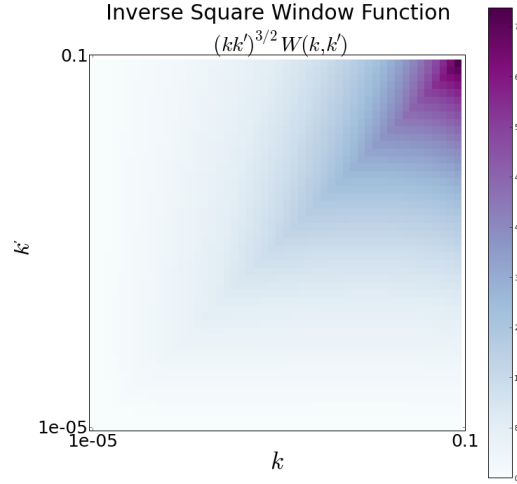


Figure 4.4: $(kk')^{3/2}\tilde{W}(k, k')$ for equally spaced bins from $k, k' = 1 \times 10^{-5}$ to 0.1 and $A_r = 90 \text{ Galaxies}/\text{Mpc } h^{-1}$.

From figure 4.5 one can see the window function effect with k' is fixed. The inverse squared window function mixes all modes with different amplitudes, in a way which is regulated by A_r . Higher values of A_r lead to higher amplitudes of $\tilde{W}(k, k')$. It is important to observe that despite the peak on $k = k'$. Notice that the selection function's geometry does not change with the free parameter, A_r , but the window function's geometry does. The window function is not simply the Fourier transform of $\bar{n}(r)$ in this case, it also takes into account the weights, which explains how A_r affects it.

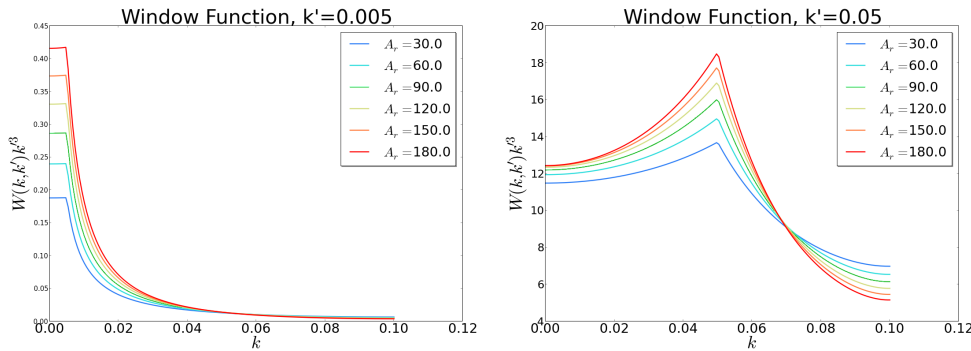


Figure 4.5: Window function $\tilde{W}(k, k')$ for different values of A_r (in Galaxies/ Mpc h^{-1}) fixing $k' = 0.005$ (left) and fixing $k' = 0.05$ (right). Differently from the last case, here the amplitude of the window function has a dependence on the selection function's free parameter.

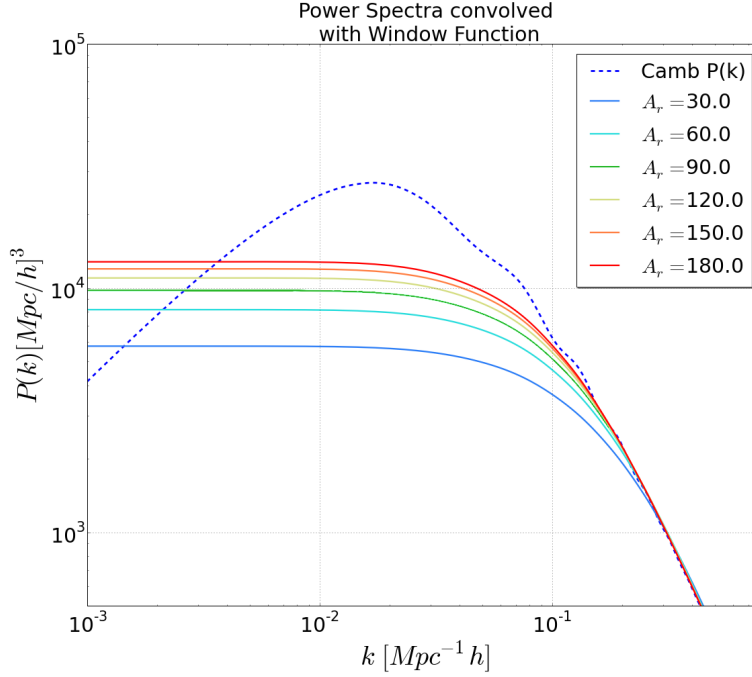


Figure 4.6: $\hat{P}(k)$ convolved with a inverse square window.

Now, performing the numerical convolution between the window (4.16) and the **CAMB** matter power spectrum, one can see that some Fourier modes are suppressed according to the value of A_r , with higher values of A_r suppressing less the power spectrum on large-scales. Even so, the effects of the convolution on the estimated power spectra (Figure 4.6) are remarkable and drastically change “knee” of the spectra. This convolution implies that at least estimates for Ω_C , H_0 , Ω_b and Ω_Λ will be affected. Also, one can see that the acoustic wiggles are gone, which means that no measurements of baryonic acoustic oscillations can be used as standard ruler, leading to completely wrong estimates on dark energy parameters such as w_0 and w_a .

4.2.3 Gaussian Selection Function

The last analytical convolution case considered here is a Gaussian selection function – another reasonable case of survey geometry. With only one free parameter, the spread σ_r , the Gaussian selection function can be expressed as

$$\bar{n}(r) = \frac{V}{(2\pi)^{3/2}\sigma_r^3} e^{-r^2/2\sigma_r^2} \quad (4.17)$$

whose Fourier transform, as in the last two cases, can be expressed as

$$G(|\mathbf{k} - \mathbf{k}'|) = \frac{1}{N} e^{-|\mathbf{k} - \mathbf{k}'|^2 \sigma_r^2 / 2}. \quad (4.18)$$

Again, one uses expression (4.7) to evaluate the window function as the angular average of $|G(|\mathbf{k} - \mathbf{k}'|)|^2$, using $|\mathbf{k} - \mathbf{k}'| = \sqrt{k^2 + k'^2 - 2kk'\mu_k}$. The resulting 2D matrix in terms of k and k' is presented in Figure 4.7.

$$\begin{aligned}
\tilde{W}(k, k') &= \frac{1}{2\pi^2 N^2} \int_{-1}^1 \frac{d\mu_k}{2} \exp \left\{ -\frac{\sigma_r^2}{2} (k^2 + k'^2 - 2kk'\mu_k) \right\} \\
&= \frac{1}{2\pi^2 N^2} e^{-\sigma_r^2(k^2+k'^2)} \int_{-1}^1 \frac{d\mu_k}{2} \exp\{2\sigma_r^2 kk' \mu_k\} \\
&= \frac{1}{2\pi^2 N^2} \left(\frac{e^{-\sigma_r^2(k^2+k'^2)}}{4\sigma_r^2 kk'} \right) \left[e^{2\sigma_r^2 kk'} - e^{-2\sigma_r^2 kk'} \right] \\
&= \frac{1}{2\pi^2 N^2} \left(\frac{e^{-\sigma_r^2(k^2+k'^2)}}{2\sigma_r^2 kk'} \right) \sinh(2\sigma_r^2 kk')
\end{aligned} \tag{4.19}$$

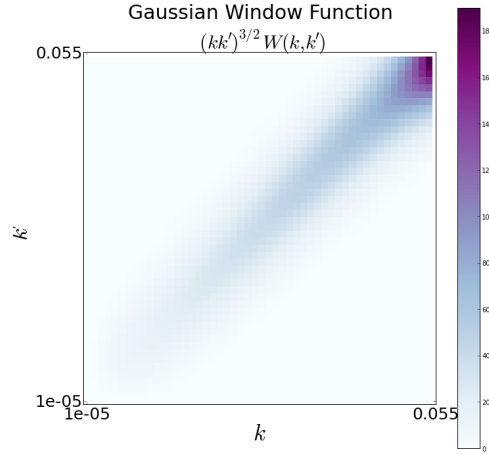


Figure 4.7: $(kk')^{3/2}\tilde{W}(k, k')$ for a Gaussian window using equally spaced bins from $k, k' = 1 \times 10^{-4}$ to 0.055 and $\sigma_r = 130 \text{ Mpc } h^{-1}$.

Once again, one can see that there is a symmetry between $k \Leftrightarrow k'$ and the window's maximum value happens when $k = k'$. From the one-dimensional plot of the window function (Figure 4.8), it is possible to see that the Gaussian window averages over nearly Gaussian bins of k , whose peaks change depending on the value of k' considered, as well as on the spread, σ_r . For lower values of k' , the position of the peak is almost the same at the origin, and the spread influences more the window's phase. As for higher values of k' , the peak positions change from lower values of k' going to higher values as the spread increases. For even higher values of σ_r , as expected, the window function gets closer and closer to a Dirac Delta, $\lim_{\sigma_r \rightarrow \infty} \tilde{W}(k, k', \sigma_r) \rightarrow 1/k^2 \delta_D(k - k')$. Such effect reflects itself on the convolution as the estimated spectrum gets closer to the real spectrum.

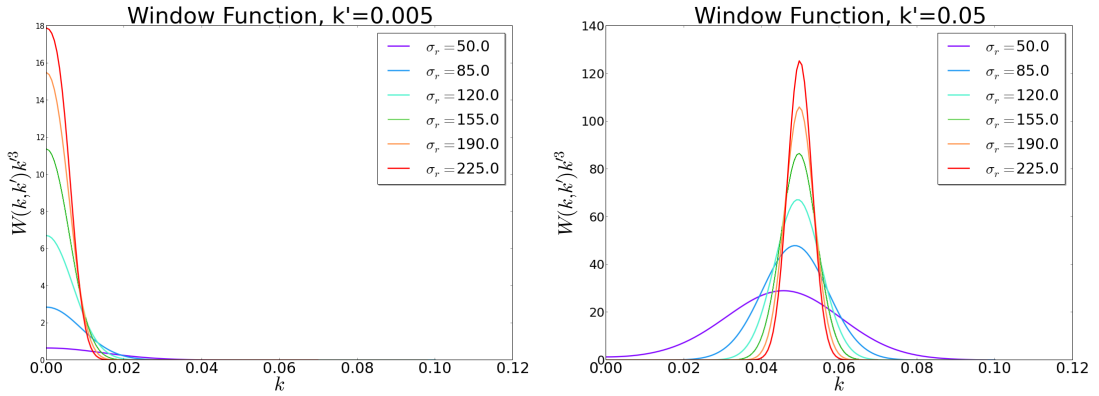


Figure 4.8: Window function $\tilde{W}(k, k')$ using different values of the spread σ_r (in Mpc h^{-1}) fixing $k' = 0.005$ (left) and fixing $k' = 0.05$ (right). As expected, since the Gaussian window is the Fourier transform of a Gaussian selection function, a small spread σ_r reflects in a wider window.

The estimated power spectra for this case show interesting features. When σ_r is large enough, the Gaussian window goes to the Dirac Delta limit (as said above), but as it gets smaller, the convolution mimics some different acoustic features on $\hat{P}(k)$, changing the position of peaks and their amplitudes. This scenario presents a complication when trying to obtain cosmological parameters using $\hat{P}(k)$. Since the acoustic peaks are slightly different, some cosmological parameters that are sensitive to the peak positions and amplitudes (mainly H_0 , Ω_m , Ω_c , Ω_b , w_0 and w_a) will result in biased estimates, even after marginalizing over selection function parameters.

As an illustration, an MCMC is performed for this case considering three free parameters for the selection function instead of only one. These parameters are \bar{n}_0 , the mean density of galaxies in the survey; a displacement, R ; and a spread, σ_r .

$$\bar{n}(|\mathbf{r}|) = \bar{n}_0 \exp \left\{ -\frac{(|\mathbf{r}| - R)^2}{\sigma_r^2} \right\} \quad (4.20)$$

This case was analysed using a $128 \times 128 \times 128$ grid, with cell size $L_{\text{cell}} = 10 \text{Mpc h}^{-1}$ – total volume of $2.097 \text{Gpc}^3 \text{h}^{-3}$ –, using the fiducial cosmology quoted in 4.1. The free cosmological parameters were H_0 , Ω_C , w_0 and w_a – and all analysis in this work were made probing these four cosmological parameters since they are more sensitive to changes on the acoustic peaks of the galaxy power spectrum. The Monte-Carlo was performed using 512 walkers with 500 steps each, meaning that the posterior was sampled with $256k$ points in a 7-dimensional parameter space. For this case, a burn in of $70k$ points was used (since the criteria for burn in is irrelevant for the given analysis, this information is omitted for future results).

In this work, MCMC results are quoted in two different ways – since there’s no agreement about which value to quote as the best-fit value [39]. First, using the one-dimensional

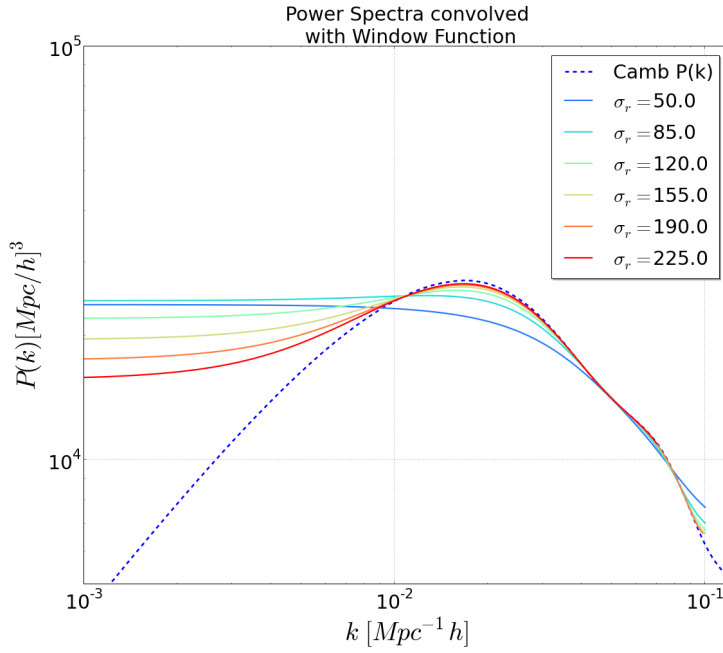


Figure 4.9: $\hat{P}(k)$ convolved with a Gaussian window. Note the change on the peak's positions and amplitudes as σ_r varies. As σ_r values get higher, the Gaussian window goes to a Dirac Delta and the convolution reflects the real power spectrum for scales smaller than $k = 10^{-2} \text{Mpc}^{-1} h$

marginalized distributions³ and evaluating its mean value and standard deviation (see Table 4.1). Second, the values presented in Figure 4.11, which were evaluated from maximum likelihood coordinates in parameter space as the best-fit value, while the error bars are the region enclosing 68.26% (1σ) of the points around the best-fit value. Figure 4.11 also shows values of two different cases: fixing the selection function parameters at their best-fit values; and allowing the selection function parameters to be treated as nuisance parameters, *i.e.*, marginalizing over them. In addition, Figure 4.10 shows the two-dimensional distributions for joint probabilities of all 7 parameters showing some correlation between some subsets.

The selection function effect is clear in Figure 4.11, for all four cosmological parameters the error bars decrease considerably, while the best-fit value gets closer to the fiducial value – except for the w_0 parameter, but further analysis show that this parameter is sensitive to different slices of redshift. These considerations demonstrate that the convolved power spectrum is affected by the nuisance parameters of the selection function. Hence, marginalizing over them alters the estimation of cosmological parameters.

³ Recall from Section 3.3 that, for a Monte-Carlo Markov Chain simulation, marginalizing over one or more parameters is the same as projecting the sampled posterior distribution on the parameter's subspace.

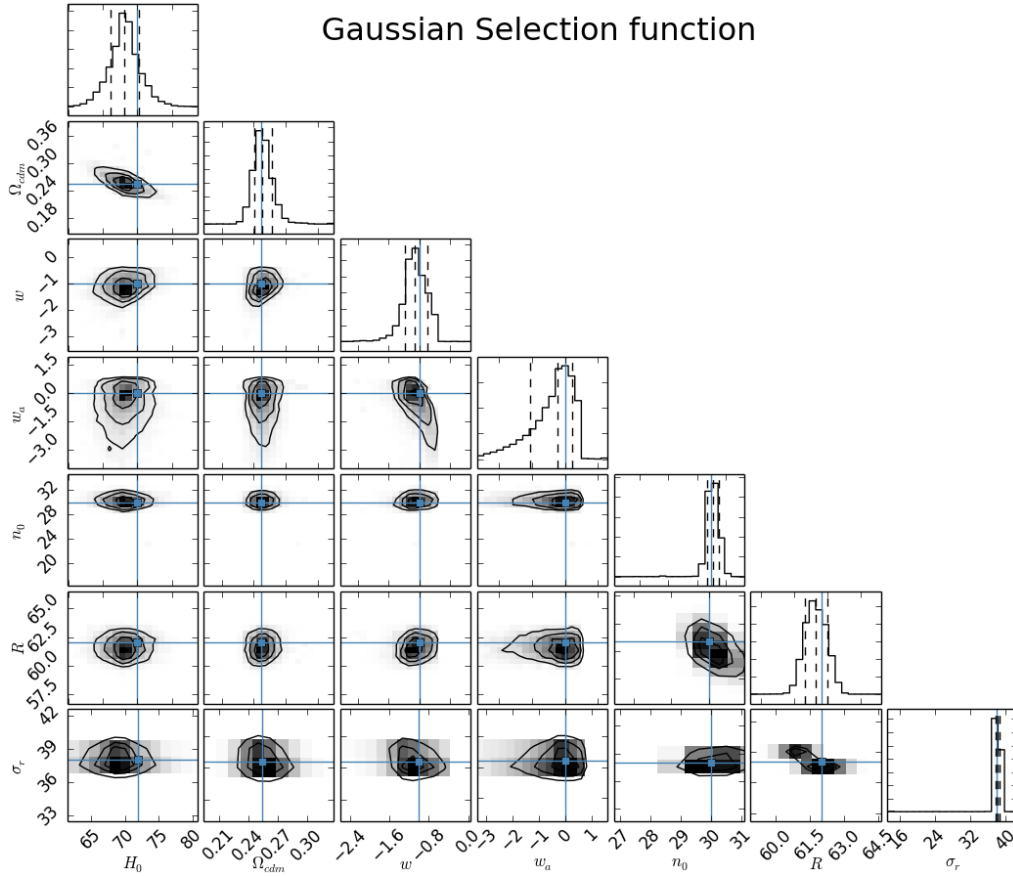


Figure 4.10: One- and two-dimensional distributions for the estimated parameters H_0 , Ω_c , w_0 , w_a , $\bar{n}_{0,z}$, R and σ_r for the Gaussian selection function. Blue lines show the true values for each parameter. Note the expected correlation between H_0 and Ω_c and the correlation between two of the selection function's parameters \bar{n}_0 and R .

Parameter	Fiducial Value	Mean Value	Standard Deviation
H_0	72	69.07	± 3.46
Ω_C	0.2538	0.25711	$\pm 2.268 \times 10^{-2}$
w_0	-1.0	-1.144	± 0.3920
w_a	0.0	-0.544	± 0.989
\bar{n}_0	30.0	30.052	± 1.555
R	62.0	61.513	± 1.012
σ_r	38.0	37.840	± 2.120

Table 4.1: Mean value and standard deviations as best-fit values for the one-dimensional marginalized distribution as the results of the MCMC run using a Gaussian Selection function (4.20). H_0 is expressed in $Mpc/km/s$, \bar{n}_0 in $gal/cell$, R and σ_r in $Mpc h^{-1}$.

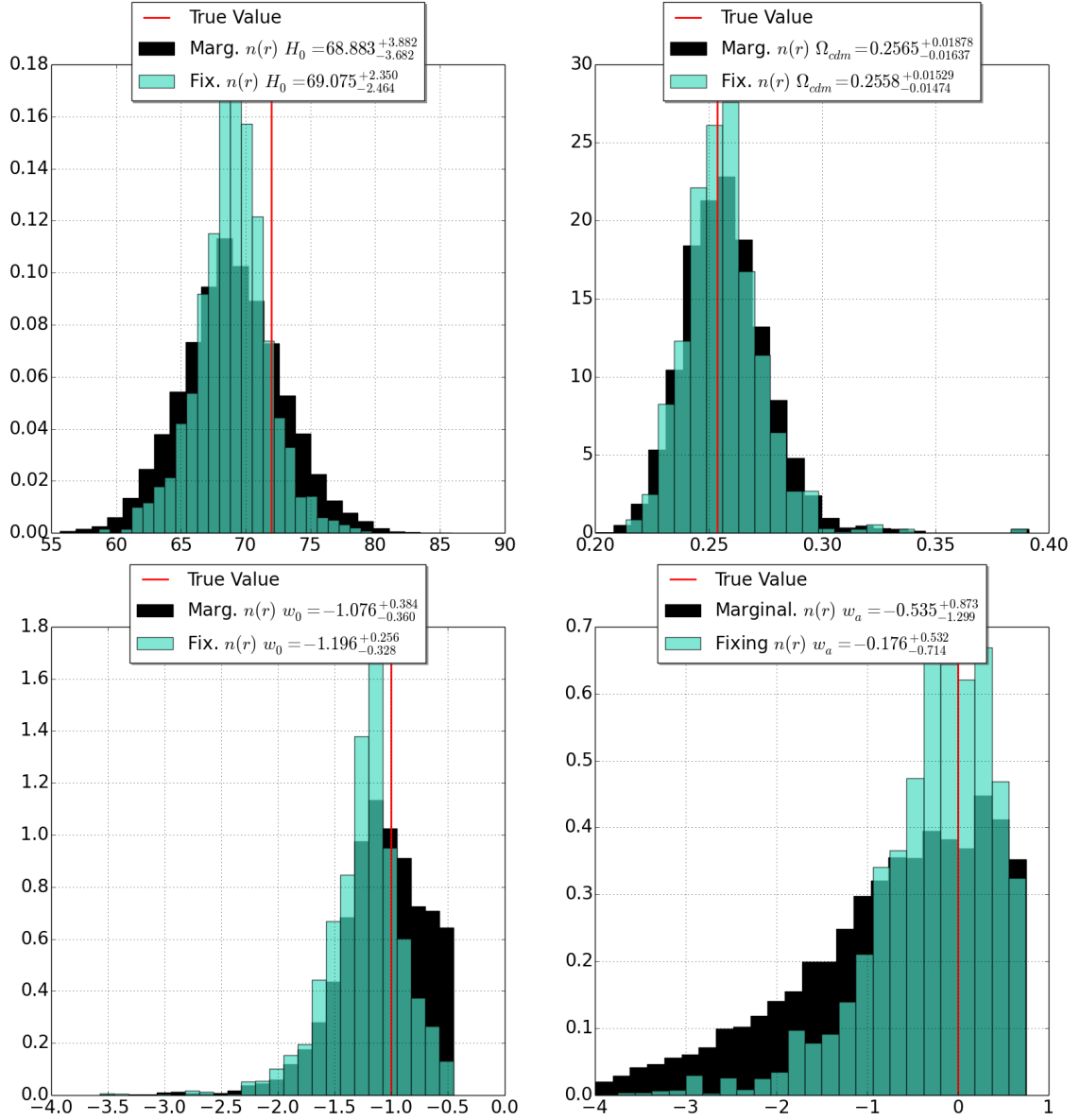


Figure 4.11: (Gaussian Selection Function) One-dimensional marginalized distributions for H_0 (upper left), Ω_c (upper right), w_0 (lower left), and w_a (lower right). Two cases are presented, (green) fixing the selection function parameters at their fiducial values ($\bar{n}_{0,0.3} = 30.0 \text{ gal/cell}$, $R = 62.0 \text{ Mpc } h^{-1}$, and $\sigma_r = 38.0 \text{ Mpc } h^{-1}$) and (black) marginalizing over all other estimated parameters, considering the selection function parameters as nuisance. Red lines are the true values. Note that the values quoted are not the maximum of the marginalized distributions, but the coordinate in parameter space of the maximum likelihood value. Best-fit values for all parameters get closer to the true value, the only exception is w_0 , which deviates from the fiducial value but presents a considerable decrease on its error bars.

4.3 J-PAS LRGs Forecast

Luminous Red Galaxies proved useful for the study of LSS and as probes of BAOs [11]. The present Section uses the method and algorithm discussed in Section 4.1 with the results from mock simulations for photometric redshift LRGs presented in Table 8 of the J-PAS White Paper [10]. Forecasts for J-PAS LRGs surface density of galaxies were made considering three groups of photometric estimated errors: 0.3%, 1.0% and 3.0%. For large-scale structure studies, it is important to keep photometric errors on redshift estimations as low as possible. Therefore, the data considered here for forecasts makes use of the 0.3% photo-z errors estimates on counts of LRGs from the J-PAS White Paper.

For the present considerations, bias is assumed to be unit ($b = 1$). Note that a unity bias **does not reflect the true bias** of LRGs, which is around $b_{LRG} \sim 1.6$ at $z \sim 0.5$. The reason for this choice lies on the fact that the log-normal density field (2.64) introduces another kind of bias, which becomes worse as $b \gg 1$. As the main purpose of this work is to probe geometrical effects on cosmological parameters, assuming a bias different from one can introduce a variety of effects that can be mixed with the geometrical effects due to the selection function estimation. The LRGs forecast in the present Section is therefore just a forecast in the geometrical sense.

Distances and lengths are expressed in comoving radius, Eq. (1.36), and the redshift bins considered for this forecast are centred at $z_1 = 0.3$, $z_2 = 0.5$, $z_3 = 0.7$ and $z_4 = 0.9$, all having a redshift thickness of 0.2, which means that the forecast's total range is $0.2 < z < 1.0$. The expected number of galaxies per $Mpc^3 h^{-3}$ for each redshift slice is presented on Table 4.2. Using this data, a fit for a selection function as a function of comoving radius leads to

$$\bar{n}(r) = \alpha \exp \left\{ - \left(\frac{r}{\beta} \right)^2 - \left(\frac{r}{\gamma} \right)^4 \right\} \quad (4.21)$$

with $\alpha = 0.005$ Galaxies / $Mpc^3 h^{-3}$, $\beta = 2000$ Mpc h^{-1} and $\gamma = 1800$ Mpc h^{-1} . The J-PAS LRGs selection function is plotted in Figure 4.12 as a function of comoving radius.

As Figure 4.12 suggests, for each of the bins centered in $z_i = 0.3, 0.5, 0.7, 0.9$, a galaxy mock catalog is produced with a “local” selection function (4.22) that fits the total selection function inside a cube $z_{min} < z_i < z_{max}$, where $z_{min} = z_i - 0.1$ and $z_{max} = z_i + 0.1$, and following the decay law:

$$\bar{n}_z(r) = \bar{n}_{0,z} \exp\{-c_{1,z} r\}. \quad (4.22)$$

Here, $\bar{n}_{0,z}$ is the expected number of galaxies in the central redshift and $c_{1,z}$ is rate of the derivative of (4.21) (at the comoving radius of the central redshift of the map).

The procedure for the present forecast goes as follows: for each redshift bin, a mock

Redshift (z)	Comoving Radius at z [Mpc h^{-1}]	$\bar{n}(r_z)$ [Galaxies/Mpc ³ h^{-3}]
0.2	795.7	4.108×10^{-3}
0.3	1164.8	2.989×10^{-3}
0.4	1514.4	1.707×10^{-3}
0.5	1845.1	7.077×10^{-4}
0.6	2157.3	1.984×10^{-4}
0.7	2451.8	3.560×10^{-5}
0.8	2729.6	3.921×10^{-6}
0.9	2991.6	2.59×10^{-7}
1.0	3238.9	1.016×10^{-8}

Table 4.2: Expected number of LRGs per $Mpc^3 h^{-3}$ in each redshift bin from 0.2 to 1.0 for 0.3% photo-z errors LRGs. Data extracted from Benitez *et al.* (2014)[10]. Bold columns are the central redshift data used for each of the analysis.

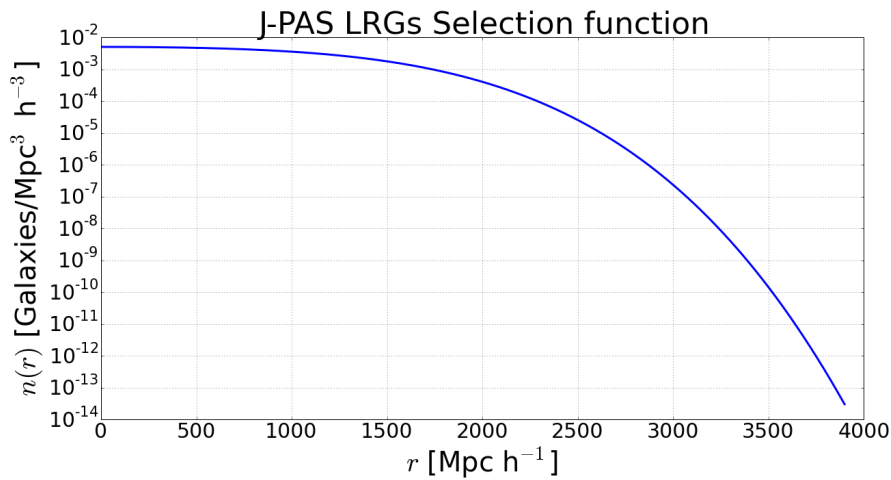


Figure 4.12: Fit for the J-PAS LRGs selection function (4.21) using data from Table 4.2.

galaxy catalog is generated containing the local selection function (4.22) in a cube with an effective volume $V_{eff}(z_i) = [V_c(z_{max}) - V_c(z_{min})]/5$ – where $V_c(z)$ is the comoving volume at a redshift z and the $1/5$ term reflects the angular area covered by J-PAS (see 1.3.3); after that, the MCMaps code runs an MCMC simulation for each of the four different redshift bins; finally, all resulting chains for each redshift bins z_i are put together after removing the burn-ins and after fixing both selection function parameters ($\bar{n}_{0,z}$ and $c_{1,z}$). Results are also presented using Planck [3] and Hubble Space Telescopes [48], together with SDSS low- z BAO data [11], all obtained from CosmoMC [42]⁴.

For comparison, the final analysis were made using $64 \times 64 \times 64$ and $128 \times 128 \times 128$ grids containing the same V_{eff} for each of the redshift bins, *i.e.*, the size of the cells changes for each of the catalogs. One will be able to see that this makes a considerable difference on the estimates of the cosmological parameters, although the main analysis is

⁴CosmoMC is able to provide chains for the desired parameters using data from different sources. Available online at <http://http://cosmologist.info/cosmomc> .

made only for the 128^3 cells case. Once again, the main goal is to probe H_0 , Ω_c , w_0 and w_a .

4.3.1 Individual Redshift Bin Analysis

This Section shows the results for each of the redshift bins analysed, $0.2 < z_1 < 0.4$, centered in $z_1 = 0.3$; $0.4 < z_2 < 0.6$, centered in $z_2 = 0.5$; $0.6 < z_3 < 0.8$, centered in $z_3 = 0.7$; and $0.8 < z_4 < 1.0$, centered in $z_4 = 0.9$. This means that the mean galaxy density in the center of each catalog is given by the value on Table 4.2. For each of these cases, the analysis process follows the same procedure described for the Gaussian selection function case, Section 4.2.3: the resulting chains from the MCMs code are binned and projected in one- and two-dimensional distributions, always marginalizing over the other parameters. For the selection function effect analysis, a comparison between marginalizing over the selection function together with others cosmological parameters, and fixing the $\bar{n}(r)$ parameters to then marginalize over the other cosmological parameters, is made. The catalogs's individual characteristics can be found on Table 4.3 for the 64^3 cells maps and on Table 4.4 for the main 128^3 cells maps. Histograms and two-dimensional marginalized distributions for each of the redshift bins maps shown hereafter refer only to the 128^3 cells case. The other case, with 64^3 cells, appears only in the joint probability analysis as a matter of comparison.

z_i	$V_{eff} [Gpc^3 h^{-3}]$	$L_{cell}^{64} [Mpc h^{-1}]$	$\bar{n}_{0,z}^{64} [gal/cell]$	$c_{1,z}^{64} [1/cell]$
0.3	2.44	21.04	27.04	0.0249
0.5	5.5	27.60	14.8794	0.0915
0.7	8.6	32.01	1.167	0.2190
0.9	11.6	35.37	0.01147	0.414

Table 4.3: Main characteristics of the 64^3 cells maps for each redshift bin.

z_i	$V_{eff} [Gpc^3 h^{-3}]$	$L_{cell}^{128} [Mpc h^{-1}]$	$\bar{n}_{0,z}^{128} [gal/cell]$	$c_{1,z}^{128} [1/cell]$
0.3	2.44	10.52	3.473	0.0125
0.5	5.5	13.79	4.346	0.0293
0.7	8.6	16.01	0.14595	0.1095
0.9	11.6	17.68	1.434×10^{-3}	0.2068

Table 4.4: Main characteristics of the 128^3 cells maps for each redshift bin..

In order to perform importance sampling [42], which means to use joint probabilities of different datasets, all MCMs chains where probed using the same flat priors (4.2) on

the cosmological parameters. Flat priors are more “orthodox”, and do not lead to any significant bias on the estimates since they are assumed to be 0 or 1 inside a given region. The priors considered for this work are

1. $40. < H_0 < 95$ Mpc/km/s;
2. $0.05 < \Omega_c < 0.60$;
3. $-4.0 < w_0 < -0.4533$;
4. $-4.0 < w_a < 0.75$;

Also, all chains were generating using 512 walkers and 500 steps each, in a total of $256k$ points to sample the posterior distribution. Burn in is different for each case and is based on the technique explained in Section 3.3.

Graphical results are shown in two different ways. First, the two-dimensional distributions for pairs of parameters with 1, 2, and 3σ contours together with their respective histograms with the 1σ vertical lines, containing 68.26% of the values inside it (Figures 4.13 to 4.16). Second, the one-dimensional marginalized distributions are shown in detail for the cases where one marginalize over all six parameters (H_0 , Ω_c , w_0 , w_a , $\bar{n}_{0,z}$ and $c_{1,z}$) and when one fixes the selection function at its fiducial value, marginalizing only over the remaining cosmological parameters H_0 , Ω_c , w_0 , w_a (Figures 4.17 to 4.20).

Best-fit values and error bars are also quoted in two ways: the mean value and standard deviation of the one-dimensional marginalized distributions, presented in Tables 4.5 to 4.8, and the values corresponding to the maximum for the multi-dimensional likelihood together with the percentiles containing 68.26% (1σ) of the points around the quoted value – these are presented on the one-dimensional histograms for both fixing and marginalizing over the selection function parameters.

One can see a considerable change for the maximum likelihood values when fixing the selection function parameters together with a substantial decrease on the 1σ regions. This suggests that marginalizing over the selection function parameters, *i.e.*, considering them as nuisance parameters, affects the best-fit values and the error bar in a way that cannot be ignored. It is also clear, from Figures 4.17 to 4.20, that dark energy’s equation of state parameters are more sensitive to the estimation of the selection function as a nuisance parameter, while H_0 and Ω_c become less sensitive at higher redshift.

Note how the estimates on dark energy’s parameters become more and more precise as redshift grows. However, for the last slice, $z_4 = 0.9$, as the map is closer to redshifts where matter was dominant over dark energy, these estimates worse. This leads to poor estimates, even if the selection function parameters are fixed (Figure 4.20).

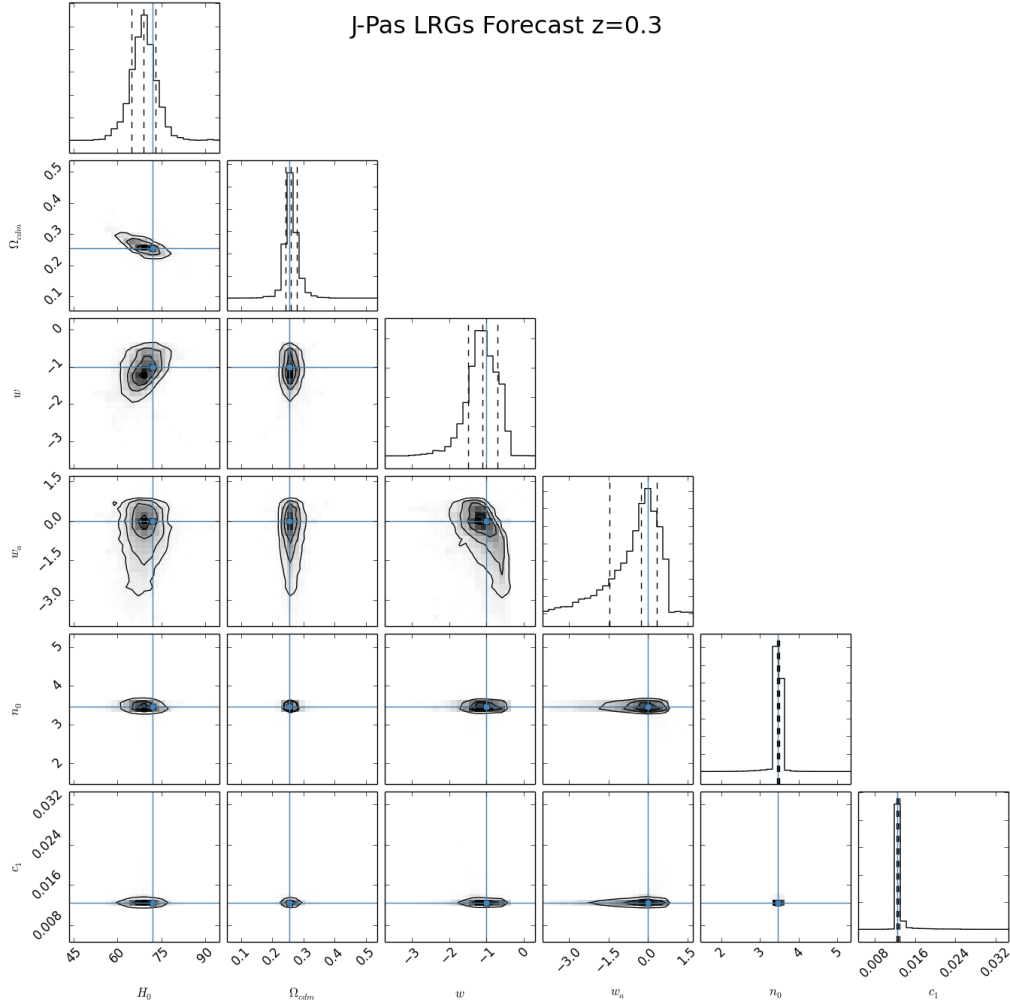


Figure 4.13: One- and two-dimensional distributions for the estimated parameters H_0 , Ω_c , w_0 , w_a , $\bar{n}_{0,z}$ and $c_{1,z}$ for the redshift bin $z_1 = 0.3$. Blue lines show the true values for each parameter. Note the expected correlation between H_0 and Ω_c which will reflect in all the other bins. Notice also that the estimation of selection function parameters is very precise in almost all cases.

$z_1 = 0.3$			
Parameter	Fiducial Value	Mean Value	Standard Deviation
H_0	72	68.791	± 4.462
Ω_c	0.2538	0.2607	$\pm 2.288 \times 10^{-2}$
w_0	-1.0	-1.131	± 0.4036
w_a	0.0	-0.5150	± 0.9564
$\bar{n}_{0,0.3}$	3.473	3.466	± 0.9563
$c_{1,0.3}$	1.25×10^{-2}	1.288×10^{-2}	$\pm 1.370 \times 10^{-3}$

Table 4.5: Mean value and standard deviations for the $z_1 = 0.3$ slice. Results obtained from the one-dimensional marginalized distributions for each parameter. H_0 is in $Mpc/km/s$, $\bar{n}_{0,0.3}$ and $c_{1,0.3}$ are expressed in cell units.

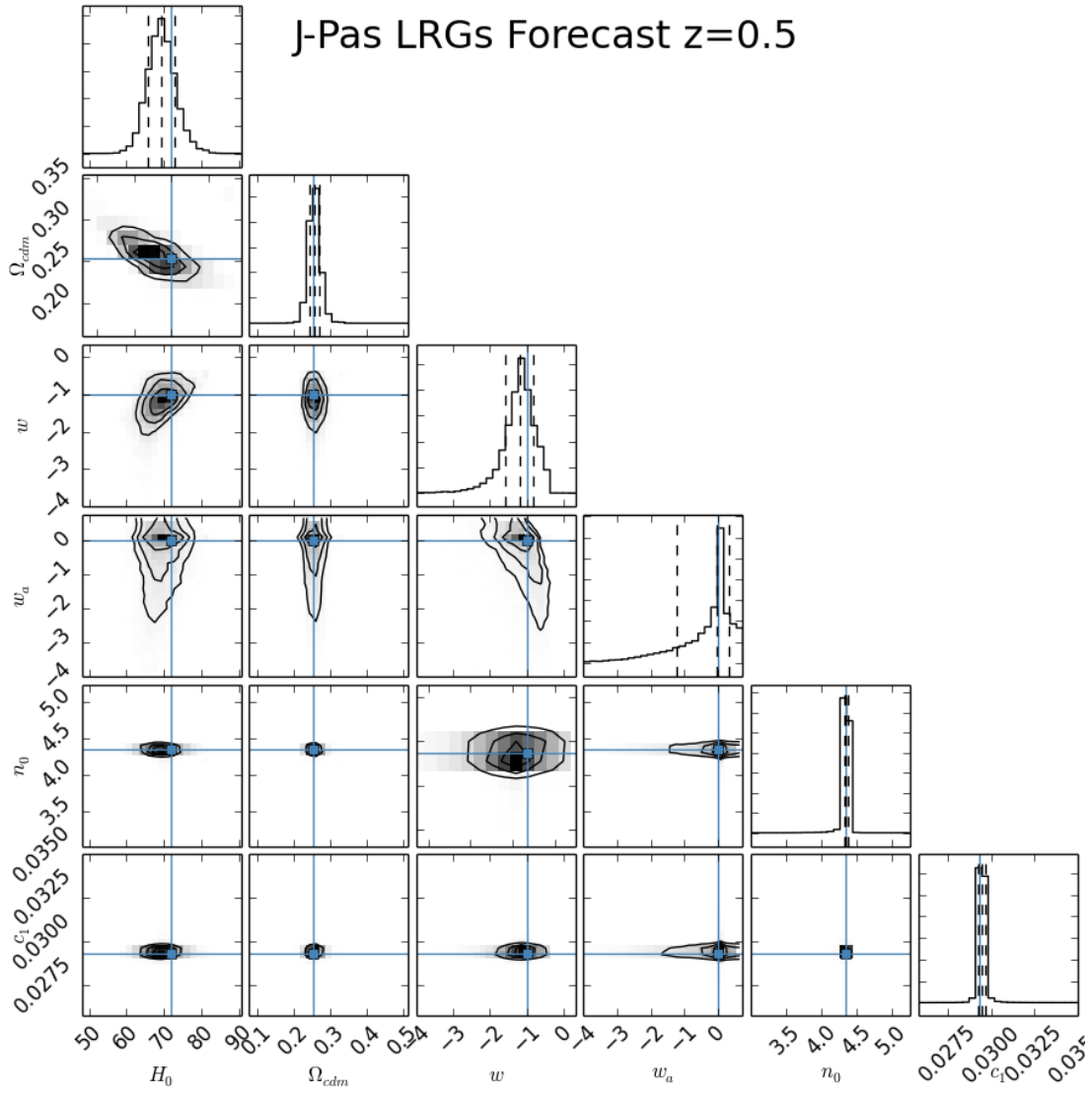


Figure 4.14: One- and two-dimensional distributions for the estimated parameters H_0 , Ω_c , w_0 , w_a , $\bar{n}_{0,z}$ and $c_{1,z}$ for the redshift bin $z_2 = 0.5$. Blue lines show the true values for each parameter.

$z_2 = 0.5$			
Parameter	Fiducial Value	Mean Value	Standard Deviation
H_0	72	69.397	± 3.737
Ω_c	0.2538	0.2670	$\pm 1.661 \times 10^{-2}$
w_0	-1.0	-1.230	± 0.45716
w_a	0.0	-0.373	± 0.8913
$\bar{n}_{0,0.5}$	4.346	4.346	$\pm 5.20 \times 10^{-2}$
$c_{1,0.5}$	2.93×10^{-2}	2.945×10^{-2}	$\pm 2.370 \times 10^{-4}$

Table 4.6: Mean value and standard deviations for the $z_2 = 0.5$ slice. Results obtained from the one-dimensional marginalized distributions for each parameter. H_0 is in $Mpc/km/s$, $\bar{n}_{0,0.5}$ and $c_{1,0.5}$ are expressed in cell units.

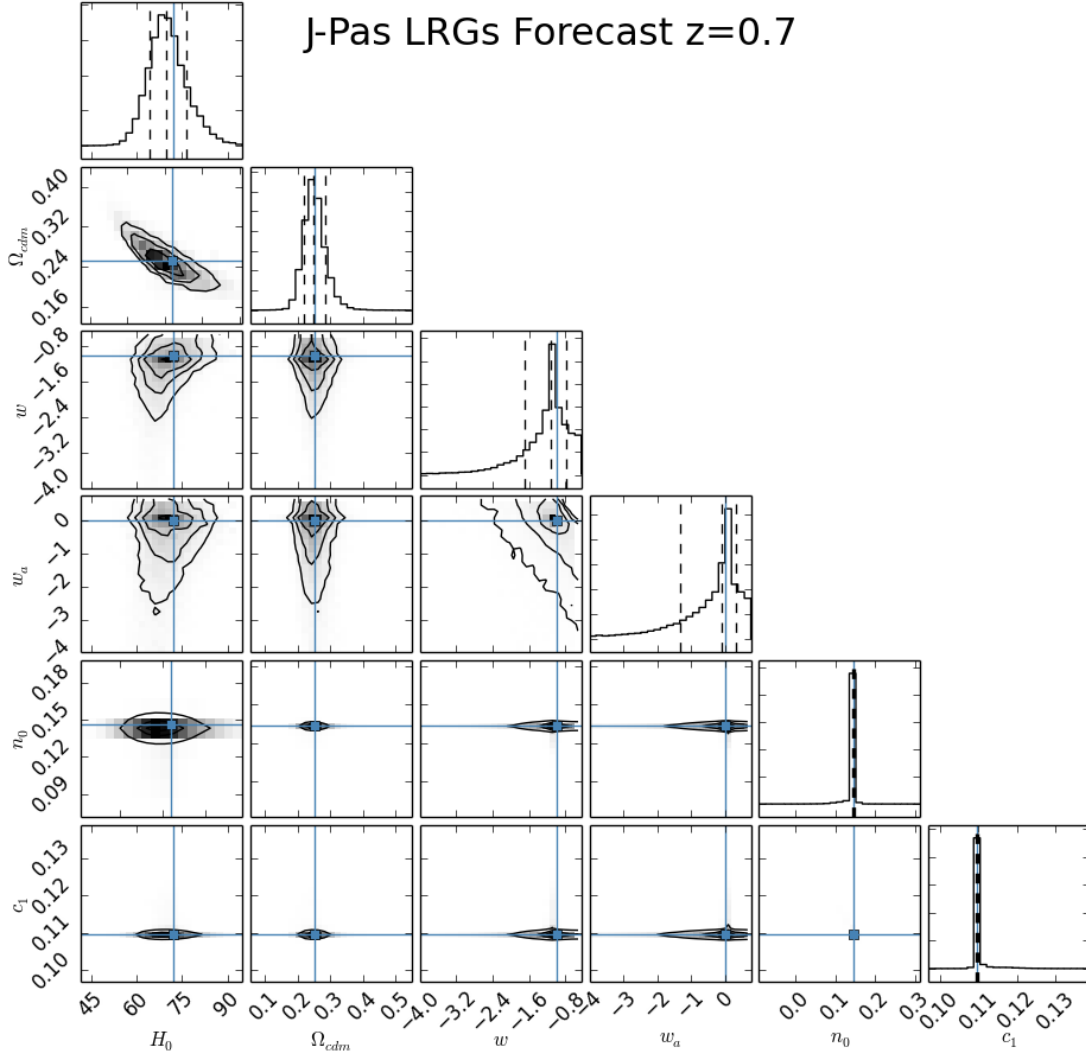


Figure 4.15: One- and two-dimensional distributions for the estimated parameters H_0 , Ω_c , w_0 , w_a , $\bar{n}_{0,z}$ and $c_{1,z}$ for the redshift bin $z_3 = 0.7$. Blue lines show the true values for each parameter. Note that some correlation seems to appear between w_0 and w_a for higher redshifts.

$z_3 = 0.7$			
Parameter	Fiducial Value	Mean Value	Standard Deviation
H_0	72	70.474	± 6.434
Ω_c	0.2538	0.2525	$\pm 3.430 \times 10^{-2}$
w_0	-1.0	-1.256	± 0.5740
w_a	0.0	-0.460	± 0.9630
$\bar{n}_{0,0.7}$	0.1459	0.1444	$\pm 1.017 \times 10^{-2}$
$c_{1,0.7}$	0.1095	0.1099	$\pm 1.873 \times 10^{-3}$

Table 4.7: Mean value and standard deviations for the $z_3 = 0.7$ slice. Results obtained from the one-dimensional marginalized distributions for each parameter. H_0 is in $Mpc/km/s$, $\bar{n}_{0,0.7}$ and $c_{1,0.7}$ are expressed in cell units.

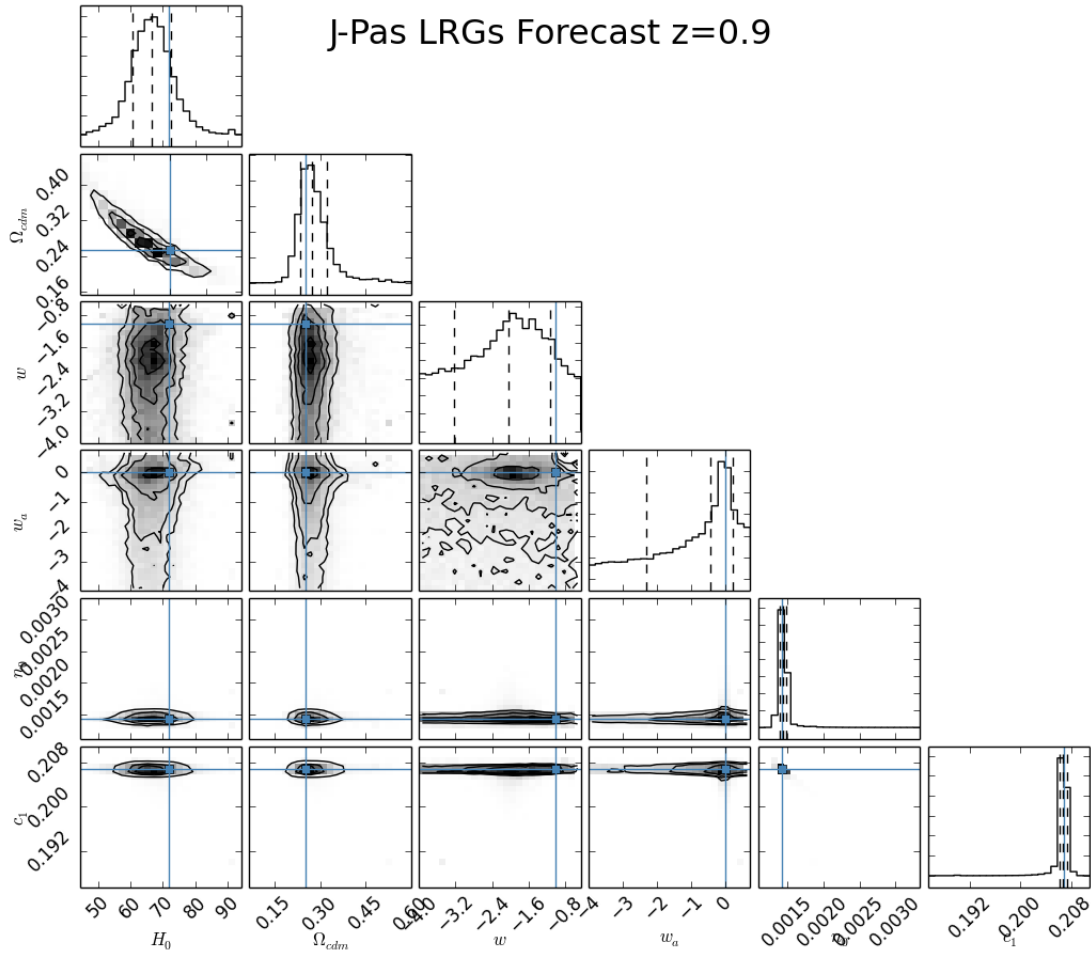


Figure 4.16: One- and two-dimensional distributions for the estimated parameters H_0 , Ω_c , w_0 , w_a , $\bar{n}_{0,z}$ and $c_{1,z}$ for the redshift bin $z_4 = 0.9$. Blue lines show the true values for each parameter. It starts to get clear here that for higher redshifts, as z gets closer to $z = 1$, the dark energy era comes near the matter dominated era, so the dark energy equation of state parameters, w_0 and w_a , are harder to probe.

$z_4 = 0.9$			
Parameter	Fiducial Value	Mean Value	Standard Deviation
H_0	72	66.660	± 6.502
Ω_c	0.2538	0.2821	$\pm 5.694 \times 10^{-2}$
w_0	-1.0	-2.131	± 0.9264
w_a	0.0	-0.855	± 1.2184
$\bar{n}_{0,0.9}$	1.434×10^{-3}	0.1448×10^{-3}	$\pm 8.68 \times 10^{-5}$
$c_{1,0.9}$	0.2068	0.2066	$\pm 1.189 \times 10^{-3}$

Table 4.8: Mean value and standard deviations for the $z_4 = 0.9$ slice. Results obtained from the one-dimensional marginalized distributions for each parameter. H_0 is in $Mpc/km/s$, $\bar{n}_{0,0.9}$ and $c_{1,0.9}$ are expressed in cell units.

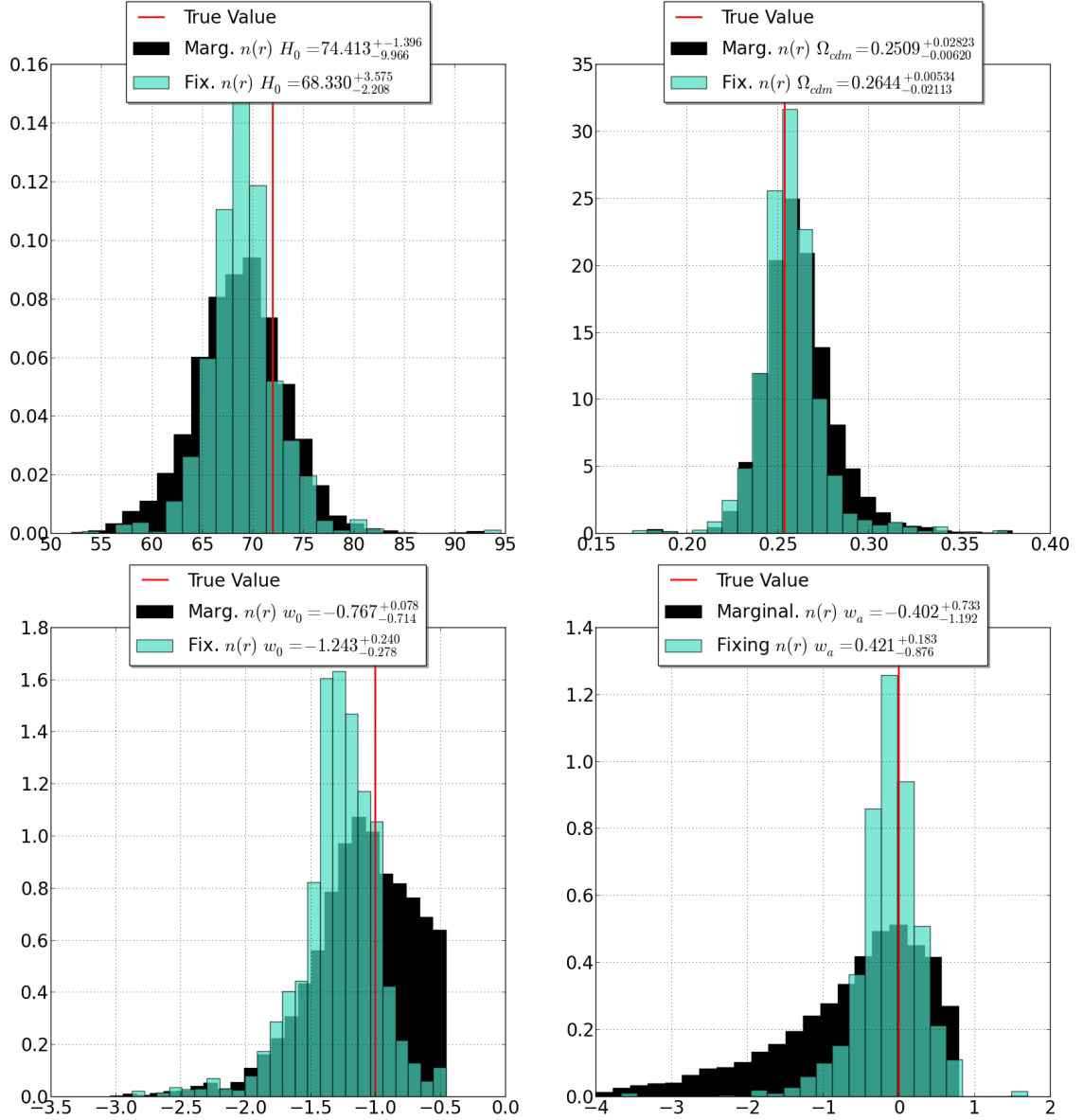


Figure 4.17: ($z_1 = 0.3$) One-dimensional marginalized distributions for H_0 (upper left), Ω_c (upper right), w_0 (lower left), and w_a (lower right). Two cases are presented, (green) fixing the selection function parameters at their fiducial values ($\bar{n}_{0,0.3} = 3.473$ gal/cell and $c_{1,0.3} = 1.25 \times 10^{-2}$ 1/cell) and (black) marginalizing over all other estimated parameters, considering the selection function parameters as nuisance. Red lines are the true values. Note that the values quoted are not the maximum of the marginalized distributions, but the coordinate in parameter space of the maximum likelihood value. Best-fit values for all parameters get closer to the true value, except for w_a whose change is small but there is a considerable decrease on its error bars.

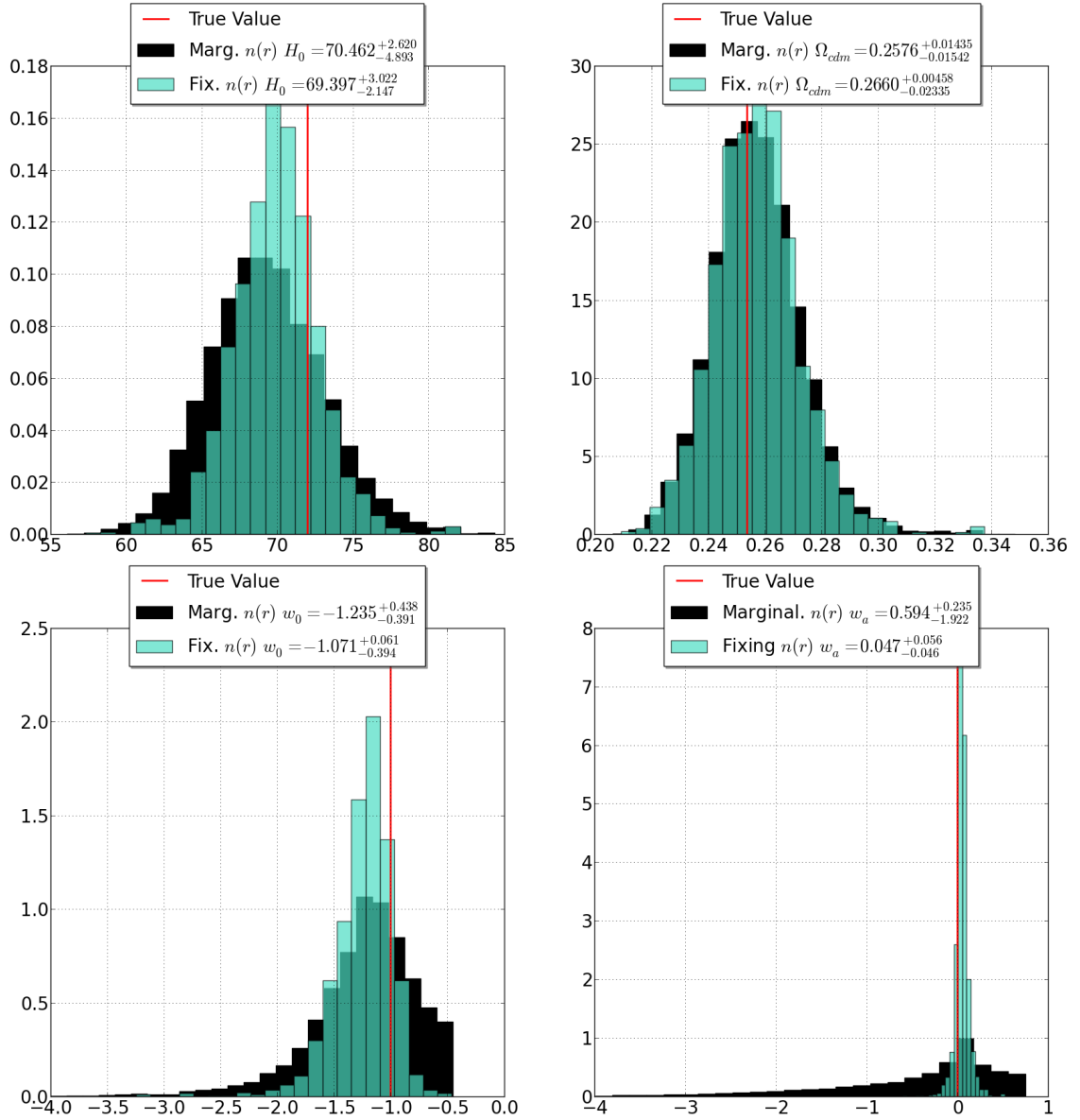


Figure 4.18: ($z_2 = 0.5$) One-dimensional marginalized distributions for H_0 (upper left), Ω_c (upper right), w_0 (lower left), and w_a (lower right). Two cases are presented, (green) fixing the selection function parameters at their fiducial values ($\bar{n}_{0,0.5} = 4.346$ gal/cell and $c_{1,0.5} = 2.930 \times 10^{-2}$ 1/cell) and (black) marginalizing over all other estimated parameters, considering the selection function parameters as nuisance. Red lines are the true values. Here, the sensibility of dark energy parameters with the selection function estimation becomes even more clear. Although there's still a considerable change on H_0 and Ω_c best-fit values and error bars, changes for w_0 and w_a are more dramatic. Best-fit values get even closer to the true values, while error bars drastically decrease.

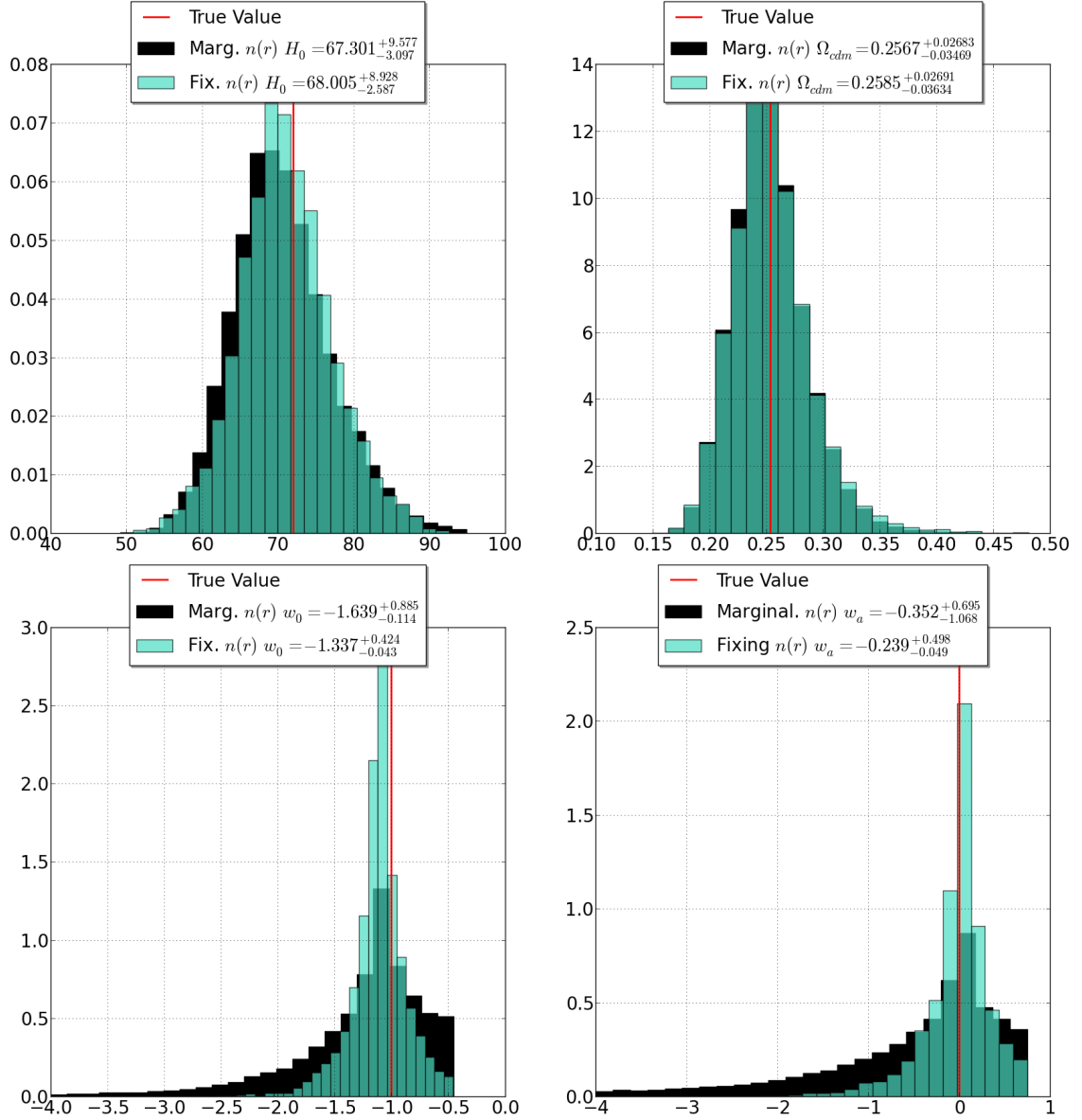


Figure 4.19: ($z_3 = 0.7$) One-dimensional marginalized distributions for H_0 (upper left), Ω_c (upper right), w_0 (lower left), and w_a (lower right). Two cases are presented, (green) fixing the selection function parameters at their fiducial values ($\bar{n}_{0,0.7} = 0.14595$ gal/cell and $c_{1,0.7} = 0.1095$ 1/cell) and (black) marginalizing over all other estimated parameters, considering the selection function parameters as nuisance. Red lines are the true values. Note that for this case, H_0 and Ω_c are practically insensitive to the selection function estimation while dark energy's equation of state parameters still show a big difference between the two cases, both for best-fit values and error bars.

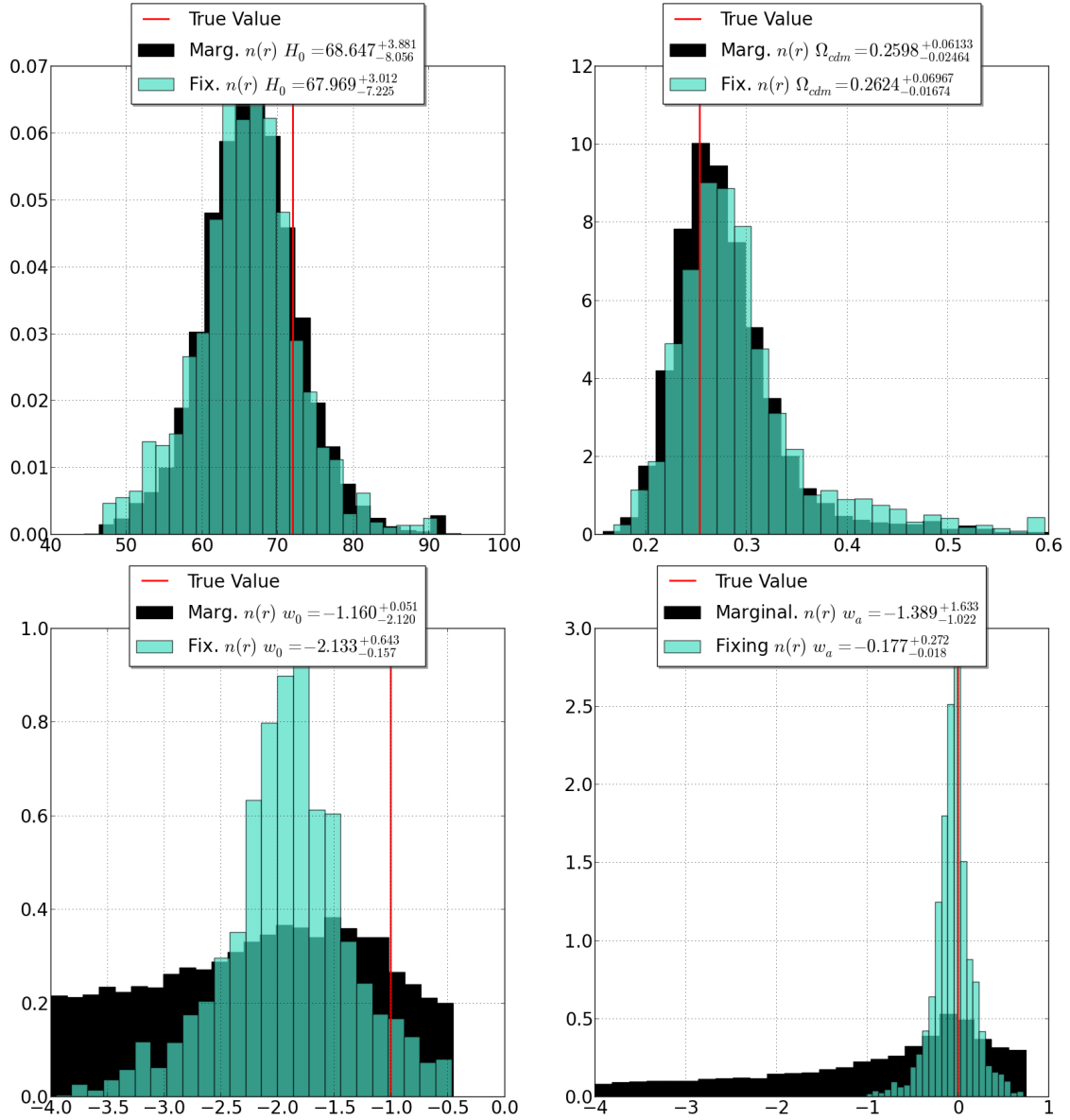


Figure 4.20: ($z_4 = 0.9$) One-dimensional marginalized distributions for H_0 (upper left), Ω_c (upper right), w_0 (lower left), and w_a (lower right). Two cases are presented, (green) fixing the selection function parameters at their fiducial values ($\bar{n}_{0,0.9} = 1.434 \times 10^{-3}$ gal/cell and $c_{1,0.9} = 0.2068$ 1/cell) and (black) marginalizing over all other estimated parameters, considering the selection function parameters as nuisance. Red lines are the true values. For this case, two phenomena become clear. Firstly, as the effective volume for $z_4 = 0.9$ is much bigger than the other cases, the cell size ($L_{cell}(z_4) = 17.89 \text{ Mpc } h^{-1}$) makes it harder to probe the BAO scale, which reflects in worse estimates for cosmological parameters that depend on these measurement. Secondly, as redshift gets closer to $z = 1$, the dark energy era has not yet started in full, so the dark energy parameters are less sensible to LSS measurements. This explain the bad estimates on w_0 when fixing the selection function parameters.

4.3.2 Joint Data Set Analysis

When estimating an ensemble of parameters from different datasets, one may wish to join all data to obtain better constraints. **Importance sampling** is a statistical tool that makes this kind of analysis possible. Given a sample set from a posterior distribution P , it is possible to estimate parameters with respect to a similar distribution P' . This is done using a weighting scheme that is proportional to the ratio of the probabilities P/P' [42]. The expected value of some function $f(\mathbf{q})$ under the new distribution P' is given by

$$\langle f(\mathbf{q}) \rangle_{P'} \approx \frac{\sum_{i=1}^N P'(\mathbf{q}_i)/P(\mathbf{q}_i)f(\mathbf{q}_i)}{\sum_{i=1}^N P'(\mathbf{q}_i)/P(\mathbf{q}_i)}. \quad (4.23)$$

However, for the current application, all datasets have the same flat priors and are, therefore, consistent with each other. For this case, importance sampling is done by just joining the ensembles after the burn in procedure is made and after the selection function parameters are fixed (or marginalized) for each of the different redshift bins. The consistency of datasets can be observed as the posterior distribution shrinks after joining the data ensembles.

The CosmoMC code [42] allows to generate parameter chains using data from existing cosmological experiments like Planck Space Telescope [3], HST [48], Sloan [7, 11] and others. In order to constrain the chains presented in the previous Section with importance sampling, CosmoMC was used, employing the same flat priors on the cosmological parameters, with data from these three cosmological experiments cited above (Planck, HST, and SDSS low- z BAOs measurements).

Figures 4.21 to 4.24 show the joint two-dimensional probabilities, together with the one-dimensional marginalized distribution for each of the given cosmological parameters considering the two cases with the selection function parameters fixed at their fiducial values. Results are shown using J-PAS forecasts alone, and J-PAS forecast together with the other experiments using CosmoMC – using 64^3 cells (Figures 4.21 and 4.22 respectively) and 128^3 cells (Figures 4.23 and 4.24 respectively). Table 4.9 gives a summary of the mean and standard deviation values for each case.

Comparing both cases for different numbers of cells, one can see that the 64^3 has worse estimates on the dark energy parameters. The reason is simple: as the volumes are the same for both catalogs, the cell size is larger if the number of cells is smaller – as one can see from Tables 4.3 and 4.4. A larger cell size means that the BAO statistics gets washed out, or even biased, by the poor statistics done inside the larger cells. For the $z_4 = 0.9$ catalog in the 64^3 cells case, the cell size is $L_{cell,0.9} = 35.37 \text{ Mpc } h^{-1}$, meaning that the BAO scale fits inside only 3 cells. As for the other case (128^3 cells), the BAO scale fits inside eight times as many cells, leading to better statistics.

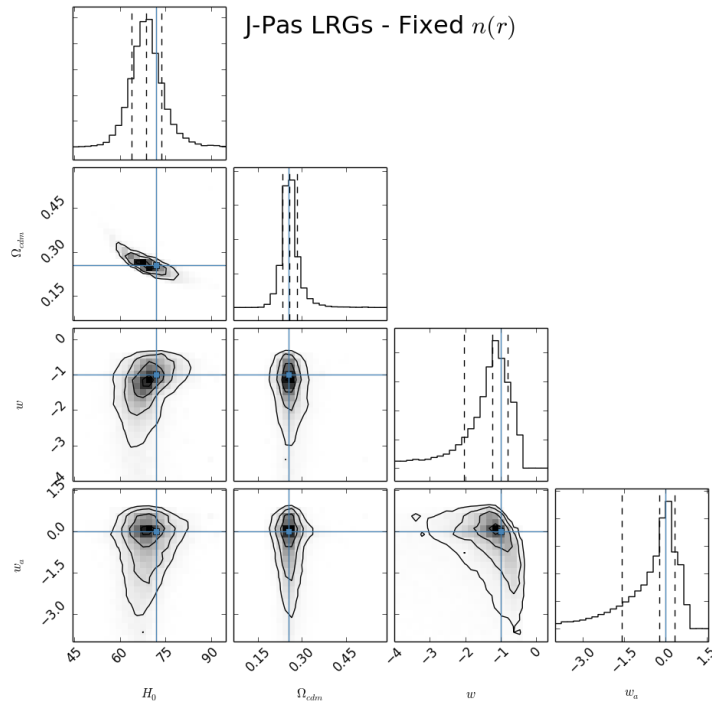


Figure 4.21: One- and two-dimensional distributions using the 64^3 cells maps together ($0.2 < z < 1.0$) for the estimated parameters H_0 , Ω_c , w_0 , and w_a fixing the selection function parameters at their fiducial value.

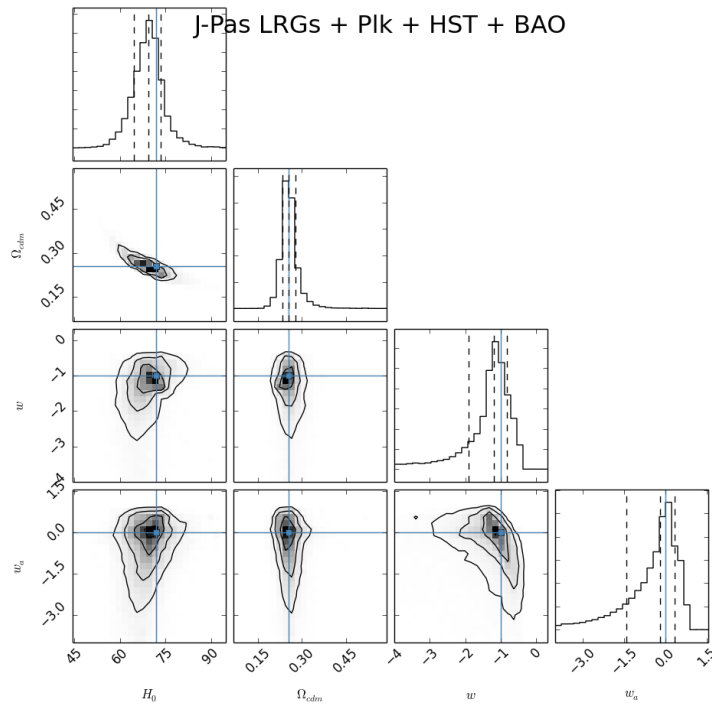


Figure 4.22: One- and two-dimensional distributions using the 64^3 cells maps together ($0.2 < z < 1.0$) and using Planck, HST and SDSS BAO data for the estimated parameters H_0 , Ω_c , w_0 , and w_a .

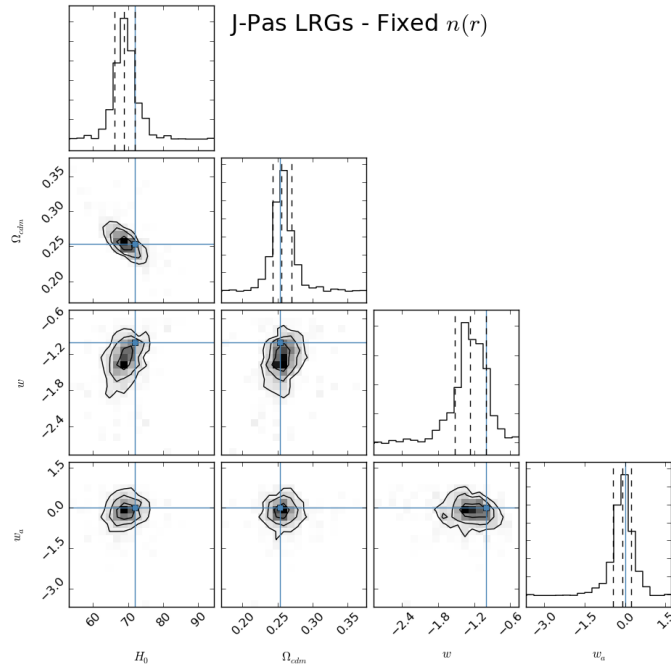


Figure 4.23: One- and two-dimensional distributions using the 128^3 cells maps together ($0.2 < z < 1.0$) for the estimated parameters H_0 , Ω_c , w_0 , and w_a fixing the selection function parameters at their fiducial value.

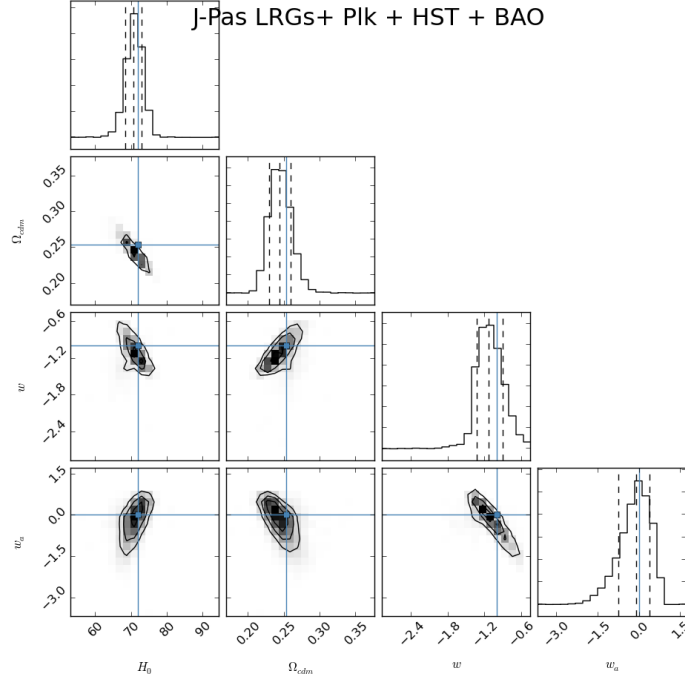


Figure 4.24: One- and two-dimensional distributions using the 128^3 cells maps together ($0.2 < z < 1.0$) and using Planck, HST and SDSS BAO data for the estimated parameters H_0 , Ω_c , w_0 , and w_a fixing the selection function parameters at their fiducial value.

-	Fiducial Value	J-PAS 64 ³	J-PAS+Plk+HST+BAO 64 ³	J-PAS 128 ³	J-PAS+Plk+HST+BAO 128 ³
H_0	72	68.866 ± 5.566	69.228 ± 5.212	69.081 ± 3.579	70.732 ± 2.464
Ω_c	0.2538	0.2606 ± 0.0343	0.2575 ± 0.0325	0.25723 ± 0.0186	0.2449 ± 0.0160
w_0	-1.0	-1.422 ± 0.727	-1.366 ± 0.680	-1.283 ± 0.313	-1.117 ± 0.231
w_a	0.0	-0.559 ± 1.022	-0.498 ± 0.973	-0.130 ± 0.447	-0.1848 ± 0.574

Table 4.9: Best-fit parameters (mean) and 1σ (standard deviation) values considering the one-dimensional marginalized distributions for each parameter in all cases considered above on Figures 4.21 to 4.24. Selection function parameters are fixed on their respective fiducial values.

Note that for w_a , adding Planck, HST and BAO data to the 128³ cells case makes the estimate worse by less than $\sigma/2$. This phenomenon exposes a certain tension between the fiducial cosmology used to generate the galaxy mocks for the MCMaps analysis and the Planck/HST/BAO maximum likelihood values. The reason this only happens to w_a is because it is the most sensitive parameter, *i.e.*, the one with weaker constraints from cosmological observations. Such feature is expected and does not mean that the datasets are inconsistent with each other, it only exposes a tension between them.

For the final analysis, consider the one-dimensional marginalized distributions for both types of maps on Figures 4.25 and 4.26. Results are presented considering three types of datasets: marginalizing over all parameters, including the selection function ones; fixing the selection function parameters at their fiducial values and marginalizing over the remaining ones; and adding Planck, HST, SDSS BAO data to this last case.

From the analysis and figures presented in this Section, one can conclude that the size of cells considered for the galaxy maps is fundamental. For cell sizes of almost one third of the BAO scale ($\sim 105 \text{ Mpc } h^{-1}$), the statistics between cells makes it hard to probe dark energy parameters with high accuracy. When probing these parameters with smaller cells, the BAO scale fits inside more cells, which makes the estimates more precise. Once more, the effect on the selection function estimation proves itself influential when estimating ensembles of cosmological parameters.

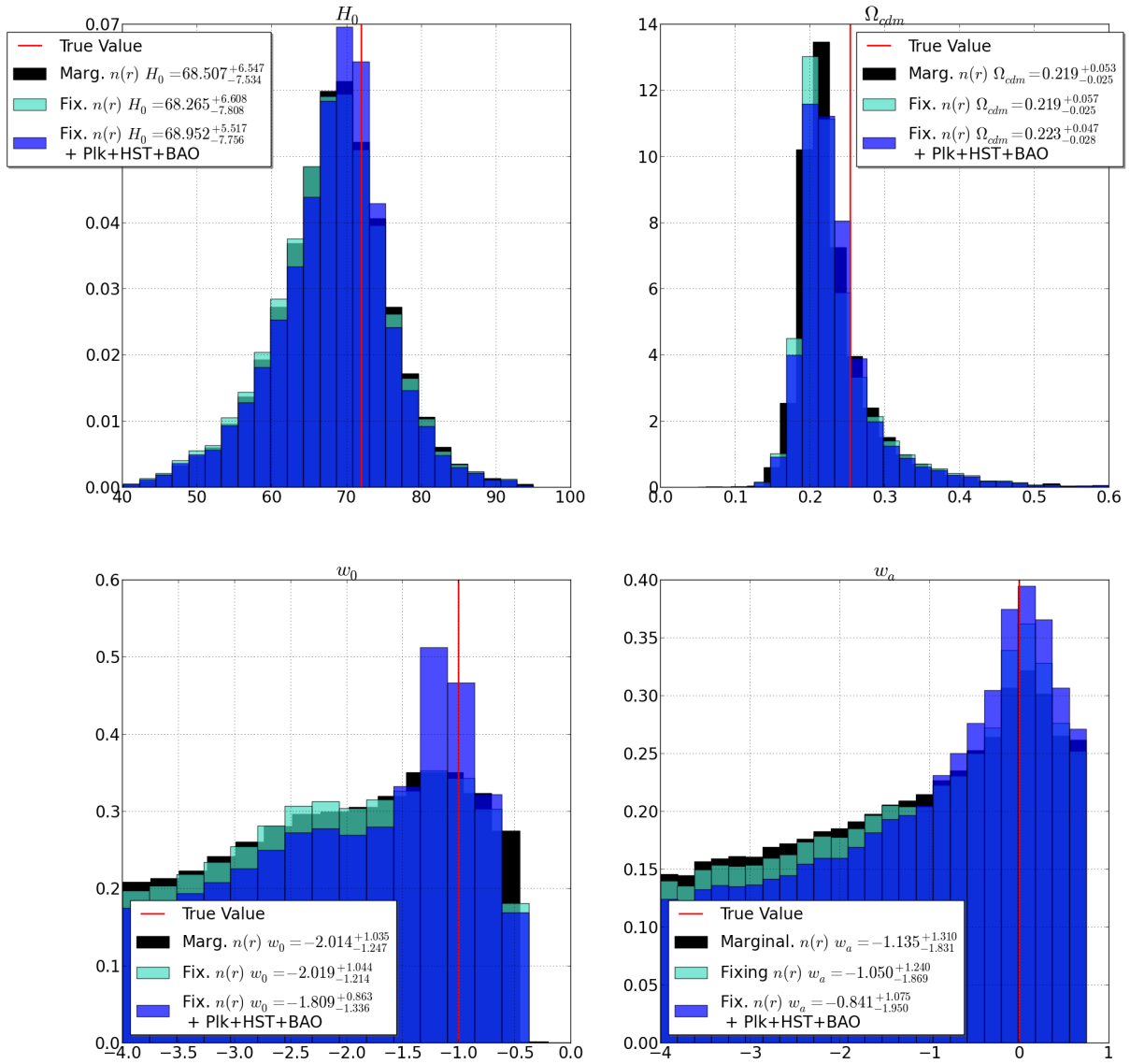


Figure 4.25: (64^3) Marginalized distributions for H_0 (upper left), Ω_c (upper right), w_0 (lower left), and w_a (lower right). Three cases are presented, (black) marginalizing over all estimated parameters, (green) fixing the selection function parameters at their fiducial values marginalizing over all the remaining, and (blue) adding Planck, HST and SDSS low- z BAO data to the fixed selection function case. Red lines are the true values. Values quoted are not the maximum of the marginalized distributions, but the coordinates in parameter space of the maximum likelihood value. Observe that estimates for dark energy parameters are not well constrained even when joining external data to it.

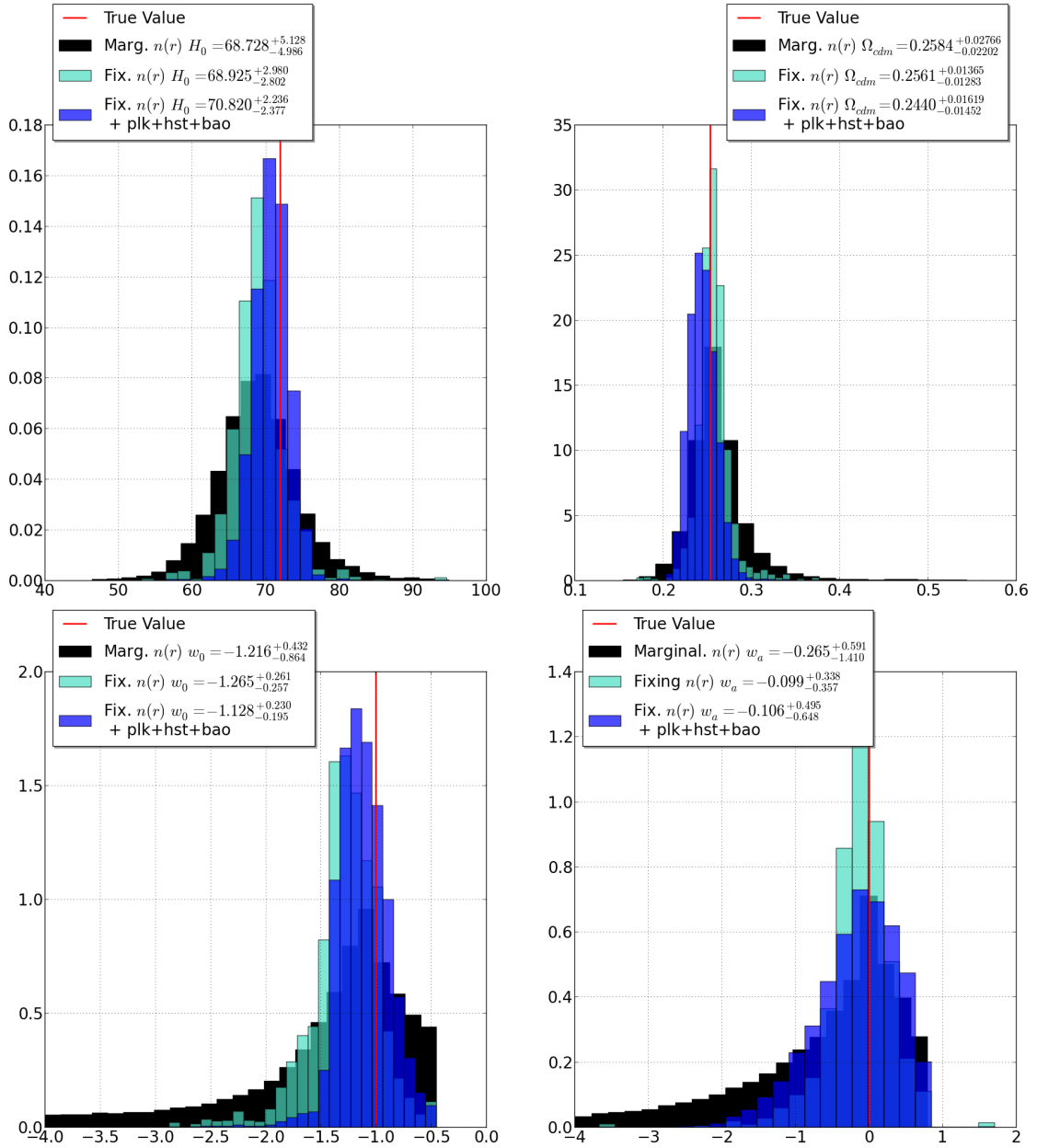


Figure 4.26: (128^3) Marginalized distributions for H_0 (upper left), Ω_c (upper right), w_0 (lower left), and w_a (lower right). Three cases are presented, (black) marginalizing over all estimated parameters, (green) fixing the selection function parameters at their fiducial values marginalizing over all the remaining, and (blue) adding Planck, HST and SDSS low- z BAO data to the fixed selection function case. Red lines are the true values. Here, adding external datasets makes all estimates better, values are closer to their true values and error bars decrease. The only exception is w_a , whose best-fit value and error bars get worse as more data is added to J-PAS LRGs forecast. The reason for this discrepancy might come from tension between some values on the fiducial cosmology considered for J-PAS forecast and the external datasets.

Chapter 5

Conclusions

Precision cosmology hopes to achieve errors of order of a few percent for all cosmological parameters. To succeed, systematic errors must be taken into account. Photometric redshifts, for example, have their own systematics and even if surveys like J-PAS hope to lower these to less than 0.3% [10], there are still different effects that must be probed in order to achieve higher precision. It was demonstrated in Section 4.2 that the survey’s geometry plays a major role in galaxy power spectra estimation. The convolution with the respective window function alters the convolved spectra – what is actually measured – in a variety of ways. Even a simple selection function can modify the measured power spectrum in a subtle way, making it very hard to distinguish those effects from variants of the cosmological parameters. Acknowledging that nuisance parameters can affect estimates should help controlling some of these problems. However, it is still necessary to comprehend **how** they can affect the analysis.

The present work implemented a “forward” method for galaxy power spectrum estimation using a fast parallelized MCMC algorithm. Different from other galaxy power spectra analysis, the MCMC method compares estimations for the data galaxy power spectra with theoretical galaxy power spectra from galaxy mock realizations. This means that, instead of using a theoretical matter power spectrum from linear perturbation theory (Section 2.1), one uses a “theoretical” $P_g(k)$, estimated over the same geometry as the data. Using this approach, it is possible to understand the behaviour of the survey’s geometry on the estimated cosmological parameters. Performing analytical convolutions with the window function – obtained from a survey’s selection function – is not always a simple task, as was shown in Section 4.2. To deconvolve the real matter power spectrum from the window function is an even harder task. Instead, the method presented here was able to perform a certain kind of deconvolution. After performing the Monte-Carlo, it is possible to obtain estimates for all the cosmological parameters, their best-fit values, and error bars. Making use of this information together with any code capable of evolving cosmological perturbations to obtain a theoretical power spectrum – like CAMB, for example –, one is able to recover the deconvolved underlying matter power spectrum and

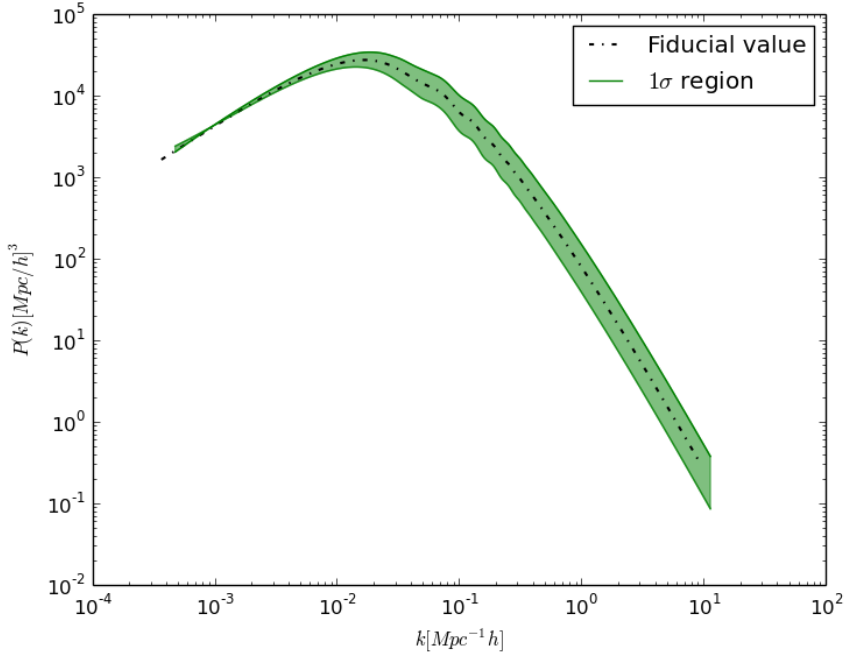


Figure 5.1: Illustration of a deconvolved matter power spectrum together with the 1σ region using estimation of the parameters H_0 , Ω_c , w_0 , and w_a from the MCMaps code.

its error bars, given the estimated cosmology (Figure 5.1).

To understand the processes that govern the nature of the accelerated expansion of the Universe, usually attributed to dark energy, is also one of the purposes of modern cosmology. There are two probes of dark energy study – its density Ω_{DE} and its equation of state, being the second less constrained by current data. The Dark Energy Task Force suggested that, if dark energy evolves as a function of redshift, *i.e.*, if dark energy is not actually a cosmological constant, the CPL parametrization (1.2) is a useful tool to study the accelerated expansion. As it was demonstrated on Sections 4.3.1 and 4.3.2, the CPL parameters, w_0 and w_a , are very sensitive to the marginalization of the selection function parameters. If these parameters are fixed on their fiducial values, the error bars can get $\sim 40\%$ lower for w_0 and $\sim 34\%$ lower for w_a , when compared to the error bars on the marginalized $\bar{n}(r)$ analysis. Of course, when comparing two distributions from a resulting MCMC, the one that has less parameters will always have smaller error bars, but is important to understand how treating the selection function as a nuisance can affect the estimates.

For the remaining cosmological parameters, the Hubble constant and the dark matter density, errors decrease down to 57% and 53%, respectively, in comparison with the marginalized selection function estimations. This demonstrates once again the importance of acknowledging the effects a convolution with the selection function may have on the measured galaxy power spectrum. In order to obtain maximum precision, knowing

the survey’s geometry for each galaxy species should lower systematic errors introduced by this type of effect.

In conclusion, the methods applied here were able to recover well the fiducial cosmology, with reasonable errors, and demonstrated the effects of a nuisance selection function. Yet, some simple modifications of these methods can lead to interesting features in the near future. It is a matter of fact that introducing redshift space, multi-tracer analysis, bias estimation, etc, will result in a more realistic data analysis. For example, it was shown by Abramo and Leonard (2013) that a multi-tracer analysis lowers even more the systematic errors introduced by survey’s geometry, specifically cosmic variance due the survey’s limited volume. An implementation of a multi-tracer galaxy power spectra estimator can be performed, and the mock catalog generation module of the MCMaps code already simulates multiple species of galaxies using the same underlying Gaussian density field. However, to fully estimate how a multi-tracer analysis could improve the cosmological parameters estimations, one must take into account that different tracers have not only different selection functions, but also different biases. Once a bias estimation is implemented on the MCMaps algorithm, this analysis should be trivial.

In addition, tests with real data or more complex mock galaxy catalogs need to be performed together with the implementation of a method to probe the selection function in order to estimate the data FKP error bars (2.85). As the code was developed to be a part of J-PAS’s pipeline, it is already public available and “user friendly”. Any researcher can choose which of the nine cosmological parameters to probe and write its own selection function without any problem. A more detailed commented version of the code will be available in the near future in order to be widely used by the J-PAS community.

Appendices

Appendix A

Moments of a Log-Normal Distribution

The log-normal (LN) distribution is defined such as its logarithm is normally distributed, *i.e.*, a Gaussian distribution. Which means that if a random variable, θ , comes from a LN distribution, $\gamma = \ln(\theta)$ is a normally distributed variable. Therefore, if γ comes from a Gaussian distribution, $\theta = e^\gamma$ is a LN distributed variable. The major difference between both distributions is the fact that log-normal random variables only assume positive values.

A LN random variable can be defined in terms of the mean, μ , and variance, σ , of a normal distribution.

$$\theta = e^{\mu + \alpha\sigma} \quad (\text{A.1})$$

as, by definition, the logarithm of a variable is normally distributed. On the expression above, α is just a standard normal variable. Finally, the LN probability distribution is defined as

$$\mathbb{P}_{LN}(\theta; \mu, \sigma) = \frac{1}{\theta\sigma\sqrt{2\pi}} \exp\left\{-\frac{(\ln \theta - \mu)^2}{2\sigma^2}\right\} \quad (\text{A.2})$$

With $\theta > 0$.

First Moment: Mean Value

The mean value of the distribution is given by the expected value of its first moment, $E[\theta]$. One can evaluate it in terms of the normal distributed variable, γ , as $E[\theta] = E[e^\gamma]$.

$$\begin{aligned}
 E[e^\gamma] &= \int_{-\infty}^{+\infty} d\gamma e^\gamma \mathbb{P}_G(\gamma; \mu, \sigma) \\
 &= \int_{-\infty}^{+\infty} d\gamma e^\gamma \frac{1}{\sqrt{2\pi\sigma^2}} \exp\left\{-\frac{(\gamma - \mu)^2}{2\sigma^2}\right\} \\
 &= \frac{1}{\sqrt{2\pi\sigma^2}} \int_{-\infty}^{+\infty} d\gamma \exp\left\{\gamma - \frac{(\gamma - \mu)^2}{2\sigma^2}\right\} \\
 &= \frac{1}{\sqrt{2\pi\sigma^2}} \int_{-\infty}^{+\infty} d\gamma \exp\left\{-\frac{1}{2\sigma^2}[\gamma^2 + (-2\sigma^2 - 2\mu)\gamma + \mu^2]\right\}
 \end{aligned} \tag{A.3}$$

Completing squares inside the brackets on the exponential, one can write

$$\begin{aligned}
 E[e^\gamma] &= \frac{1}{\sqrt{2\pi\sigma^2}} \int_{-\infty}^{+\infty} d\gamma \exp\left\{-\frac{1}{2\sigma^2}[\gamma - (\sigma^2 + \mu)]^2 + \frac{\sigma^2}{2} + \mu\right\} \\
 &= \exp\left\{\mu + \frac{\sigma^2}{2}\right\} \underbrace{\frac{1}{\sqrt{2\pi\sigma^2}} \int_{-\infty}^{+\infty} d\gamma \exp\left\{-\frac{1}{2\sigma^2}[\gamma - (\sigma^2 + \mu)]^2\right\}}_{=1}
 \end{aligned} \tag{A.4}$$

So, finally, in terms of the log-normal distributed variable, θ ,

$$E[\theta] = \exp\left\{\mu + \frac{\sigma^2}{2}\right\}. \tag{A.5}$$

Second Moment and Variance

To evaluate the variance, defined as $Var[\theta] = E[\theta^2] - E[\theta]^2$, one needs to calculate the second moment of the LN distribution. Using the same technique as for the first moment, $E[\theta^2] = E[e^{2\gamma}]$, leading to

$$\begin{aligned}
 E[e^{2\gamma}] &= \frac{1}{\sqrt{2\pi\sigma^2}} \int_{-\infty}^{+\infty} d\gamma e^{2\gamma} \exp\left\{-\frac{(\gamma - \mu)^2}{2\sigma^2}\right\} \\
 &= \frac{1}{\sqrt{2\pi\sigma^2}} \int_{-\infty}^{+\infty} d\gamma \exp\left\{2\gamma - \frac{(\gamma - \mu)^2}{2\sigma^2}\right\}.
 \end{aligned} \tag{A.6}$$

Now, again completing squares, one can write

$$E[e^{2\gamma}] = e^{(2\mu+2\sigma^2)} \underbrace{\frac{1}{\sqrt{2\pi\sigma^2}} \int_{-\infty}^{+\infty} d\gamma \exp\left\{-\frac{(\gamma - \mu - 2\sigma^2)^2}{2\sigma^2}\right\}}_{=1}. \tag{A.7}$$

Therefore,

$$E[\theta^2] = e^{2\mu+2\sigma^2} \tag{A.8}$$

As for the variance of the log-normal distribution, it can be evaluated as

$$\text{Var}[\theta] = E[\theta^2] - E[\theta]^2 = (e^{\sigma^2} - 1)e^{2\mu + \sigma^2}. \quad (\text{A.9})$$

k^{th} Moment

As a matter of fact, one can easily deduce a general expression for the k^{th} moment of the LN distribution. From (A.6), one can write

$$E[e^{k\gamma}] = \frac{1}{\sqrt{2\pi\sigma^2}} \int_{-\infty}^{+\infty} d\gamma e^{k\gamma} \exp\left\{-\frac{(\gamma - \mu)^2}{2\sigma^2}\right\}, \quad (\text{A.10})$$

and, after completing squares as in the first and second moment,

$$E[e^{k\gamma}] = e^{k(2\mu + k\sigma^2)/2} \underbrace{\frac{1}{\sqrt{2\pi\sigma^2}} \int_{-\infty}^{+\infty} d\gamma \exp\left\{-\frac{(\gamma - \mu - k\sigma^2)^2}{2\sigma^2}\right\}}_{=1}. \quad (\text{A.11})$$

So, the k^{th} moment of the log-normal distribution is given by

$$E[\theta^k] = e^{k(2\mu + k\sigma^2)/2}. \quad (\text{A.12})$$

Bibliography

- [1] S. Perlmutter et al., *Measurements of Ω and Λ from 42 High-Redshift Supernovae*, *The Astrophysical Journal* **517** (June, 1999) 565–586, [[astro-ph/9812133](#)].
- [2] A. G. Riess et al., *Observational Evidence from Supernovae for an Accelerating Universe and a Cosmological Constant*, *The Astronomical Journal* **116** (Sept., 1998) 1009–1038, [[astro-ph/9805201](#)].
- [3] Planck Collaboration, P. A. R. Ade, N. Aghanim, C. Armitage-Caplan, M. Arnaud, M. Ashdown, F. Atrio-Barandela, J. Aumont, C. Baccigalupi, A. J. Banday, and et al., *Planck 2013 results. XVI. Cosmological parameters*, *Astronomy and Astrophysics* **571** (Nov., 2014) A16, [[arXiv:1303.5076](#)].
- [4] M. Chevallier and D. Polarski, *Accelerating Universes with Scaling Dark Matter*, *International Journal of Modern Physics D* **10** (2001) 213–223, [[gr-qc/0009008](#)].
- [5] E. V. Linder, *Exploring the Expansion History of the Universe*, *Physical Review Letters* **90** (Mar., 2003) 091301, [[astro-ph/0208512](#)].
- [6] A. Albrecht, G. Bernstein, R. Cahn, W. L. Freedman, J. Hewitt, W. Hu, J. Huth, M. Kamionkowski, E. W. Kolb, L. Knox, J. C. Mather, S. Staggs, and N. B. Suntzeff, *Report of the Dark Energy Task Force*, *ArXiv Astrophysics e-prints* (Sept., 2006) [[astro-ph/0609591](#)].
- [7] J. Loveday, J. Pier, and SDSS Collaboration, *The Sloan Digital Sky Survey*, in *Wide Field Surveys in Cosmology* (S. Colombi, Y. Mellier, and B. Raban, eds.), p. 317, 1998. [astro-ph/9809179](#).
- [8] The Dark Energy Survey Collaboration, *The Dark Energy Survey*, *ArXiv Astrophysics e-prints* (Oct., 2005) [[astro-ph/0510346](#)].
- [9] K. S. Dawson et al., *The Baryon Oscillation Spectroscopic Survey of SDSS-III*, *The Astronomical Journal* **145** (Jan., 2013) 10, [[arXiv:1208.0022](#)].
- [10] N. Benitez et al., *J-PAS: The Javalambre-Physics of the Accelerated Universe Astrophysical Survey*, *ArXiv e-prints* (Mar., 2014) [[arXiv:1403.5237](#)].

- [11] D. J. Eisenstein et al., *Detection of the Baryon Acoustic Peak in the Large-Scale Correlation Function of SDSS Luminous Red Galaxies*, *The Astrophysical Journal* **633** (Nov., 2005) 560–574, [astro-ph/0501171].
- [12] B. Bassett and R. Hlozek, *Baryon acoustic oscillations*, p. 246. 2010.
- [13] J. M. Bardeen, J. R. Bond, N. Kaiser, and A. S. Szalay, *The statistics of peaks of Gaussian random fields*, *The Astrophysical Journal* **304** (May, 1986) 15–61.
- [14] A. Einstein, *The foundation of the general theory of relativity*, in *The Collected Papers of Einstein - Vol. 6* (M. J. K. A. J. Kox and R. Schulmann, eds.), pp. 146–201. Princeton University Press, 1997.
- [15] S. Dodelson, *Modern Cosmology*. Academic Press, San Diego, US, 2003.
- [16] J. A. Peacock, *Cosmological Physics*. Cambridge University Press, Cambridge, UK, 1999.
- [17] P. J. E. Peebles, *Principles of Physical Cosmology*. Princeton University Press, Princeton, US, 1993.
- [18] P. Schneider, *Extragalactic Astronomy and Cosmology: An Introduction*. Springer, Berlin , GE, 2006.
- [19] C. Smeenk, *Time in cosmology*, in *A Companion to the Philosophy of Time* (H. Dyke and A. Bardon, eds.), pp. 201–219. John Wiley and Sons, Inc, 2013.
- [20] T. Padmanabhan, *Structure formation in the universe*. Cambridge University Press, Cambridge , UK, 1993.
- [21] B. Ratra and P. J. E. Peebles, *Cosmological consequences of a rolling homogeneous scalar field*, *Physical Review D* **37** (June, 1988) 3406–3427.
- [22] E. Abdalla, E. G. M. Ferreira, J. Quintin, and B. Wang, *New Evidence for Interacting Dark Energy from BOSS*, *ArXiv e-prints* (Dec., 2014) [arXiv:1412.2777].
- [23] L. Anderson et al., *The clustering of galaxies in the SDSS-III Baryon Oscillation Spectroscopic Survey: baryon acoustic oscillations in the Data Release 9 spectroscopic galaxy sample*, *Monthly Notices of the Royal Astronomical Society* **427** (Dec., 2012) 3435–3467, [arXiv:1203.6594].
- [24] W. Hu, *Dark energy and matter evolution from lensing tomography*, *Physical Review D* **66** (Oct., 2002) 083515, [astro-ph/0208093].

- [25] The Dark Energy Survey Collaboration, *The Dark Energy Survey Science Program*, .
- [26] N. Benítez, M. Moles, J. A. L. Aguerri, E. Alfaro, T. Broadhurst, J. Cabrera-Caño, F. J. Castander, J. Cepa, M. Cerviño, D. Cristóbal-Hornillos, A. Fernández-Soto, R. M. González Delgado, L. Infante, I. Márquez, V. J. Martínez, J. Masegosa, A. Del Olmo, J. Perea, F. Prada, J. M. Quintana, and S. F. Sánchez, *Optimal Filter Systems for Photometric Redshift Estimation*, *The Astrophysical Journal Letters* **692** (Feb., 2009) L5–L8, [arXiv:0812.3568].
- [27] L. R. Abramo, M. A. Strauss, M. Lima, C. Hernández-Monteagudo, R. Lazkoz, M. Moles, C. M. de Oliveira, I. Sendra, L. Sodré, and T. Storchi-Bergmann, *Measuring large-scale structure with quasars in narrow-band filter surveys*, *Monthly Notices of the Royal Astronomical Society* **423** (July, 2012) 3251–3267, [arXiv:1108.2657].
- [28] H. S. Xavier, L. R. Abramo, M. Sako, N. Benítez, M. O. Calvão, A. Ederoclite, A. Marín-Franch, A. Molino, R. R. R. Reis, B. B. Siffert, and L. Sodré, *Photometric Type Ia supernova surveys in narrow-band filters*, *Monthly Notices of the Royal Astronomical Society* **444** (Nov., 2014) 2313–2332, [arXiv:1312.5706].
- [29] A. Lewis, A. Challinor, and A. Lasenby, *Efficient computation of CMB anisotropies in closed FRW models*, *Astrophys. J.* **538** (2000) 473–476, [astro-ph/9911177].
- [30] H. A. Feldman, N. Kaiser, and J. A. Peacock, *Power-spectrum analysis of three-dimensional redshift surveys*, *The Astrophysical Journal* **426** (May, 1994) 23–37, [astro-ph/9304022].
- [31] W. J. Percival, L. Verde, and J. A. Peacock, *Fourier analysis of luminosity-dependent galaxy clustering*, *Monthly Notices of the Royal Astronomical Society* **347** (Jan., 2004) 645–653, [astro-ph/0306511].
- [32] D. J. Fixsen, E. S. Cheng, J. M. Gales, J. C. Mather, R. A. Shafer, and E. L. Wright, *The Cosmic Microwave Background Spectrum from the Full COBE FIRAS Data Set*, *The Astrophysical Journal* **473** (Dec., 1996) 576, [astro-ph/9605054].
- [33] P. Peter and J.-P. Uzan, *Cosmologie primordiale*. Editions Belin-Paris, Paris, FR, 2005.
- [34] J. A. Peacock et al., *A measurement of the cosmological mass density from clustering in the 2dF Galaxy Redshift Survey*, *Nature* **410** (Mar., 2001) 169–173.
- [35] D. J. Eisenstein and W. Hu, *Power Spectra for Cold Dark Matter and Its Variants*, *The Astrophysical Journal* **511** (Jan., 1999) 5–15, [astro-ph/9710252].

- [36] D. J. Eisenstein, H.-J. Seo, and M. White, *On the Robustness of the Acoustic Scale in the Low-Redshift Clustering of Matter*, *The Astrophysical Journal* **664** (Aug., 2007) 660–674, [astro-ph/0604361].
- [37] P. Coles and B. Jones, *A lognormal model for the cosmological mass distribution*, *Monthly Notices of the Royal Astronomical Society* **248** (Jan., 1991) 1–13.
- [38] D. W. Hogg, *Is cosmology just a plausibility argument?*, *ArXiv e-prints* (Oct., 2009) [arXiv:0910.3374].
- [39] D. S. Silvia and J. Skilling, *Data Analysis: A Bayesian Tutorial*. Oxford University Press, New York, US, 2006.
- [40] N. Christensen, R. Meyer, L. Knox, and B. Luey, *Bayesian methods for cosmological parameter estimation from cosmic microwave background measurements*, *Classical and Quantum Gravity* **18** (July, 2001) 2677–2688, [astro-ph/0103134].
- [41] L. Knox, N. Christensen, and C. Skordis, *The Age of the Universe and the Cosmological Constant Determined from Cosmic Microwave Background Anisotropy Measurements*, *The Astrophysical Journal Letters* **563** (Dec., 2001) L95–L98, [astro-ph/0109232].
- [42] A. Lewis and S. Bridle, *Cosmological parameters from CMB and other data: A Monte Carlo approach*, *Physical Review D* **66** (Nov., 2002) 103511, [astro-ph/0205436].
- [43] D. Foreman-Mackey, D. W. Hogg, D. Lang, and J. Goodman, *emcee: The MCMC Hammer*, *The Publications of the Astronomical Society of the Pacific* **125** (Mar., 2013) 306–312, [arXiv:1202.3665].
- [44] J. Goodman and J. Weare, *Ensemble samplers with affine invariance*, *Comm. App. Math. And Comp. Sci.* (2010).
- [45] L. R. Abramo, *The full Fisher matrix for galaxy surveys*, *Monthly Notices of the Royal Astronomical Society* **420** (Mar., 2012) 2042–2057, [arXiv:1108.5449].
- [46] L. R. Abramo and K. E. Leonard, *Why multitracer surveys beat cosmic variance*, *Monthly Notices of the Royal Astronomical Society* **432** (June, 2013) 318–326, [arXiv:1302.5444].
- [47] R. W. Hockney and J. W. Eastwood, *Computer Simulations Using Particles*. Taylor and Francis Group, New York, US, 1988.

-
- [48] W. Zheng, H. Li, J.-Q. Xia, Y.-P. Wan, S.-Y. Li, and M. Li, *Constraints on cosmological models from Hubble parameters measurements*, *International Journal of Modern Physics D* **23** (Apr., 2014) 50051, [[arXiv:1403.2571](#)].